Universität Stuttgart
Institut für Kernenergetik
und Energiesysteme

Experimental investigation on heat transfer and pressure drop of supercritical carbon dioxide cooling in small diameter tubes

Andreas Wahl

April 2022 IKE 2-168

IKE

Universität Stuttgart
Institut für Kernenergetik
und Energiesysteme

Experimental investigation on heat transfer and pressure drop of supercritical carbon dioxide cooling in small diameter tubes

von der Fakultät Energie-, Verfahrens- und Biotechnik der Universität Stuttgart zur Erlangung der Würde eines Doktor-Ingenieurs (Dr.-Ing.) genehmigte Abhandlung

vorgelegt von

M.Sc- Andreas Wahl

geboren in Backnang.

Hauptberichter: Herr Prof. Dr.-Ing. Jörg Starflinger

Mitberichter: Prof. Dr. techn. Günter Scheffknecht

Tag der Einreichung: 14.04.2022

Tag der mündlichen Prüfung: 28.09.2022

ISSN-0173-6892

April 2022 IKE 2-168

Erklärung über die Eigenständigkeit der Dissertation

Ich versichere, dass ich die vorliegende Arbeit mit dem Titel

„Experimental Investigation on heat transfer and pressure drop of supercritical carbon dioxide cooling in small diameter tubes “

selbstständig verfasst und keine anderen als die angegebenen Quellen und Hilfsmittel benutzt habe; aus fremden Quellen entnommene Passagen und Gedanken sind als solche kenntlich gemacht.

Stuttgart, den 17.10.2022

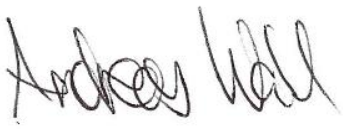

Andreas Wahl

Vorwort

Die vorliegende Forschungsarbeit auf dem Gebiet der Wärmeübertragung mit überkritischem CO2 entstand am Institut für Kernenergetik und Energiesysteme (IKE) der Universität Stuttgart und wurde im Rahmen des EU-Projektes „sCO_2-flex“ durchgeführt.

Ein besonderer Dank gilt meinem Betreuer Herrn Prof. Dr.-Ing. Jörg Starflinger für die wissenschaftliche Betreuung meiner Arbeit. Für Fragen stand er mir jederzeit zur Verfügung und während des Projektes unterstützte er mich mit wertvollen Hinweisen und Tipps. Mein herzlicher Dank geht auch an Herrn Prof. Dr. techn. Günter Scheffknecht für sein Engagement bei der Übernahme des Mitberichts.

Im Weiteren ist mein Abteilungsleiter Herr Dr.-Ing. Rainer Mertz zu nennen, der stets ein offenes Ohr für Fragen hatte und jederzeit eine äußerst verlässliche Unterstützung war. Meinem Büro- und Versuchsanlagenpartner Herr Konstantinous Theologou möchte ich besonderen Dank aussprechen. Seine fachliche Kompetenz und unermüdliche Motivation haben mir sehr geholfen diese Arbeit durchzuführen.

Weiterhin bedanke ich mich bei allen Kollegen des IKE für das freundschaftliche Miteinander, die angenehmen wissenschaftlichen Diskussionen sowie den gemeinsamen Dienstreisen.

Nicht unerwähnt bleiben sollen außerdem meine Studenten, die im Rahmen einer Bachelor-, Studien- oder Masterabeit oder als studentische Hilfskraft ebenfalls einen Beitrag zum Gelingen meiner Arbeit geleistet haben. Vielen Dank an Sümeyye Köse, Tatjana Wagner, Luisa Haak, Robert Ullmann, Ekrem Sahin, Robin Schmelcher, Alexa Kuhn, Amelia Torres.

Nicht zuletzt möchte ich mich bei meinen Eltern, Udo und Sibylle Wahl, für die fortlaufende Unterstützung meiner gesamten Ausbildung bedanken - ohne das Verständnis und die Hilfe eurerseits hätte ich diesen Weg nicht geschafft.

Vielen Dank!

Kurzfassung

Kraftwerkskreisläufe mit überkritischem Kohlendioxid (sCO_2) als Arbeitsmittel haben hohes Potenzial in Hinsicht von Effizienz- und Flexibilitätssteigerungen im Vergleich zu konventionell wasserdampfbetriebenen Kraftwerken. Das kompaktere Anlagenlayout reduziert den Materialeinsatz, was wiederum zu niedrigeren Investitionskosten führt. Bei der Wärmeabfuhr nahe dem kritischen Druck durchlaufen die thermophysikalischen Stoffeigenschaften abrupte Änderungen. Daher variieren die Wärmeübertragung und die hydraulischen Eigenschaften innerhalb eines engen Temperaturbereichs stark.

Die vorliegende Arbeit untersucht die Wärmeübertragung und den Druckverlust von sCO_2 in Rohrströmungen mit kleinem Durchmesser, um eine Designempfehlungen für neuartige Konzepte kompakter Wärmeübertrager zu liefern. Der Einsatz kompakter Wärmeübertrager hat das Potential die Effizienz, Lastwechselgeschwindigkeit und Zuverlässigkeit eines Kraftwerkskreislauf unter hohem CO_2-Druck und kleiner Differenztemperatur zu verbessern.

Es wurden zwei Teststrecken in Form eines Doppelrohrwärmeübertrager konzipiert und aufgebaut. Die sCO_2-Rohrströmung, mit jeweils 2 mm und 3 mm Innendurchmesser, wird durch das Kühlmedium im Ringspalt abgekühlt. Temperaturmessungen in der Wandung des Innenrohres ermöglichen die quantitative Bewertung des Wärme-übertragungskoeffizienten der sCO_2 Strömung. Die Arbeit wurde thematisch in vier Kaptitel unterteilt. In jedem Abschnitt wird eine Messkampagne vorgestellt und die Ergebnisse mit entsprechenden Literaturdaten verglichen.

Mit dem 2 mm-Versuchsrohr wurde die turbulente Wärmeübertragung untersucht. Unter weitreichender Variation der Betriebsbedingungen von sCO_2 (Druck, Temperatur, Massenfluss) und Kühlmedium (Volumenstrom, Temperatur) wurde der Einfluss auf den Wärmeübertragungskoeffizient untersucht. Die signifikanten Einflüsse aller Parametern wurden aufgezeigt und eine neue Nusselt-Wärmeübertragungs-gleichung wurde entwickelt.

Die Wärmeübertragung in vertikaler Strömungsausrichtung wurde mit beiden Versuchsrohren untersucht. Eine deutliche Verschlechterung der Wärmeübertragung in der Abwärtsströmung wurde festgestellt, welche durch Beschleunigungs- und Auftriebseffekte verursacht wird.

In den horizontalen Versuchsreihen mit dem 3 mm Rohr wurden Messungen doppelt durchgeführt mit jeweils Temperaturmessungen oben und unten in der Rohrwandung. Bei Variation von CO_2-Massenfluss und CO_2-Temperatur wurde eine Temperaturschichtung festgestellt.

Mit beiden Versuchrohren wurde der Druckverlust untersucht. Mit jeweils einer isothermen Versuchskampagne wurden eine Gleichung für den Reibungs-koeffizienten validiert. Basierend darauf wurde die Vorhersagbarkeit des Druckverlustes beim Kühlen untersucht. Die Berechnung der Druckverluste mit den Stoffeigenschaften bei Kernströmungstemperatur zeigten die beste Übereinstimmung mit den experimentellen Messungen.

Abstract

Power plants with supercritical carbon dioxide as working fluid have great potential to increase the efficiency and flexibility of current and future fossil fuel power plants in comparison to conventional water steam plants. CO_2 enables to build a power plant with a smaller physical footprint, thus, reduce the material input which leads to reduced capital costs. The heat removal close to the critical pressure is linked with abrupt changes in the thermophysical properties. This leads to strong variations of the heat transfer and pressure drop within a small temperature range.

Therefore, this work investigates the heat transfer and pressure drop performance of supercritical carbon dioxide in small diameter tube flow to contribute to the design of new concepts of compact heat exchangers. The compactness of heat exchangers reduces costs and material and further contributes to the cycle being able to work with high efficiency, speed and reliability under high CO_2 pressure and low pinch temperature.

Two test sections as a tube in tube heat exchangers were designed and constructed. CO_2 flows in the inner tube is cooled by the media flowing in the annulus. Temperature measurements in the wall of the inner tube facilitate the quantitative evaluation of the heat transfer coefficient of CO_2. The present work is structured in four chapters with respective experimental campaigns. Suitable literature data is presented in each chapter to evaluate the experimental results.

With the 2 mm test section the turbulent heat transfer performance was investigated. The heat transfer was evaluated with the variation of CO_2 parameters (pressure, temperature, mass flux) and the cooling media (volume flux, temperature). The significant influences of all parameters were illustrated and a new heat transfer correlation was developed.

The heat transfer in vertical flow direction was investigated in both test sections. A significant deterioration of the heat transfer in the downwards flow was detected which is caused by acceleration and buoyancy effects.

In the horizontal flow orientation with the 3 mm tube, an experimental campaign was conducted with the temperature measurement in the top and bottom sides of the tube wall. A temperature stratification was detected by the variation of CO_2 mass flux and CO_2 temperature.

The pressure drop was evaluated in both tubes. With an isothermal measurement campaign, a suitable correlation for the friction factor was validated. The predictability of the cooling process was evaluated based on this correlation. The pressuredrop calculation with the fluid properties of the bulk- and film temperature showed the best agreement with the experimental measurements.

Table of Contents

Nomenclature

A	(m²)	area of heat transfer
c_p	(J/kgK)	specific heat
d	(m)	diameter
g	(m/s²)	acceleration of gravity
G	(kg/m²s)	mass flux
Gr	(-)	Grashof number
h	(kJ/kg)	spec. Enthalpy
htc	(W/m²K)	heat transfer coefficient
K	(m)	wall roughness
L	(m)	length of discretization
m	(kg/s)	mass flow
Nu	(-)	Nusselt number
P	(bar)	pressure
Pr	(-)	Prandl number
Q	(W)	heat flow
$\dot{q}$	(W/m²)	heat flux
Re	(-)	Reynolds number
T	(°C)	temperature
v	(m/s)	velocity
V	(l/s)	volumetric flow
Greek symbols		
Δp	(bar)	pressure drop
β	(1/K)	Volumetric expansion coefficient
ε	(-)	relative roughness
η	(kg/ms)	dynamic viscosity
λ	(W/mK)	heat conductivity
ρ	(kg/m³)	density
ξ	(-)	friction factor

subscripts	
b	bulk
cool	cooling media
corr	correlation
CO_2	carbon dioxide
Cu	copper
exp	experiment
f	film
FC	forced convection
in	inlet
iso	isothermal
noniso	nonisothermal
out	outlet
t	tube
w	wall

1 Motivation

The European Union (EU) set the target to progressively reduce its greenhouse gas emissions up to 2050 to become a climate-neutral economy. In 2007, the EU leaders established the “2020 climate and energy package”, a set of laws passed to ensure that the EU meets its key climate and energy targets:

- 20% cut in greenhouse gas emissions (from 1990 levels)
- 20% of EU energy from renewables
- 20% improvement in energy efficiency

The EU is well on track to meet its emissions reduction target for 2020. EU greenhouse gas emissions were reduced by 24% between 1990 and 2019, while the economy grew by around 60% over the same period (Figure 1). In 2019, the share of consumed energy by renewable sources in the EU was 19.7%. The energy efficiency increased 26.6% from 2009 to 2019.

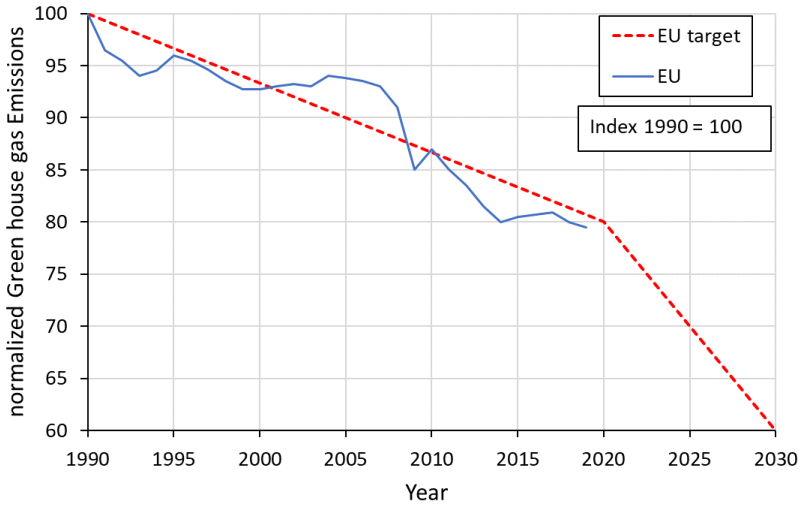

Figure 1: Greenhouse gas emissions from 1990 to 2018 in the EU [1]

For the year 2030, further ambitions are set:

- 40% cuts in greenhouse gas emissions (from 1990 levels),
- At least 32% share for renewable energy,
- At least 32.5% improvement in energy efficiency.

The long term strategy of the EU is to be climate-neutral by 2050 – an economy with net-zero greenhouse gas emissions [1]. All parts of society and economic sectors will play a role – from the power sector to industry, mobility, buildings, agriculture and forestry to meet the objectives [2].

In the context of the EU's climate and energy policy and to decarbonize the electricity sector, the role of fossil-fuel plants is intended and expected to evolve. Around 21 % of the final energy consumption in the EU is electricity and it is provided by different sources. In 2019, 39 % of the electricity consumed came from power plants burning fossil fuels and 35 % from renewable energy sources, while 26 % came from nuclear power plants. Current fossil-fuel power plants have been designed to operate in base-load conditions, i.e to provide a constant power output. However, their role is changing, due to the growing share of renewable energy sources, both in and outside the EU. Fossil-fuel power plants will increasingly be expected to provide fluctuating backup power, foster the integration of intermittent renewable energy sources and provide stability to the electricity grid. However, these plants are not able to undergo power output fluctuations.

Water has been used for decades as the thermodynamic cycle's working fluid in fossil-fuel power plants because water is abundant, cheap and presents positive thermodynamic properties. Water-related knowledge as its chemical and physical properties has continuously increased over the years, enabling to improve cycles' performances. However, the water-steam cycle enhancement is reaching economic (high-cost materials) and flexibility (long transient) limitations. In the meantime, investigations toward alternative thermodynamic cycles using other working fluids (helium, nitrogen, **carbon dioxide**, argon, etc.) have been carried out. Despite promising results, their development has been held back by several factors: fluid scarcity, toxicity and flammability, high costs, lack of suitable material able to withstand high temperatures.

In the last years, the constant improvement in materials and the development of new technologies have renewed the interest in sCO_2 cycles. Among promising fluids, CO_2 has several advantages such as chemical stability, excellent thermodynamic properties, low cost, availability and non-flammability. Finally, sCO_2 cycles present high performances with high responsiveness potential [3; 4].

The moderate value of its critical pressure (73.8 bar) makes CO_2 more economical for power plant applications than water where the critical pressure has much higher properties. In general, a low heat rejection temperature increases the efficiency of power cycles. The critical temperature of CO_2 (31.1°C) contributes to that advantage, however, it is not too low, to be cooled by the ambient temperature. CO_2 is regarded as an ideal natural working fluid with ODP = 0 (ozone depletion potential) and GWP = 1 (global warming potential) [5].

A sCO_2 Brayton cycle offers several benefits over competing power plant cycles. A high plant efficiency can be achieved due to the favourable fluid properties in the supercritical region. The high gas density of a supercritical working fluid allows to reduce the necessary compressor work and leads to a reduction in the overall size of the power plant. The reduced size of turbomachinery, boiler and heat exchangers can be further translated into reduced capital costs. A sCO_2 Brayton cycle can increase the operational flexibility and the efficiency of existing and future coal and lignite power plants [6].

The baseline cycle for most studies is the simple recuperated cycle (Figure 2). In this configuration, a recuperator is used to transfer heat from the hot exhaust leaving the turbine (5-6) to the cold fluid leaving the compressor (2-3). The isobaric heat addition in the boiler (3-4) takes at high pressure which is far away from the critical point (in the range of 200 to 250 bar) and the heat rejection (6-1) at pressures close to the critical point.

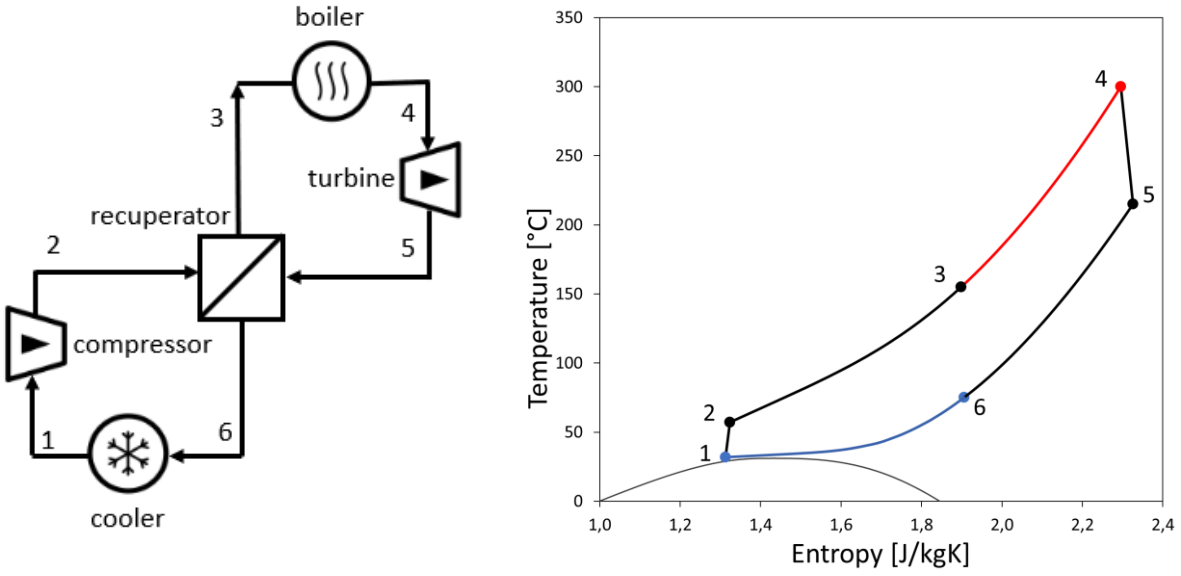

Figure 2: Cycle layout and T-s-diagram of a recuperated Brayton cycle

The heat removal close to the critical pressure is linked with abrupt changes in the thermo-physical properties. This leads to strong variations of the heat transfer and pressure drop within a small temperature range, which strongly effects the accurate dimensioning of the cooler of the brayton cycle. A heat exchanger with too small heat transfer surface can not remove the neccesary heat leading to strong influence of the the compressor inlet temperature and its efficiency. The measure to increase the heat removal is to increase the air ventilation which increases the power consumption of the cooler. In contrast to this, an “oversized” heat exchanger leads to increased thermal inertness, material input and capital costs. The research on heat transfer with sCO_2 as working fluid remains of high importancy for the development on an high efficient brayton cycle. The break down of an plant-size plate heat exchanger leads to the heat transfer capability of a single plate. The scaling procedure is explained in the literature [7; 8]. The experimental investigations on laboratory scale, such as two-plate heat exchangers, are showing promising results in regard to enhanced heat transfer and reduced pressure drop. Different kind of heat exchangers, such as printed circuit heat exchangers [9–24], finned-tube heat exchangers [25–29], plate and fin heat exchanger [30–39] are point of investigations. Further breakdown of the heat exchanger plate leads to the heat transfer and pressure drop in a single channel which is most commonly represented by the fluid flow in a straight and round tube. The experimental and numerical investigations are focusing on the local heat transfer in a wide range of tube diameters and flow directions. In this fundamental research, knowledge was gained starting from the heating application in nuclear power plant [40] or rockets [41]. Experimental investigations have been carried out with sCO_2 flowing inside electrically resistance heated tubes with different inner diameters [42–50]. For the cooling case, several researchers have investigated experimentally and numerically the heat transfer and pressure drop performance of sCO_2 in tubes of different sizes. The main focus was on the horizontal flow in tubes ranging from 0.5 to 10.7 mm inner diameter [51–59]. Especially, it has been shown that heat transfer correlations which were developed for big diameter tubes are not able to predict the heat transfer of small diameter tubes accurately. For this purpose, the heat transfer and pressure drop of small diameter tubes is investigated experimentally with a wide range of coundary conditions and flow directions to evaluate the validity of correlation from the literature.

2 State of the art

In this chapter, the sCO2 Brayton Cycle is introduced as the main motivation of this work. Different tasks in design and optimization of the cycle are presented including turbomachinery, control strategies and thermodynamic modelling leading to the heat exchanger as an important part of the cycle. A brief introduction including a literature review on industrial heat exchangers is presented in chapter 2.2. The relevant thermophysical properties of sCO_2 in the cooler of the cycle are presented in chapter 2.3.

In chapter 2.4, the state of the art of tube flow heat transfer and pressure drop starts with a general introduction which both research under heating and cooling conditions utilizing experimental and numerical work. In chapters 2.4.2 to 2.4.5, detailed information on the specific field of work is presented to illustrate the existing research gaps.

2.1 sCO_2 Brayton Cycle

The purpose of this section is to introduce the thermodynamic aspects of a sCO_2 Brayton cycle [60]. The operation under supercritical pressure raises requirements on operation and design of the cycle and components as the material must withstand corrosion under high temperature and pressure. Material selection for sCO_2 systems is dictated by the mechanical and thermal properties of the material and the fabrication costs. sCO_2 strongly influences the ionic solubility and dissociation process, which strongly affects corrosion, oxidation and creep resistance of the material [61]. Extensive investigations with high pressure and temperature in the CO_2 environment are available in literature including stainless steel, nickel-based and titanium-based alloys [62–66]. The heater has a large surface area exposed to the heat source which is highly demanding for material strength and durability. The recuperator operates under high temperatures, high absolute pressures and high-pressure differences between the exchanging fluids. This requires considerable material resistance to creep and corrosion for a long service duration without any structural degradation. The material selection also demands a balance between heat conduction and capital cost [67]. The operating conditions within the turbine are challenging due to high temperatures and the pressure difference between inlet and outlet. The main issue is

related to the thermal expansion of material during operation and the mechanical integrity during startup and shutdown.

The high operation pressures also lead to high densities, and corresponding low volumetric-flow rates in the system. This enables compact pipework and plants with a much smaller physical footprint, however, to design turbomachinery with high power density introduces challenges. Small diameter and higher rotational speed are associated with increased aerodynamic losses. A good combination of aerodynamics, rotordynamics and mechanical performance must be found. Both compressor and turbine are designed as axial or a centrifugal/radial-inflow architecture and can typically be sized using the maps developed by Balje [68]. A simple thermodynamic cycle analysis shows that increasing the pressure ratio of the cycle will increase the thermal cycle efficiency. The thermal cycle efficiency is sensitive to turbomachinery efficiency.

sCO_2 power plants have a high potential to operate efficiently in both full and part load. Fast load changes enable the power system to deliver backup power to the electricity grid. A lot of research has focused on the development of control strategies to address the part-loaded operation and the transient behaviour of sCO_2 systems during startup and shutdown. Dynamic modelling approaches have developed the understanding of transient performance [69–75]. Compressor and turbine are typically modelled using a map-based approach. The performance maps deliver the boundary conditions to the equipment upstream and downstream [76]. Heat exchangers are typically modelled with transient one-dimensional formulations of the conservation equations with semi-empirical correlations for both, heat transfer coefficient and pressure drop [77]. Control strategies can be applied to various parts of the cycle, such as heat sink flow rate, cooler bypass, compressor flow split, compressor bypass, turbine bypass, turbine throttling, turbine speed, single tank inventory and dual tank inventory. The control of the compressor inlet temperature may be achieved by acting on the heat sink at the cooler as the combination of heat sink flow rate and cooler bypass [78].

The purpose of thermodynamic modelling is to investigate how the cycle parameters, such as the operating temperatures and pressures, affect the thermodynamic cycle performance [3]. The simple recuperated cycle can be extended to more complex layouts with the implementation of **reheat, recompression or precompression**. The **reheat** cycle (Figure 3) divides the expansion process and introduces an intermediate

reheating process. This improves the cycle efficiency by increasing the temperature of heat addition and the turbine exhaust temperature, which pulls up the potential internal heat recovery.

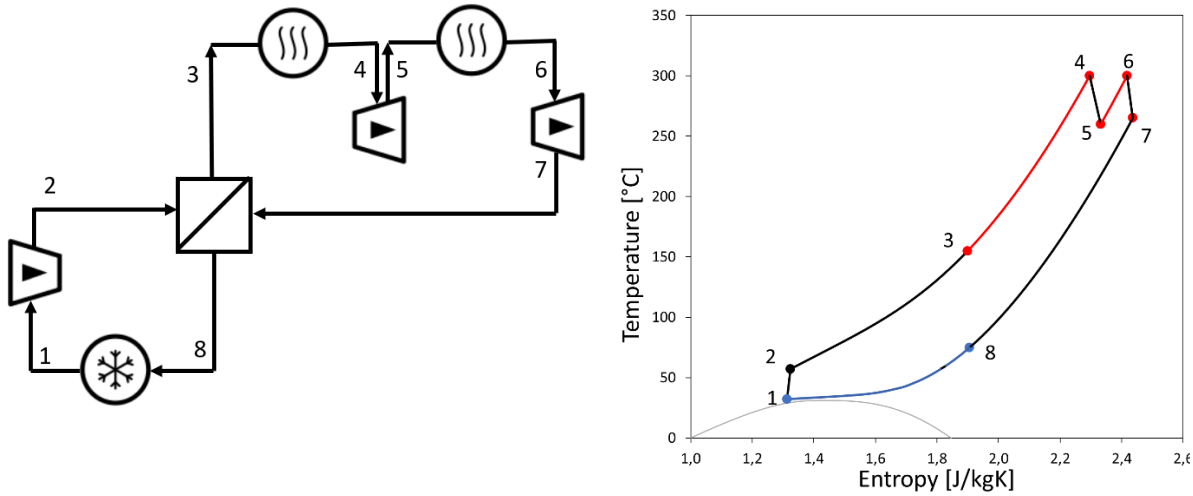

Figure 3: Cycle layout and T-s-diagram of a reheated Brayton cycle

The recompression cycle (Figure 4) is further increasing the cycle efficiency because it is still a relatively simple arrangement. The recuperation is divided into a high-temperature recuperator and a low-temperature recuperator section and a secondary compressor is installed. The compressor bypasses a fraction of the main flow from the heat-rejection process and main compressor. This helps to offset the mismatch in the heat capacities of the hot and cold fluids within the recuperators.

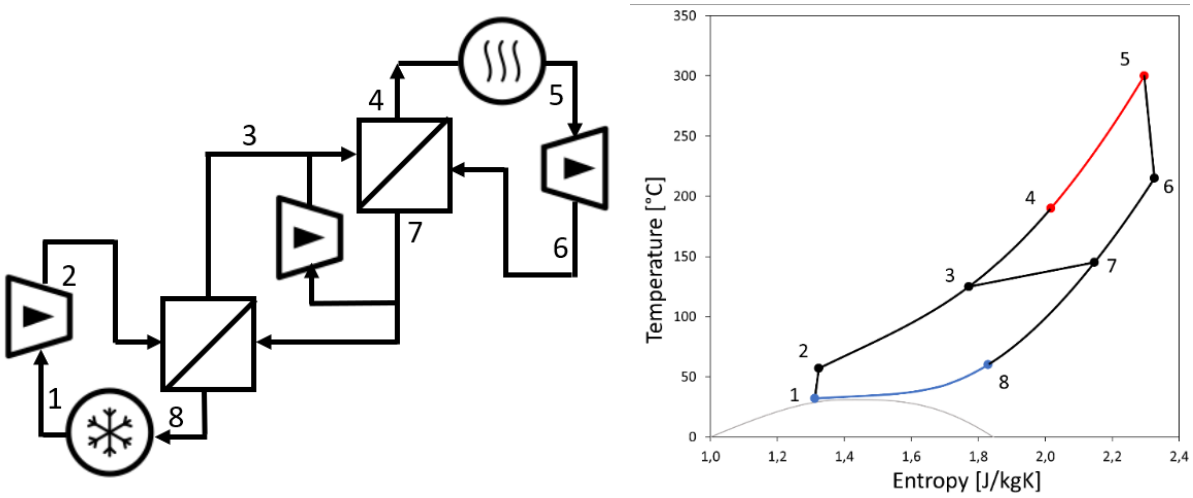

Figure 4: Cycle layout and T-s-diagram of a recompressed Brayton cycle

2.2 Industrial heat exchangers

In a sCO_2 Brayton cycle, the heat exchangers have a great influence on the overall efficiency and system size. The main challenge is to be compact, light, and robust to endure high CO_2 temperature and pressure. The applied type of heat exchanger compromises costs, durability, and performance. Three heat exchangers are involved in a sCO_2 Brayton cycle: heater, recuperator and cooler. In this chapter, possible heat exchanger solutions of both, recuperator and cooler are presented. Additionally, a review of the scientific research on each heat exchanger type is presented.

Printed circuit heat exchangers (PCHE) are the most used heat exchangers for recuperation [79]. The heat exchangers are manufactured using a solid-state joining process known as ‘diffusion bonding’. This process creates a heat exchanger core with no joints, welds or points of failure. The resulting unit combines exceptional strength and integrity with high efficiency and performance under conditions of extreme pressure and temperature [79; 67]. Figure 5 shows the cross-section of a PCHE core with a cross-flow pattern.

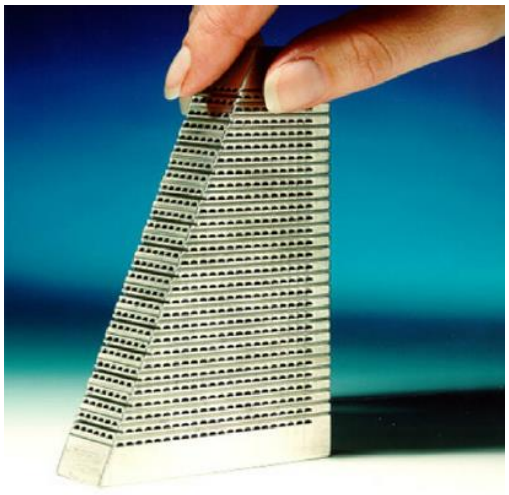

Figure 5: Printed Circuit Heat Exchanger [81]

The HX consists of several flat metal plates with fluid flow channels either chemically etched or pressed into them. The process joins the plates with strength as the base material. The flow passages are mainly categorized into four types and displayed in Figure 6:

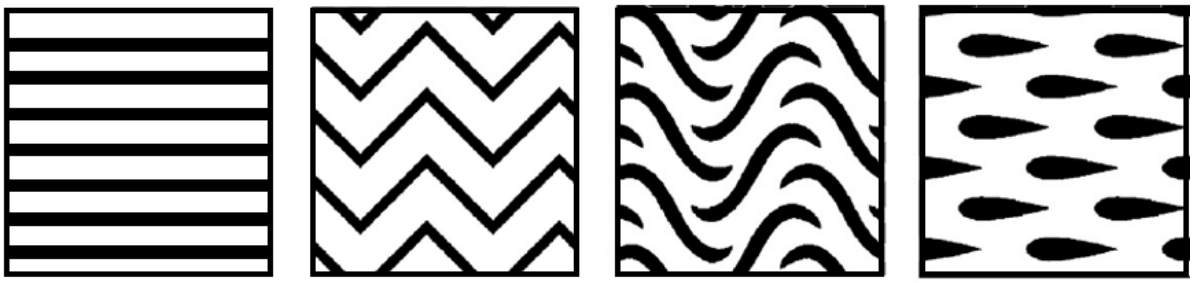

Straight Zigzag S-shaped Airfoil

Figure 6: Different types of PCHE [82]

The heat transfer and pressure drop have been investigated with various channel geometries and fluids under a wide range of conditions. Straight channels have been investigated by Mylavarapu et al. [9], Abraham et al. [10], Chen et al. [11] and Seo et al. [12]. Reynolds numbers between 100 and 2900 were covered with different types of heat transfer correlations. Nikitin et al. [13] experimentally investigated the pressure drop and heat transfer investigations with zig-zag channels and hydraulic diameter of 1.8 mm (cold side) and 1.9 mm (hot side). The overall heat transfer coefficient varied from 300 to 650 $\mathrm{W/m^2K}$, whereas the compactness for the heat exchanger volume is approximately 1050 $\mathrm{m^2/m^3}$. Empirical correlations for local heat transfer coefficient and pressure drop were proposed. Ngo et al. [14] optimized S-shaped fines by use of 3-D CFD simulations and validated his findings with experiments. This heat exchanger was used to heat water from 7 °C to 90 °C by using sCO_2 with a temperature of 118 °C and at a pressure of 115 bar. The pressure drop and internal volume of the new designed heat exchanger was significantly lower compared with a state-of-the-art industrial plate heat exchanger. Kim and No [15] investigated the thermal-hydraulic performance of a PCHE in helium–helium test loop, both experimentally and numerically. In the tested PCHE, the channel has a 0.922 mm hydraulic diameter, 24.6 mm pitch, and 15° angle. A three-dimensional numerical model was well validated against the experimental data to develop physical models for the Fanning factor and the Nusselt number for various geometries, including angle, pitch and diameter. The angle was varied from 5° to 45°, the pitch length was varied between 24.6 mm and 12.3 mm and the diameter was varied from 1.51 mm to 2 mm. Kim et al. [16] investigated the heat transfer and pressure drop in a PCHE with a numerical simulation to explore the validity of existing correlations beyond their tested Reynolds number ranges. Based on the comparison of CFD results with the experimentally obtained correlations, a new CFD-aided correlation covering an extended range of Reynolds

number for Nusselt number and friction factor is proposed to facilitate PCHE designs for the sCO_2 Brayton cycle application. Chen et al. [17] and Yoon et al. [18] investigated zigzag channels with helium as fluid and proposed Nusselt correlations with validity between Re of 50 and 2000. Tsuzuki et al. [19] investigated experimentally, both, water and CO_2 in S-shaped channels and compared the results with a numerical model. The numerical results of the heat transfer performance were about 5 % lower than the experimental results for the overall heat transfer coefficient. Therefore, the new Nusselt number correlations are useful to evaluate the experimental performance of the heat exchanger. Chu et al [20] investigated numerically the local and overall heat transfer characteristics as well as the dynamic performance of airfoil fins with different geometrical parameters. The result shows that the heat transfer rate decreases because of the strong variation of properties of sCO_2, but the pressure loss remains almost constant along the main flow direction. Meanwhile, the effect of transverse pitch and staggered longitudinal pitch are analyzed comprehensively. The correlations of Fanning and Colburn factors are fitted for the studied airfoil surfaces. Kwon et al. [21] performed CFD analysis for various airfoil fin configurations and provided correlations for predicting the Nusselt number and the Fanning friction factor. Optimization of the production and operation by reducing the size and the pressure drop of the recuperator suggested an optimized configuration of the airfoil fin PCHE. Ho et al. [22] combined an experimental study with numerical simulations to investigate the forced convective heat transfer performances of novel airfoil heat exchangers. Airfoil shaped fins were investigated experimentally and the results were compared with conventional heat sinks with circular and rounded rectangular fins. The experimental Nusselt number was enhanced by 29%. Zhao et al. [23] numerically investigated the effect of an airfoil fin arrangement on heat transfer and flow resistance using supercritical liquefied natural gas as a working fluid. The airfoil fin PCHE showed better thermal-hydraulic performance than that with the straight channel PCHE. Moreover, the airfoil fins with staggered arrangement displayed better thermal performance than that of the fins with a parallel arrangement. Chu et al. [24] investigated the thermo-hydraulic performance of printed circuit heat exchangers with airfoil fins. The results show that the arrangement with consistent and reverse layout applied to a PCHE may averagely improve the transferred heat per unit area by 28 % and 11 % accompanied with an increase of the pressure loss by 15 % and 22 %, respectively, compared to the PCHE with the symmetrical arrangement.

Cooler

The pressure and temperature in the cooler are lower than in the heater or in the recuperator. This leads to a much easier choice of material selection. The CO_2 is cooled by water or air what leads to many possible heat exchanger configurations. In air-driven coolers, the CO_2 close to the critical point has a much higher heat transfer coefficient than the cooling air. This makes the finned-tube heat exchanger design most appropriate [83; 8; 7]. The CO_2 flows in circular or flat tubes and the cooling air crosses the finned tubes where flat or continuous external fins are employed to increase the heat transfer surface area. Different types of fin and tube configurations are displayed in Figure 7.

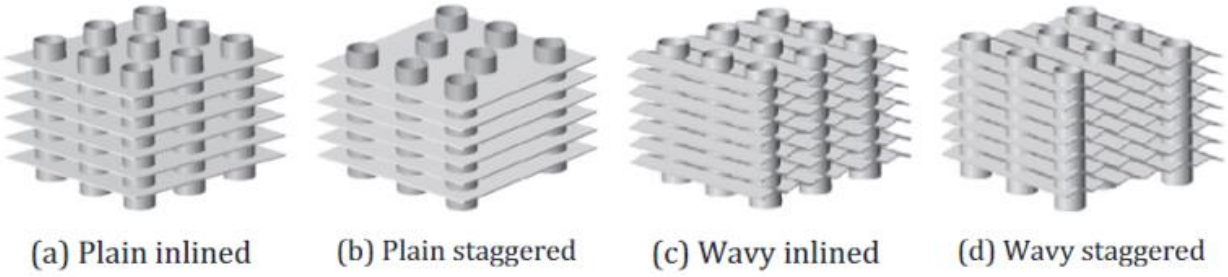

Figure 7: Different fin and tube arrangement [84]

Several investigators have carried out experimental tests and analyses of the heat transfer performance of finned-tube sCO_2 gas coolers. The majority of this work was focused only on steady-state analyses. Ge et al. [25] validated two different numerical models with measurements on two CO_2 finned-tube gas coolers with different structural designs. Li et al. [26] investigated a fin and micro-channel gas cooler experimentally. The impact of the fin geometry and air-side mal-distribution on the performance was analyzed. Ho et al. [27] present an experimental comparison between a microchannel cooler and two conventional coolers of a CO_2 air conditioning cycle. The conventional coolers and the microchannel cooler were designed to have the same heating capacity, however, the volume of the microchannel cooler is less than that of conventional coolers. The results indicate that the heat transfer efficiency of the microchannel cooler is higher than those of the conventional coolers. Yin et al. [28] developed a finite element method and compared the results with experiments at 48 operating conditions. The model predicted the gas cooler capacity within ±2 % and pressure drops on the CO_2 side well within the range of experimental error. Alternative circuiting and multi-

slab design were analyzed with the model. Vojacek et al. [29] investigated an air-cooled sCO_2 finned tube sink heat exchanger performance test comprising a wide range of variable parameters (26–166 °C, 70–100 bar, 100–32 g/s). They performed both steady-state and transient thermal-hydraulic using simulation software. The results of calculated averaged overall heat transfer coefficients and experimentally determined values show reasonably low errors.

A plate and fin heat exchanger (PFHX) is made of layers of corrugated sheets separated by flat metal plates to create a series of finned chambers. Separate hot and cold fluid streams flow through alternating layers of the heat exchanger and are enclosed at the edges by side bars. Heat is transferred from one stream through the fin interface to the parting sheet and the next set of fins into the adjacent fluid. The fins also serve to increase the structural integrity of the heat exchanger and allow it to withstand high pressures while providing an extended surface area for heat transfer [85]. Figure 8 illustrates the flow passages of a PFHX with straight fins in the counter flow.

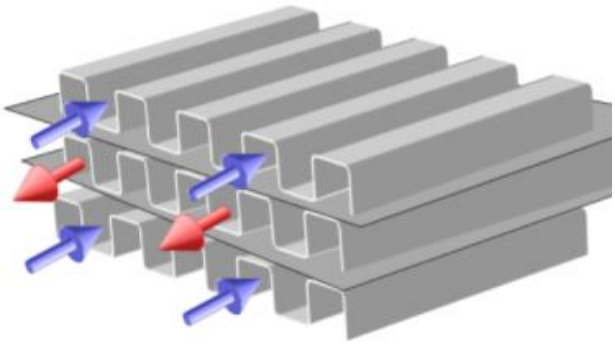

Figure 8: Plate and Fin heat exchanger in counter-flow arrangement [8]

A great number of experimental and numerical investigations were conducted in the last 40 years. A wide range of fluids under various operational conditions were tested with different types of fins which are displayed in Figure 9.

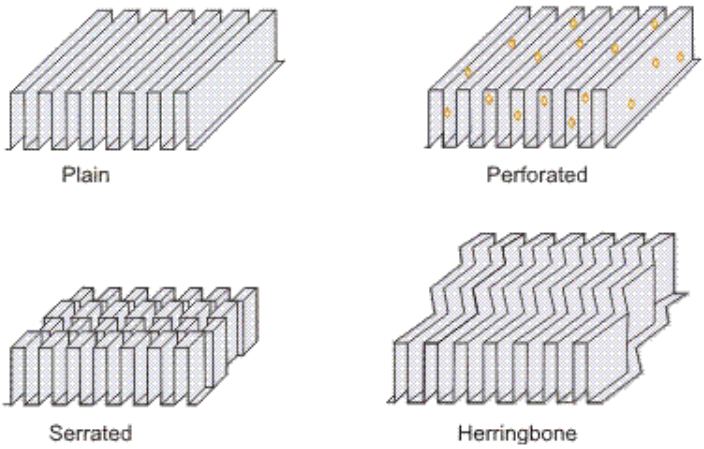

Figure 9: Different types of fins [30]

Manglik and Bergles [30] developed a thermal-hydraulic design tool for rectangular serrated fins. They reanalyzed the existing Fanning and Colburn data and showed the asymptotic behaviour of the data in the deep laminar and fully turbulent flow regimes. Geometric parameters were invented to design rational correlations by power-law equations covering the laminar, transition, and turbulent flow regimes. Ganzarolli [31] performed a thermal design optimization of a counterflow heat exchanger using air as the working fluid. The optimization was performed to obtain the optimum fin spacing and thickness. Li and Wang [32] investigated experimentally the air-side heat transfer and pressure drop characteristics for brazed aluminum heat exchangers with multi-region louvre fins and flat tubes. Experiments were conducted within a Reynolds number range from 400-1600 based on the louvre pitch. The air-side thermal performance data were analyzed by using the effectiveness-NTU method. Najafi et al. [33] optimized a plate and fin heat exchanger with air as a working fluid on both sides. Several geometric variables are considered as optimization parameters to match the total heat transfer rate and the total annual cost of the system. Fernández-Seara et al. [34] experimentally analyzed titanium brazed plate-fin heat exchanger with offset strip fins in liquid-liquid heat transfer processes with water and ethylene glycol aqueous solutions as working fluids. The Wilson plot method is applied to the reduction of the experimental heat transfer data and an empirical correlation for the heat transfer coefficient was obtained. Taler [35] presented an experimental–numerical method for determining heat transfer coefficients in crossflow heat exchangers with extended heat exchange surfaces. Coefficients in the correlations defining heat transfer on the liquid- and air-side were determined based on experimental data using a non-linear

regression method. Khoshvaght-Aliabadi [36] manufactured and tested seven plate-fin heat exchangers configurations: plain, perforated, offset strip, louvred, wavy, vortex-generator and pin. The working fluid was water and the Reynolds numbers range was from 480 to 3770. An energy-based performance evaluation criteria were employed. The vortex-generator channel shows a significant enhancement in the heat transfer coefficient and a proper reduction of the heat exchanger surface area. Peng et al. [37] conducted experimental and numerical studies on the flow and heat transfer characteristics for innovative offset strip fins compact heat exchangers. Five fin schemes were investigated with various air flow velocities and a constant inlet steam pressure by experiments. The Reynolds number ranged from 500 to 5000 at the air side. The experimental results indicated that the fin pitch, fin length and fin bending distance have a significant influence on the thermal performance of fins. Chen et al. [38] investigated numerically the effects of different plate-fin heat exchanger structures in high temperature gas-cooled reactors. Four fin structures and four working conditions were analyzed to evaluate the performance with detailed analyses of the velocity distributions, pressure distributions, temperature distributions and heat transfer. Kuchadiya et al. [39] evaluated the hydraulic behaviour of plate-fin heat exchangers with offset strip fin with conducting series of experiments. Different Mass flow rates of both the fluid, cold fluid inlet pressure and hot fluid inlet pressure are considered as input parameters. The obtained values were compared with correlations from the literature.

2.3 Thermophysical properties of sCO_2

In Figure 10, the phase diagram of CO2 is displayed. The pressure and temperature range of the solid, liquid and gaseous state are displayed. The boundaries are the sublimation, melting and boiling lines. All three regular states coexist at the triple point which is at p_{trip} = 5.18 bar and T_{trip} = -56.6°C. The pressure of the triple point is higher than the ambient pressure, which means that CO_2 can only appear in a gaseous or solid-state at ambient pressure. The boiling line is the connection of the triple point and the critical point (p_{crit} = 73.8 bar and T_{trip} = 31.0°C).

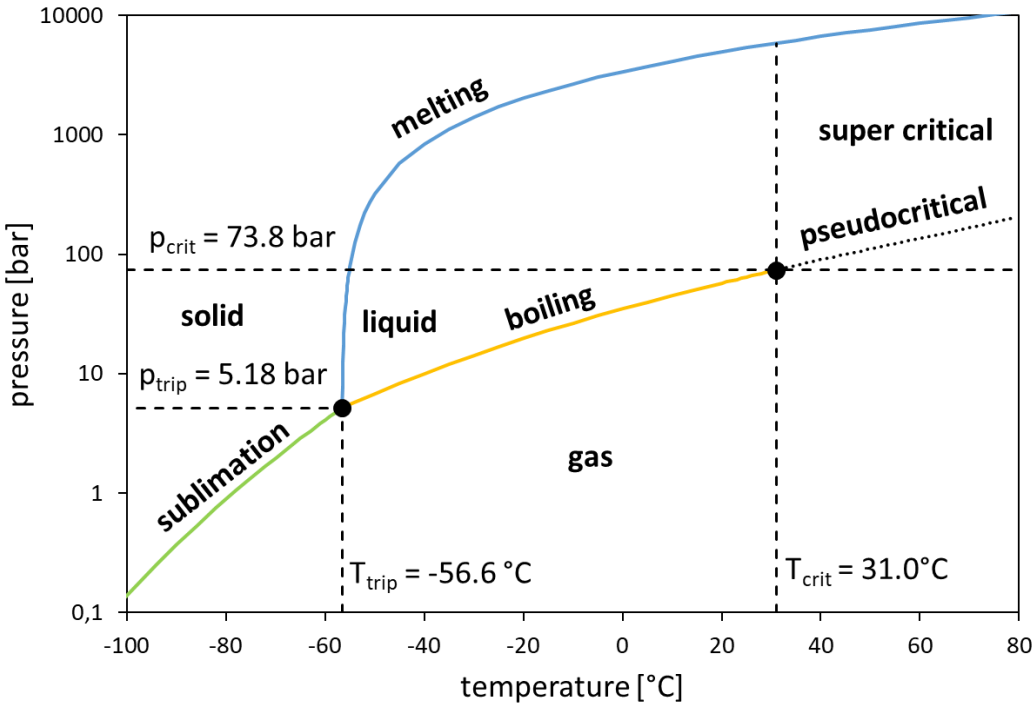

Figure 10: Phase diagram of CO2 [86]

The extension of the boiling line into supercritical temperature and pressure is so called the pseudocritical line, which is defined as the temperature with the highest gradient in viscosity and density and the peak in the isobaric heat capacity and thermal conductivity. The pseudocritical temperature is calculated with the empirical approximation as follows (Eq.1):

$$T_{pc}(p) = T_{crit}\left(1 + 1.3977\left(\frac{p}{p_{crit}} - 1\right) - 0.37344\left(\frac{p}{p_{crit}} - 1\right)^2 + 0.045\left(\frac{p}{p_{crit}} - 1\right)^3\right) \quad (1)$$

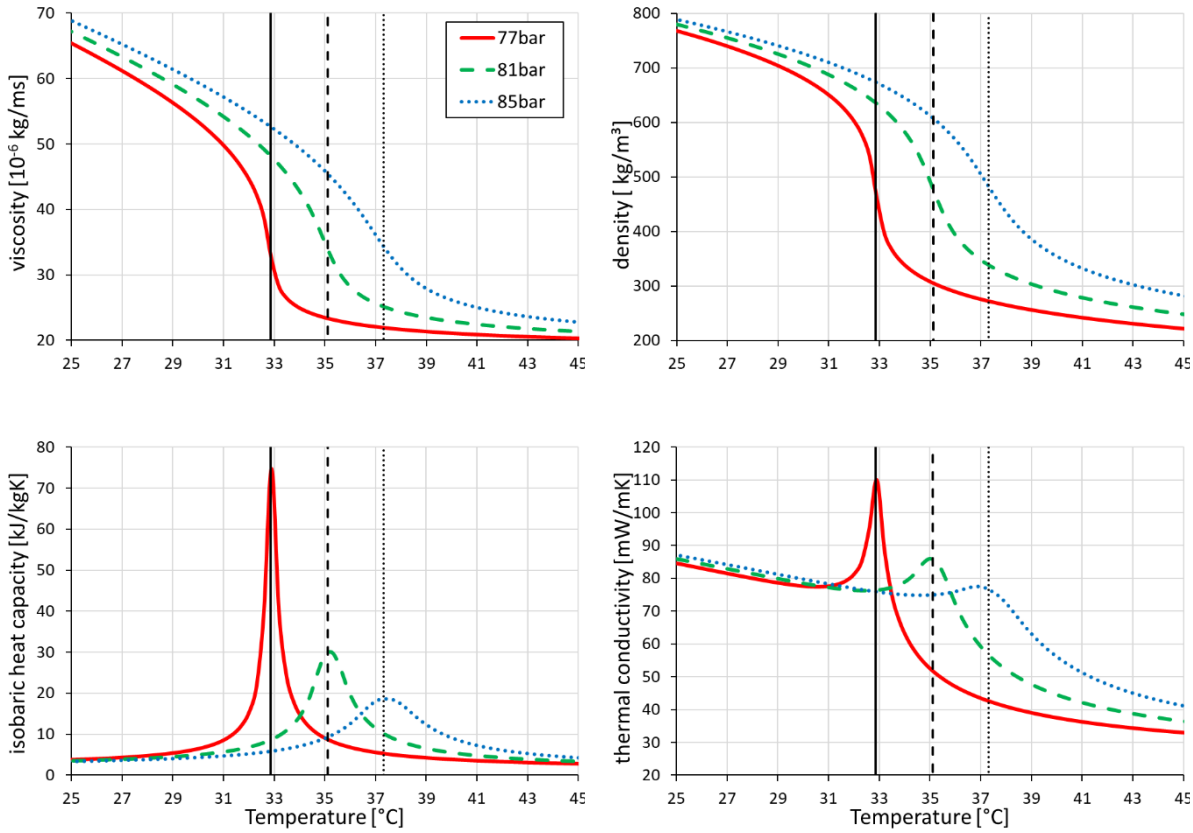

Figure 11: Thermophysical properties of CO2 at 77, 81 and 85 bar

The thermodynamic properties of CO_2 close to the critical point are illustrated in Figure 11. The viscosity, density, isobaric heat capacity and thermal conductivity are displayed as a function of the temperature for three different pressure (77, 81 and 85 bar). The properties were calculated using the software NIST REFPROP [86] which is the application of the following equations: Span and Wagner [87] (density, isobaric heat capacity), Vesovic et al. [88] (thermal conductivity) and Fenghour et al. [89] (viscosity).

The thermophysical properties change strongly with temperature and pressure. For each pressure (77, 81 and 85 bar), the viscosity and density are strongly decreasing with increasing temperature. The isobaric heat capacity and thermal conductivity pass through a peak crossing the pseudocritical temperature. The pseudocritical temperature increases with increasing pressure. Moreover, the distinct peaks are flattened.

2.4 Heat transfer and pressure drop in sCO2 tube flow

This chapter describes the state of the art of tube flow heat transfer and pressure drop starting with a general introduction which both kinds of research under heating and cooling conditions utilizing experimental and numerical work.In chapters 2.4.2 to 2.4.5, detailed information on the specific field of work is presented to illustrate the existing research gap.

2.4.1 Basic information

A great number of researchers have investigated supercritical heat transfer and pressure drop. Mainly from its application as a working fluid in nuclear power plants [40] or as rocket fuel [41], supercritical heat transfer has been investigated under heating conditions extensively. A lot of knowledge of sCO_2 heat transfer performance was gained in the heating case where the data for cooling is limited or does even not exist. Based on this, the chapter starts with a brief introduction of the heating case.

Experimental investigations have been carried out with sCO_2 flowing inside electrically resistance heated tubes with different inner diameters. A defined direct current is applied to the tube. The heat flux is the result of the tube cross-sectional area, the ohmic resistance, the voltage and the amperage. The heat flux can be assumed as constant over the length of the test section. A test section is displayed in Figure 12 including differential pressure measurement, power supply and surface temperature measurements with defined discretization.

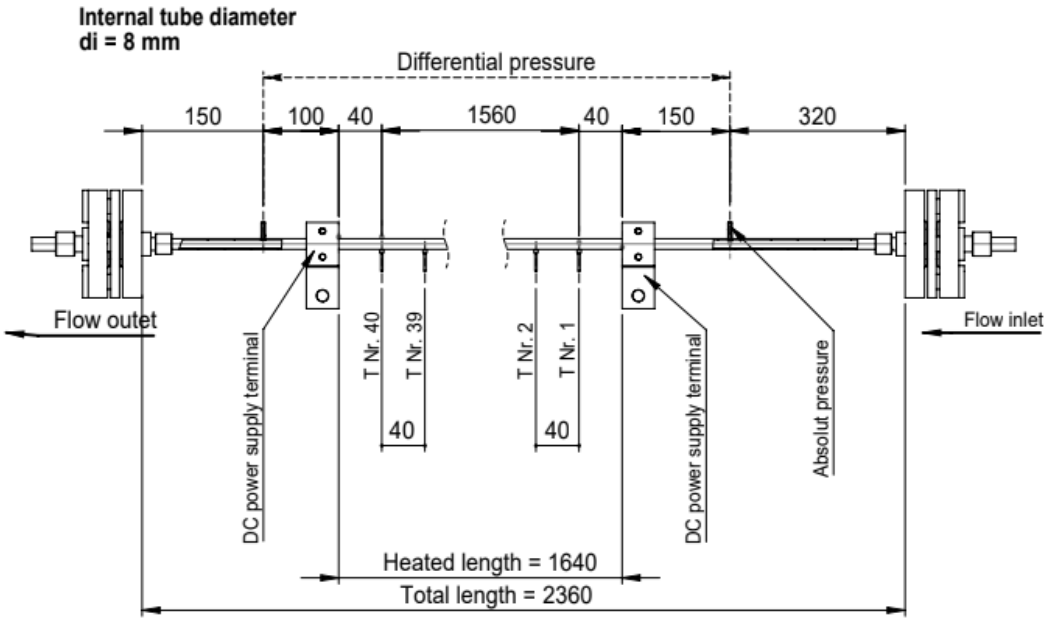

Figure 12: Heated tube with direct electrically heating [42]

With the defined inlet conditions and the constant heat flux along the tube, the bulk fluid enthalpy and temperature can be calculated at each subsection. The heat transfer coefficient at each subsection is then calculated using the difference between the bulk fluid temperature $T_{b,x}$ and the measured tube surface temperature $T_{w,x}$.

$$htc_x = \frac{\dot{q}_{const}}{T_{w,x} - T_{b,x}} \tag{2}$$

The results show that the heat transfer of sCO_2 is strongly affected by heat flux and flow direction. The development of mixed convection in the vertical upwards flow can lead to a drastic deterioration of the heat transfer performance which is characterized by a peak in the wall temperature [43]. The vertical downwards flow lead to an enhancement of heat transfer.

Song et al. [44] investigated tubes of 4.4 and 9.0 mm inner diameter with a heated length of 2 m. They showed that the same length to diameter ratio and wall heat flux to mass flux ratio leads to similar heat transfer behaviour. Kim and Kim [45] discussed the experimental results of a 4.5 mm diameter tube regarding buoyancy and flow-acceleration effects and showed a wall temperature peak in the upwards flow. Bae and Kim [46] carried out experiments with tubes of an inner diameter of 4.4 and 9.0 mm. From the test results, a correlation was published covering both, deteriorated and normal heat transfer. Zhang and Yamaguchi [47] studied numerically the heat transfer in a 6 mm diameter tube focusing on low mass flow rates and constant heat fluxes.

Cao et al. [48] discussed laminar mixed convection in miniature tubes with 0.5 mm diameter and points out the effects of the sharp variations of physical properties. Du et al. [49] investigated the velocity and turbulence fields using CFD simulation and concludes significant influences of buoyancy. Pandey and Laurien [50] suggested a two-layer model which can take deterioration into account.

For the cooling case, several researchers have investigated experimentally and numerically the heat transfer and pressure drop performance of sCO_2 in tubes of different sizes. The main focus was on the horizontal flow in tubes ranging from 0.5 to 10.7 mm inner diameter.

Pitla et al. [51] investigated the cooling heat transfer on a 4.7 mm inner diameter tube. They found out that the heat transfer coefficient in supercritical fluids is not constant and varies as a function of the wall temperatures and the bulk temperatures of the fluid. A new equation was presented based on the properties at the wall and the bulk temperature. 85% of the heat transfer coefficient values predicted by the new correlation were accurate within ± 20%. Nu_w and Nu_b are the Nusselt number calculated based on Gnielinski correlation [90] in Eq.4.

$$\mathrm{Nu} = \left(\frac{\mathrm{Nu_w} + \mathrm{Nu_b}}{2}\right)\frac{\lambda_\mathrm{w}}{\lambda_\mathrm{b}} \tag{3}$$

$$\mathrm{Nu} = \frac{\left(\frac{\mathrm{f}}{8}\right)(\mathrm{Re} - 1000)\mathrm{Pr}}{1{,}07 + 12{,}7\sqrt{\frac{\mathrm{f}}{8}}\left(\mathrm{Pr}^{\frac{2}{3}} - 1\right)} \tag{4}$$

Yoon et al. [52] measured the heat transfer and pressure drop of a 7.73 mm diameter tube with variations in CO_2 mass flux and CO_2 pressure. Mass fluxes were 225, 337 and 450 $\mathrm{kg/m^2}s$ and the inlet pressures varied from 75 to 88 bar. Existing correlations for the supercritical heat transfer underpredicted the measured values. A new empirical correlation was presented with a maximum deviation of 20 %. Nu_w is calculated based on the Gnielinski correlation [90] in Eq.5:

$$Nu = 1{,}38\, Nu_w \left(\frac{\bar{c_p}}{c_{pw}}\right)^{0{,}86} \left(\frac{\rho_w}{\rho_b}\right)^{0{,}57} \tag{5}$$

In this context, the mean specific heat is defined as:

$$\bar{c_p} = \frac{h_b - h_w}{T_b - T_w} \tag{6}$$

with the enthalpy and temperature of CO_2 at the wall (h_w, T_w) and in the bulk (h_b, T_b). Oh and Son [53] conducted experiments on two stainless steel circular tubes having an inner diameter of 4.55 mm and 7.75 mm and carried out for CO_2 mass fluxes of 200 to 600 kg/m^{2}s, inlet fluid pressures of 75 to100 bar, and the inlet fluid temperatures of 90 to 100 °C. The CO_2 pressure, the inner tube diameter, the mass flux and the temperature of CO_2 showed significant effects on the heat transfer coefficient. The heat transfer coefficient decreases as the cooling pressure increase otherwise increase as mass flux increases. Most heat transfer correlations show large deviations from these experimental data, thus, a new correlation was developed for sCO_2 cooling in macro tubes. Most of the experimental values are within ±13 % of the predicted values. The correlation is based on the Dittus and Boelter equation [91] with additional ratio terms of the fluid properties at bulk and wall temperature (Eq.7-8):

$$Nu_b = 0{,}023\, Re_b^{0,7} Pr_b^{2,5} \left(\frac{c_{pb}}{c_{pw}}\right)^{0,411}, \text{for } T_b > T_{pc} \tag{7}$$

$$Nu_b = 0{,}023\, Re_b^{0,7} Pr_b^{2,5} \left(\frac{\rho_b}{\rho_w}\right)^{3,7} \left(\frac{c_{pb}}{c_{pw}}\right)^{-4,6}, \text{for } T_b < T_{pc} \tag{8}$$

Liu et al. [54] investigated the cooling heat transfer of a wide range of tube diameters (d_i= 4, 6, 10.7 mm). The effects of the CO_2 mass flow rate, inlet pressure, bulk temperature and tube diameter on the heat transfer coefficient and pressure drop were illustrated. The results indicated a significant influence of the tube diameter on the heat transfer coefficient. The authors show that heat transfer correlations for the small diameter tube deviate strongly from the experimental results. A new heat transfer correlation for large diameter tubes was proposed. The maximum error between the predicted results of the new correlation and the experimental data is 15% (Eq.9).

$$Nu_w = 0{,}01\, Re_w^{0,9} Pr_w^{0,5} \left(\frac{\rho_w}{\rho_b}\right)^{0,906} \left(\frac{c_{pw}}{c_{pb}}\right)^{-0,585} \tag{9}$$

Kondou and Hrnjak [55] investigated the heat transfer in the two-phase region. Experimental results on the heat transfer coefficient and pressure drop of mass flux

from 100 to 240 kg/m^{2}s at pressures from 50 to 75 bar in a horizontal smooth tube of 6.1 mm inner diameter were provided and compared with correlations. The heat rejection process below the critical pressure was categorized into superheat, two-phase, and sub cool zones in which the bulk temperature was superheated, saturated, and subcooled, respectively. The results indicated that the heat transfer coefficient in the superheat zone is significantly higher than correlations proposed for single-phase turbulent flow, and the condensation was identified from the tube wall temperature below saturation temperature. This superheat zone accounts for a significant portion of the heat rejected in the subcritical cycle and effects on condenser sizing.

In recent years, numerical investigations have increasingly contributed to the understanding of the cooling heat transfer of sCO_2. Pandey et al. [56] conducted direct numerical simulations of a 2 mm diameter tube at a moderate Reynolds number of 5400. Xiang et al. [57]carried out simulations by using the SST k-ω turbulence model and discussed the effects of heat flux and tube diameter on the heat transfer characteristics.

Especially, it has been shown that heat transfer correlations which were developed for big diameter tubes are not able to predict the heat transfer of small diameter tubes accurately. Thus, only two experimental investigations are presented in chapter 2.4.2 for the use as a reasonable comparison of the results with small diameter tubes.

2.4.2 Forced convection cooling heat transfer

Dang and Hihara [58] investigated the heat transfer and pressure drop in tubes with four different inner diameters (d_i= 1; 2; 4; 6 mm). The temperature of the outer tube wall was measured at 10 locations evenly distributed along with the 500 mm long tube-in-tube counter-flow heat exchanger. They found that the Nusselt number increases slightly with increasing tube diameter. The authors compared the heat transfer coefficient over the bulk (T_b) and film temperatures (T_f), which is defined as the average of bulk and wall temperature (T_w)(Eq.10):

$$\mathrm{T_f} = \frac{(\mathrm{T_b} + \mathrm{T_w})}{2} \qquad (10)$$

The comparison of the heat transfer data in Figure 13 and Figure 14 shows that the maximum heat transfer coefficient is considered when the film temperature reaches the pseudocritical temperature.

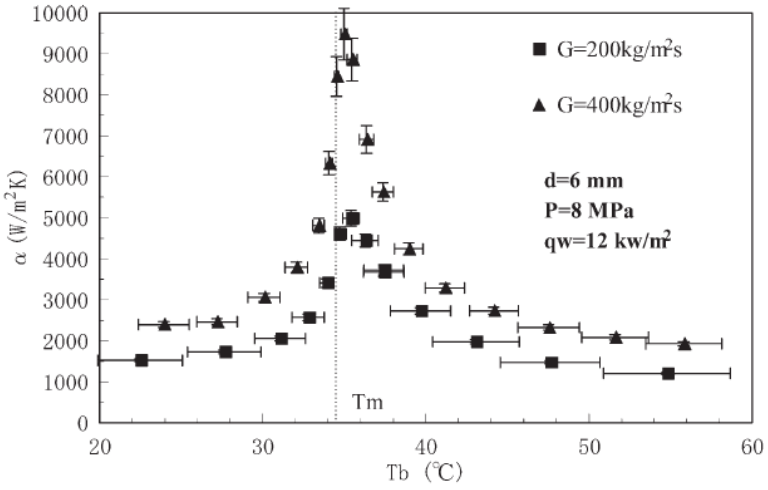

Figure 13: Effect of mass flux G on heat transfer coefficient as a function of bulk temperature [58]

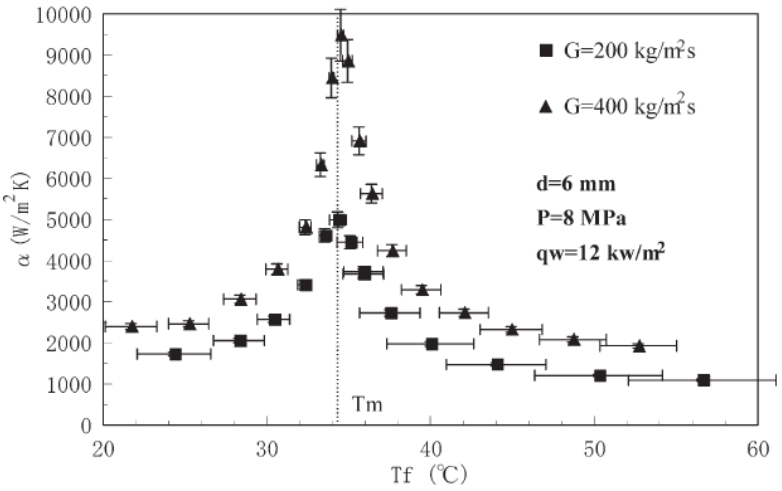

Figure 14: Effect of mass flux G on heat transfer coefficient as a function of film temperature. The dashed line denotes the pseudocritical temperature at a pressure of 8 MPa [58]

The proposed correlation by the authors is a modified Gnielinski equation [90] taking the film properties into account:

$$\mathrm{Nu_f} = \frac{\left(\frac{\xi}{8}\right)(\mathrm{Re_b} - 1000)\mathrm{Pr}}{1{,}07 + 12{,}7\sqrt{\frac{\xi}{8}}\left(\mathrm{Pr}^{\frac{2}{3}} - 1\right)} \qquad (11)$$

Liao and Zhao [59] experimentally investigated the heat transfer in six horizontal tubes (d_i= 0.5, 0.7, 1.1, 1.4 , 1.55, 2.16 mm). The experimental test section consisted of a cooled tube of 110 mm length with 6 uniformly distributed thermocouples at the outer wall. They showed the dependency of the heat transfer coefficient from the bulk temperature, pressure and mass flow. They found that the Nusselt number depends on the tube diameter due to buoyancy effects (Figure 15). The Grashof number (Eq.12) was considered, representing the influence of a secondary flow induced by the buoyancy force.

$$Gr = \frac{(\rho_w - \rho_b)\rho_b g d^3}{\eta_b^2} \qquad (12)$$

with the density of CO_2 at the wall (ρ_w) and in the bulk (ρ_b), the gravity constant (g), the pipe inner diameter (d) and the dynamic viscosity in the bulk (η_b).

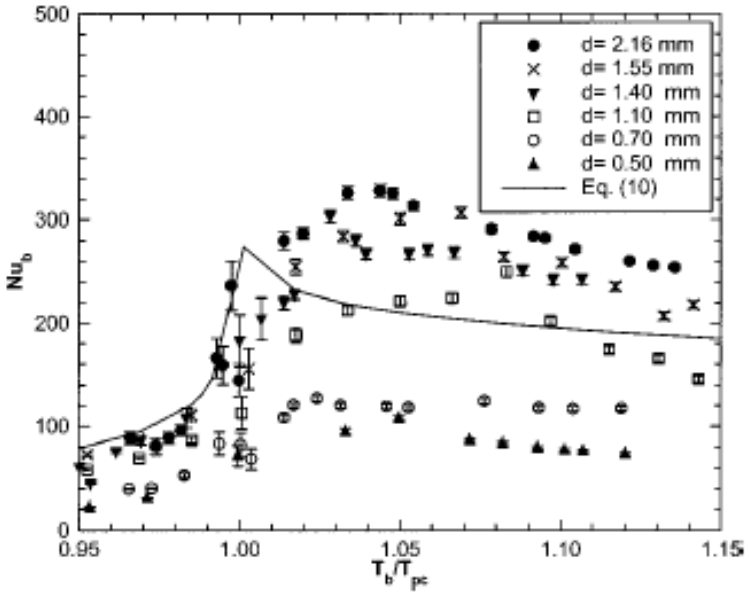

Figure 15: The effect of tube diameters on the Nusselt number Nu_b at $\frac{m}{d} = 1.19\ \frac{kg}{ms}$ [59]

The influence of different cooling water temperatures (T_{cool}) has been shown and drawn back to the temperature difference between CO_2 bulk and wall temperature. The correlation (Eq.13) was built up as a variation of the Dittus and Boelter equation [91] by multiplying it with ratio terms including the properties of the fluid at the wall temperature. The Nusselt function becomes implicit by adding these terms.

$$Nu_w = 0{,}128\, Re_w^{0,8} Pr_w^{0,3} \left(\frac{Gr}{Re_b^2}\right)^{0,205} \left(\frac{\rho_b}{\rho_w}\right)^{0,205} \left(\frac{\bar{c_p}}{c_{pw}}\right)^{0,411} \qquad (13)$$

2.4.3 Buoyancy and acceleration effects in vertical flow orientation

Different heat transfer mechanisms can be observed in the supercritical fluid flow. The enhanced (EHT), normal (NHT) and deteriorated heat transfer (DHT). The differences between the three mechanisms are explained by experiments in a heated upwards tube flow with constant mass flux and increasing heat flux.

In Figure 16, the measured inner wall temperature is displayed as a function of the bulk fluid enthalpy. The grey line is the reference as the bulk fluid temperature at the respective fluid pressure. In the NHT (red), the wall temperature has a nearly constant difference from the bulk fluid temperature. In contrast to the NHT, the EHT shows a non-constant approximation to the bulk fluid temperature with a very low difference close to the pseudo-critical temperature. The DHT occurs with a further increase of the heat flux. The wall temperature of the tube deviates significantly from the course of the bulk fluid temperature. The temperature difference between the wall and the bulk fluid increases significantly and the wall temperature shows a local peak in the region below the pseudocritical temperature.

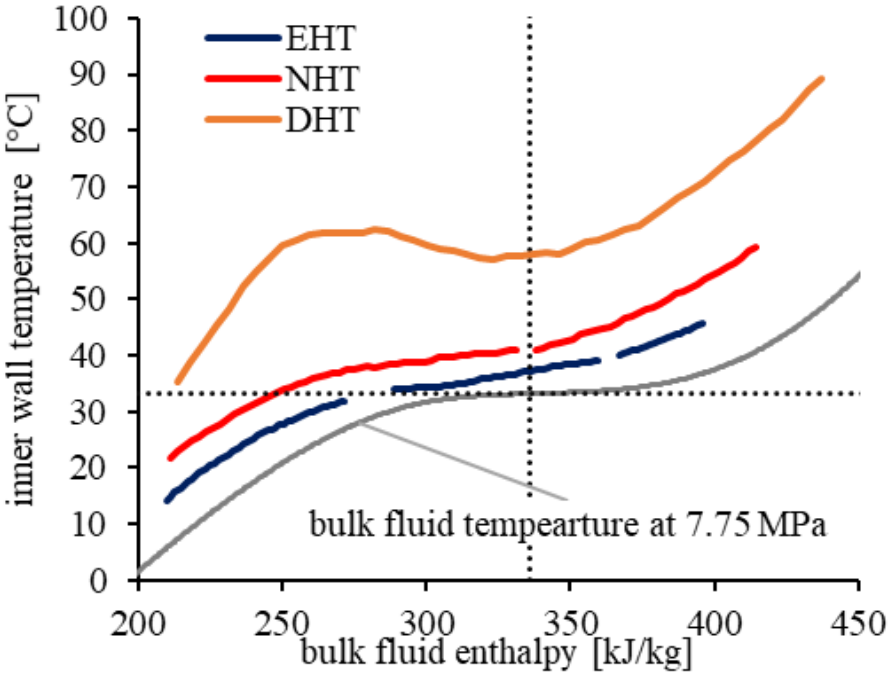

Figure 16: Classification of heat transfer based on the wall temperatures [92]

In fluid flow, a drastic deterioration of the heat transfer can occur. In the case of heating, it can be detected by the strongly increased wall temperatures. The mechanisms to cause the deterioration are due to the strongly variable fluid properties of sCO_2 close to the critical point. The flow acceleration and buoyance based on the flow direction are the main influencing factors. In the cooling case, the upwards flow is by tendency enhanced and the downwards flow deteriorates. Figure 17 illustrates the qualitative velocity profiles of an upward (left) and a downward flow (right). The forced convection shapes a parable-like profile with a flat spike (2, red) while the natural convection shapes an M-shape profile (3, blue). In the case of a downwards flow, the natural and forced convection have the same direction, thus the effect of buoyancy leads to higher velocities in the near-wall layer and the resulting profile is also an M-shape. In this case, the differential velocity between the near-wall layer and the bulk fluid decreases with the result of a lower heat transfer between these two regions. In the case of an upwards flow the natural and the forced convection run in opposite directions with the result of increasing the turbulence which leads to a better heat transfer between the near-wall layer and the bulk fluid [93]. Kurganov and Kaptilny [94] validated the velocity profiles experimentally.

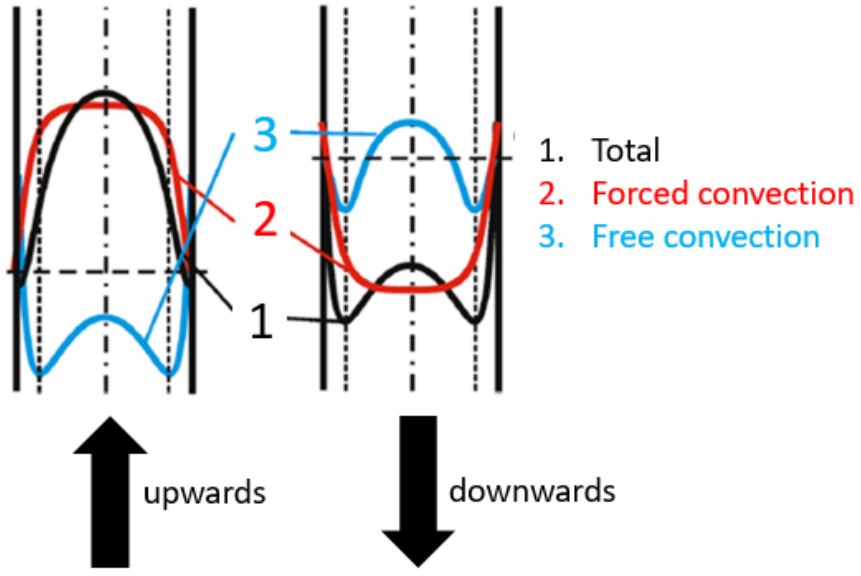

Figure 17: Deteriorated heat transfer based on the fluid flow velocity [93]

The onset of deterioration in sCO_2 heat transfer was investigated in the heating case by several researchers. The research on sCO_2 heating in direct electrical heated tubes lead to the development of criteria for the deterioration of heat transfer in vertical flow.

The criterion by Petukhov et al. [95] is based on the effect of flow acceleration and predicts that the region of the NHT is determined by the ratio of the acceleration resistance, to the friction resistance which has to be smaller than 1-1.3 (Eq.14-16)

$$\left(\frac{\xi_e}{\xi}\right)_{max} \leq 1 - 1.3 \tag{14}$$

$$\xi = \left(\frac{\rho_w}{\rho_b}\right)^{0.4} \left(1.82 \log\left(\frac{Re_b}{8}\right)\right)^2 \tag{15}$$

$$\xi_u \cong 8\, \dot{q}_b^+ \tag{16}$$

The non-dimonsional heat flux $\dot{q}_b^+$ is defined by McEligot and Jackson [43] in Eq.17:

$$\dot{q}_b^+ = \frac{\dot{q}\beta_b}{c_{p,b}G} \tag{17}$$

The criterion by Jackson et al. [96] is based on a semi-empirical parameter which considers the comparison between the buoyancy force and the inertial force based on the Richardson number (Eq.18):

$$Ri = \frac{Gr}{Re^2} \tag{18}$$

Using this parameter, mixed convection has a significant effect on heat transfer when:

$$\frac{\overline{Gr_b}}{Re_b^{2.7}} \geq 10^{-5} \tag{19}$$

The Grashof number is calculated as:

$$\overline{Gr_b} = \frac{(\rho_b - \bar{\rho})gd^3}{\rho_b\, \nu_b^2} \tag{20}$$

The average density of the fluid $\bar{\rho}$ can be calculated based on an approximation proposed by Bae and Yoo [97](Eq.21-22):

$$\bar{\rho} = \frac{1}{T_w - T_b} \int_{T_b}^{T_w} \rho dT \tag{21}$$

$$\bar{\rho} \approx \begin{cases} \dfrac{(\rho_w + \rho_b)}{2} \; for \; T_w > T_{pc} \; or \; T_b < T_{pc} \\ \dfrac{\left[\rho_b\left(T_b - T_{pc}\right) + \rho_w\left(T_{pc} - T_w\right)\right]}{T_b - T_w} \; for \; T_w < T_{pc} < \; T_b \end{cases} \quad (22)$$

Another buoyancy based criterion was published by McEligot and Jackson [43], with the buoyancy parameter Bo^* (Eq.23) described by the heat flux based Grashof number Gr^* (Eq.24):

$$Bo^* = \frac{Gr^*}{Re_b^{3.425} Pr^{0.8}} > \sim 6 * 10^{-7} \quad (23)$$

$$Gr^* = \frac{g \, \beta_b \dot{q} d_i^4}{\lambda_b \nu_b^2} \quad (24)$$

Other criteria use the heat flux to mass flux ratio to indicate the onset of DHT. The criterion by Jeon et al. [98] is investigated in CO_2 flow (Eq.25). The others in water flow (Eq.25-28).

Jeon et al. [98]	$\dot{q} = 0.2 \, G^2$	(25)
Yamagata [99]	$\dot{q} = 200 \, G^{1.2}$	(26)
Pioro et al. [100]	$\frac{\dot{q}}{G} \geq 400 \, \frac{J}{kg}$	(27)
Styrokovich et al. [101]	$\frac{\dot{q}}{G} \geq 600 \, \frac{J}{kg}$	(28)

Further experimental and numerical investigations are ongoing to validate and improve the criteria and equations [92; 102; 103].

Jiang and Zhao [104] investigated the heat transfer in a vertical 2 mm diameter tube with a combination of experimental measurements and numerical simulations. The results showed that the local heat transfer coefficients vary significantly along the tube when the CO_2 bulk temperatures are close to the pseudo critical temperature.

Experimental work in vertical sCO_2 cooling

Bruch et al. [105] investigated experimentally the cooling heat transfer of sCO_2 in a vertical copper tube with an inner diameter of 6 mm. They were the only authors who applied a deterioration criterion to the cooling heat transfer.

The test section consists of two vertical tube-in-tube heat exchangers connected in series employing a U-bend. In the experiment, the in- and outlet temperature of CO_2 and cooling media were measured and treated with an integral method to determine the heat transfer coefficient. The semi-empirical parameter ($Gr/Re^{2.7}$) by Jackson and Hall [106] was applied to characterize the influence of natural convection on turbulent vertical flow. The heat transfer in the vertical flow is compared with a correlation of pure forced convection heat transfer.The selected correlation is the one by Jackson and Hall [106]:

$$\mathrm{Nu}_{fc} = 0.0183 Re_b^{0.82} \overline{Pr}_b^{0.5} \left(\frac{\rho_b}{\rho_w}\right)^{-0.3} \quad (29)$$

The results of the experimental investigation were plotted in dimensionless form (Figure 18). The resulting functions of the downwards stream are the following (Eq.30-31):

$\frac{Gr}{Re^{2.7}} < 4.2 \cdot 10^{-5}$: $\frac{Nu_b}{Nu_{FC}} = 1 - 75 \left(\frac{Gr}{Re^{2.7}}\right)^{0.46}$ (30)

$\frac{Gr}{Re^{2.7}} > 4.2 \cdot 10^{-5}$: $\frac{Nu_b}{Nu_{FC}} = 13.5 \left(\frac{Gr}{Re^{2.7}}\right)^{0.40}$ (31)

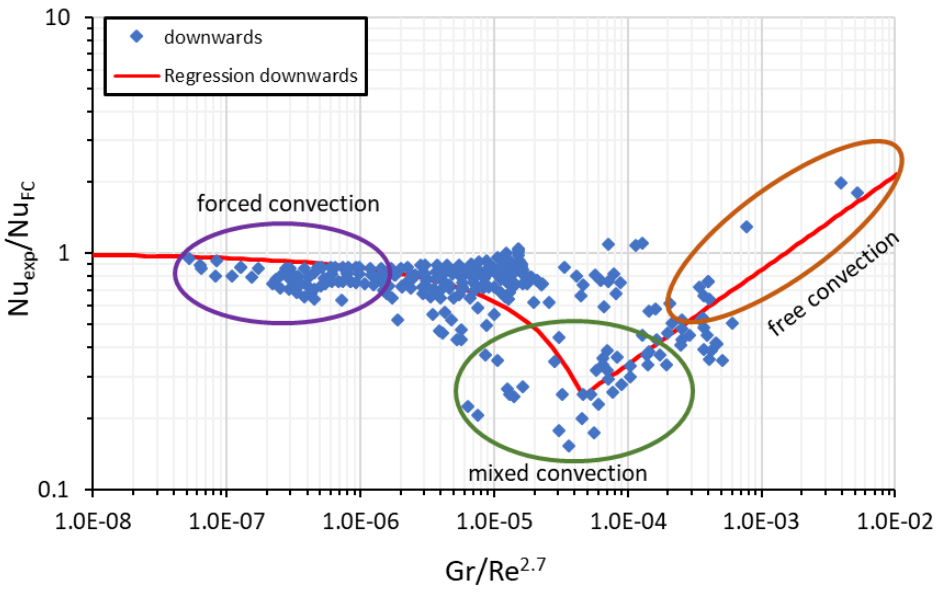

Figure 18: Evolution of Nusselt number with the mixed convection parameter by Bruch et al. [105]

The region of forced convection is present at $\mathrm{Gr}/\mathrm{Re}^{2.7} < 10^{-6}$ with only a little difference to unity. In this region, free convection can be neglected and the general applicability of the forced convection Nusselt equation can be tested. With increasing mixed convection parameters, the heat transfer deteriorates can be seen by a negative gradient of the red line. The strongest deterioration is present in the mixed convection area which is the turning point of the red line. With further increase of the mixed convection factor, the flow regime converts to free convection which a noticeable recovery of the heat transfer in this area.

2.4.4 Buoyancy effects in horizontal flow orientation

An important role in the heat transfer with supercritical fluids plays the buoyancy and the resulting temperature stratifications in horizontal flow. The temperature difference in the heat transfer process between the wall and bulk fluid leads to strong density differences. This causes secondary flows based on gravity and buoyancy. It is known that the buoyancy effect in the flow might not be neglected even for a horizontal test section at high Reynolds numbers [59].

Different buoyancy parameters are suggested in the literature to estimate the significance of the effect of buoyancy on the heat transfer coefficient in a horizontal pipe flow. Three criteria are available in the literature. A theoretical consideration is based on the Richardson number (Eq.32), which is the ratio between buoyancy- and inertia force. The criterion states the region of neglectable buoyancy effects:

$$Ri = \frac{Gr}{Re^2} \ll 10^{-3} \tag{32}$$

Adebiyi and Hall [107] investigated experimentally the heat transfer of sCO_2 in a heated pipe with an inner diameter of 22 mm. The results were compared with the estimated values from the empirical correlation without including buoyancy effects. Buoyancy effects were detected despite Reynolds numbers above 10000 at the inlet of the tube. Temperature differences up to 50 K were detected between the top and the bottom tube wall. The heat transfer was deteriorated at the top and enhanced at the bottom. Based on the experimental findings, the dimensionless buoyancy free region criterion Bu was developed considering the dimensionless tube length $\left(\frac{x}{d}\right)$ and the property variation between bulk fluid and wall $\left(\frac{\rho_\mathrm{b}}{\rho_\mathrm{W}}\right)$:

$$Bu_J = \frac{Gr_\mathrm{b}}{Re_b^2} \cdot \left(\frac{\rho_\mathrm{b}}{\rho_\mathrm{W}}\right) \cdot \left(\frac{x}{d}\right)^2 < 10 \tag{33}$$

Petukhov et al. [95] proposed a criterion for the buoyancy free region in horizontal flow as:

$$Bu_\mathrm{P} = \frac{Gr_\mathrm{b}^*}{Re_\mathrm{b}^{2,75}}\, Pr_\mathrm{b}^{-0.5} \cdot \left[1 + 2{,}4 \cdot Re_\mathrm{b}^{-1/8} \cdot \left(Pr_\mathrm{b}^{2/3} - 1\right)\right]^{-1} < 3 * 10^{-5} \tag{34}$$

Du et al.[49], Lin et al.[108] and Diao et al.[109] confirmed that the buoyancy effects are distinct close to the pseudocritical temperature. In addition to that, the temperature stratification is negligible in comparison to the liquid-like and gas-like region. Cao et al [48] investigated experimentally laminar flow of sCO_2 in a microchannel with constant wall temperatures with a numerical simulation. Secondary flow appeared in accordance with the criterion $\mathrm{Ri} < 10^{-3}$. Du to the buoyancy effects and an existing temperature stratification, the heat transfer in the upper part of the tube was strongly enhanced while in the bottom part of the tube the heat transfer was slightly deteriorated. This effect was strongest close to the critical temperature. Tanimizi and Sadr [110] investigated the buoyancy criterions $\mathrm{Bu_{AH}}$, $\mathrm{Bu_P}$ and $\mathrm{Ri} < 10^{-3}$ with experiments in sCO_2 on their validity. They concluded that all criterions predict the local heat transfer deterioration. In contrary to that, Kim et al.[111] showed that only Bu_{AH} and $\mathrm{Ri} < 10^{-3}$ are able to predict the appearance of buoyancy effects. A limitation is present for the Jackson criterion at low heat fluxes. In addition to that the heat transfer was deteriorated in the top of the tube for all experiments and at low heat fluxes an enhanced heat transfer in the bottom tube occurred.

2.4.5 Experimental investigations of tube flow pressure drop

The pressure drop within a tube is defined as follows in Eq.35:

$$\Delta p = \xi \frac{l}{d} \frac{\rho u^2}{2} = \xi \frac{l}{d} \frac{G^2}{\rho} \quad (35)$$

considering the dimensionless friction factor ξ, the length l and the diameter d of the tube, the density ρ and the velocity u and the mass flux G. The fundamental equations of the friction factor in turbulent tube flow can be summarized by the following Equations from the VDI Heat Atlas [112]. The Blasius equation is valid within the range of Reynolds 3000 – 100000 (Eq.36):

$$\xi = \frac{0{,}3164}{\sqrt[4]{Re}} \quad (36)$$

For higher Reynolds numbers $10^4 \leq Re_i \leq 10^6$, the Konakov correlation (Eq.37) is valid.

$$\xi = \frac{1}{(1.8 \lg Re - 1.5)^2} \quad (37)$$

At Reynolds number of $10^5 \leq Re_i \leq 5 * 10^7$, the Filonenko correlation (Eq.38) is valid.

$$\xi = \frac{1}{(1.819 \lg Re - 1.64)^2} \quad (38)$$

For the turbulent flow in the region of plain and rough surfaces to following Eq.39 is valid:

$$\frac{1}{\sqrt{\xi}} = -2 \lg \left[\frac{2{,}51}{Re_i \sqrt{\xi}} + \frac{K/d_i}{3{,}71} \right] \quad (39)$$

by consideration of the roughness of tube K. The correlations in Eq.36-39 is fundamental for pressure drop investigations. The experimental pressure drop and friction factor of sCO_2 were in the first instance compared with these correlations. New correlations with better predictability of sCO_2 cooling were mainly built up based on these equations by adding ratio terms of the fluid properties. Petrov and Popov [113] published a correlation for cooling of sCO_2 in tubes in 1985. The tube roughness was not considered in his correlation (Eq.40-42):

$$\xi_w = [1.82 \log(Re_w) - 1.64]^{-2} \quad (40)$$

$$s = 0.023 * \left(\frac{q}{G}\right)^{0.42} \quad (41)$$

$$\xi = \xi_w \frac{\rho_w}{\rho_b} \left(\frac{\eta_w}{\eta_b}\right)^s \quad (42)$$

Liao and Zhao [59] investigated the variation of the friction factor f with the Reynolds Number for d_i = 0.50, 0.70, 1.40, and 2.16 mm at G/d =1.19 kg/ms and p = 80 bar. The friction factor is seen to drop as the tube size was reduced. Yoon et al. [52] measured the pressure drop of a 7.73 mm diameter tube with variations in mass flux and pressure. The results were compared with literature correlation and showed good agreement with an average deviation of 3.7% and an absolute average deviation of 4.9%. They concluded that the Blasius equation is recommended for predicting pressure drops of sCO_2. Dang and Hihara [58] measured the pressure drop in a 1 mm and 2 mm tube and examined the effects of different mass fluxes and pressures. The influences are based on thermophysical properties. Son and Park [114] investigated the pressure drop of a 7.75mm tube with various CO_2 mass fluxes, pressures and temperatures. The experimental results were compared with suitable correlations. The Blasius correlation slightly underestimated the experiments (mean deviation 4.6%) whilst the Petrov and Popov [113] equation overestimated the experiments significantly (mean deviation 64%). Fang and Xu [115] used several data sources (Krasnoshchekov et al. [116], Liao and Zhao [59], Dang and Hihara [58], Huai et al. [117], Oh and Son [53] and Lv et al. [118]) to evaluate the available experimental results and existing correlations for an in-tube pressure drop of sCO_2 cooling. A new correlation (Eq.43-44) was developed through extensive computer tests based on the results of 297 experiments.

$$\xi_{iso,b} = 1.613 * \left[\ln\left(0.234 * \left(\frac{K}{d}\right)^{1.1007} - \frac{60.525}{Re_b^{1.1105}} + \frac{56.291}{Re_b^{1.0712}}\right)\right]^{-2} \quad (43)$$

$$\xi_{noniso} = \xi_{iso,b} * \left[\frac{\eta_w}{\eta_b}\right]^{-0.49\left(\frac{\rho_f}{\rho_{pc}}\right)^{1.31}} \quad (44)$$

Liu et al. [119] experimentally investigated the pressure drop with 4.6 and 10.7 mm tubes. The results of the 10.7 mm tube are displayed for four mass fluxes and three pressures. A comparison with the Blasius equation showed very good agreement.

3 Objectives of work

As already pointed out, the heat-removal process takes place in the near-critical region in the Brayton cycle. In the near-critical region, thermophysical properties change significantly in a small temperature range which makes the prediction of the heat transfer and pressure drop very challenging. A wide range of experimental and numerical investigation were analized in regard to the development of industrial heat exchangers which are showing promising results in terms of higher heat transfer rate with lower material input and internal volume. The experimental investigations are mainly on laboratory scale such as two-plates heat exchangers. However, the fundamental understanding of the heat transfer characteristics, based on the fluid properties, remains in the smallest scale which is represented by the single channel fluid flow. From the above discussion, it becomes clear that there are still discrepancies and lack of knowledge in cooling heat transfer of small size tube flow. It has been shown that heat transfer correlations which were developed for big diameter tubes are not able to predict the heat transfer of small diameter tubes accurately. The occurance of heat transfer deterioration in the vertical flow orientation was mainly investigated in the heating case. The only experimental work carried out so far in the cooling case was with a 6 mm tube which does not reflect on the compact heat exchangers of current state of the art.

The objective of this work is to investigate the heat transfer and pressure drop in small diameter tubes for the purpose of an accurate sizing of compact heat exchangers. In a sCO_2 Brayton cycle, the heat exchangers greatly influence the overall cycle efficiency. However, the heat transfer prediction in the cooling process close to the critical point is challenging due to the strong variations in thermophysical properties. The heat transfer and pressure drop performance data presented in this work will contribute to the design of new concepts of compact heat exchangers. The objective is to investigate the heat transfer performance and pressure drop with a high spatial resolution within a 2 mm tube, long enough to represent the complete cooling process of the Brayton cycle in one experiment. An experimental system was built up to investigate the local heat transfer characteristics of CO_2 cooled in a tube. In a second test section, the heat transfer and pressure drop performance are investigated in a 3

mm tube to examine the buoyancy and acceleration effects on the flow in both vertical and horizontal flow orientation.

In chapter 4, the experimental test facility “SCARLETT” and the two tube-in-tube test sections are presented. The used measurement devices including the uncertainties are complementing the chapter. In chapter 5, the data reduction is presented with the energy balance and the pressure drop evaluation which is valid for both testsections. The heat transfer calculations are presented in separate sub-chapters for the two test sections. In chapter 6.1, the influence on the heat transfer coefficient will be evaluated at a wide range of different CO_2 pressures, CO_2 mass fluxes, CO_2 inlet temperatures and cooling water temperatures. The significant effects of all parameters will be discussed in detail and a new heat transfer correlation for the heat transfer coefficient in a 2 mm tube will be developed. In chapter 6.2, the heat transfer in vertical flow orientation is evaluated with the 2 mm and 3 mm tubes. In the vertical flow, the heat transfer performance of the upwards and downwards orientation are compared and evaluated based on dimensionless criteria from the literature. In Chapter 6.3, the horizontal flow orientation was investigated in the 3 mm tube with variation in CO_2 mass fluxes and CO_2 inlet temperatures with the wall temperature measurements at the top and bottom of the tube to determine the development of temperature stratifications within the cooling process. In chapter 6.4, the pressure drop is evaluated with the 2 mm and 3 mm tube and compared to literature correlations.

4 Test facility

The SCARLETT test facility which provides sCO2 at defined boundary conditions for the experiments is introduced first. In chapter 4.2, the two tube test sections are presented including the introduction of the general construction approach and the applied measurement devices. The dimensioning of the tubes and the implementation of the temperature measurements in the tube wall are described in detail. The measurements devices and achieved accuracies are described in chapter 4.3.

4.1 SCARLETT test facility

The SCARLETT test loop provides sCO2 under defined boundary conditions. Figure 19 depicts the piping and instrumentation (P&I) diagram of the SCARLETT test loop, which is described in detail by Flaig et al. [120]. After evacuating the loop with a vacuum pump, the pressure vessels (1, 10) are filled with CO_2. During normal operation, liquid CO_2 flows from the storage vessel through an electrically heated evaporator (2) and is slightly superheated. After leaving a demister unit (3), where the remaining liquid CO_2 is separated from the flow, it enters a compressor (4), where it is compressed to a certain pressure and simultaneously heated by the compression.

Before entering a test section, there is conditioning (5) of the sCO_2, which means that a defined temperature can be adjusted via cooling or heating the sCO_2 mass flow rate. In the test section (6) different kinds of experiments can be performed. After leaving the test section, the sCO_2 is cooled down in a gas cooler (7) followed by the expansion in an expansion valve (8). Before it enters the storage vessel (1) the CO_2 can be cooled down again in a condenser (9). The sCO_2 mass flow rate in the SCARLETT test loop can be adjusted from about 30 to 110 g/s. Lower mass flow in the test section can be achieved by bypassing needle valves. It must be mentioned, that the achievable mass flow rate depends on the compressor performance map, which leads to less mass flow at higher pressures and vice versa. The sCO2 temperature at the inlet of the test section can be varied from about 0 to 140 °C and the pressure from about 75 to 110 bar.

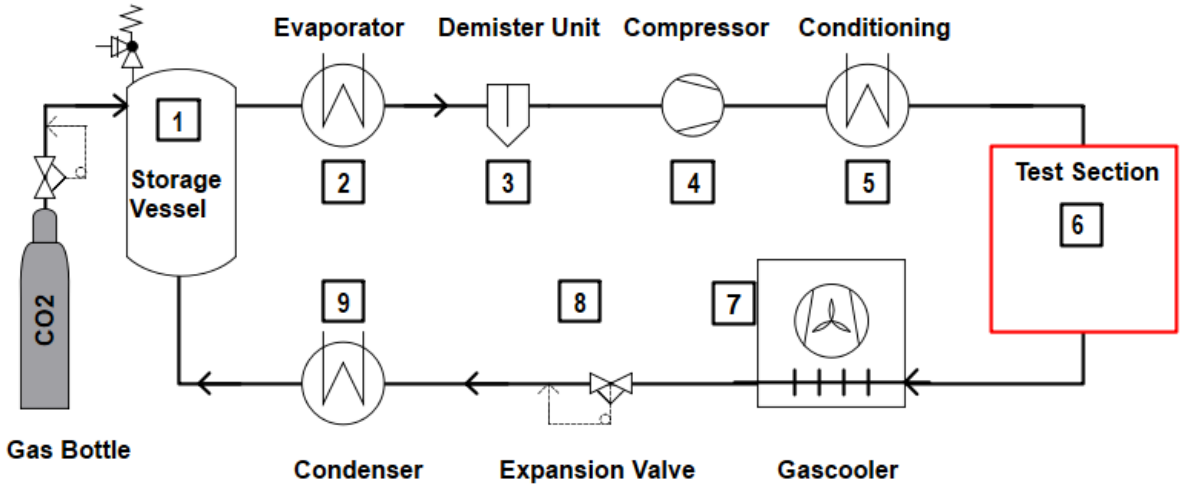

Figure 19: Flow diagramm of the SCARLETT test loop

4.2 Tube test sections

The test sections are constructed as a tube-in-tube heat exchanger. The main components of the test section are a circular straight tube and an outer structure to form the annulus. CO_2 flows in the straight tube and the cooling water flows in the annulus. The CO_2 mass flux is measured before entering the tube. The tube inflow is constructed with a T-junction with an implemented PT-100 temperature sensor. A hole was drilled in the tube wall between the tube inflow and the cooling part to measure the pressure with a minimum influence on the flow. A T-junction leads to a leak tide connection of the pressure sensors. The tube is completely symmetrical. The dimensions of the inflow area are the same as in the outflow area. An absolute pressure sensor is integrated on the high-pressure side. The two drilled holes are connected to a differential pressure sensor (Figure 20).

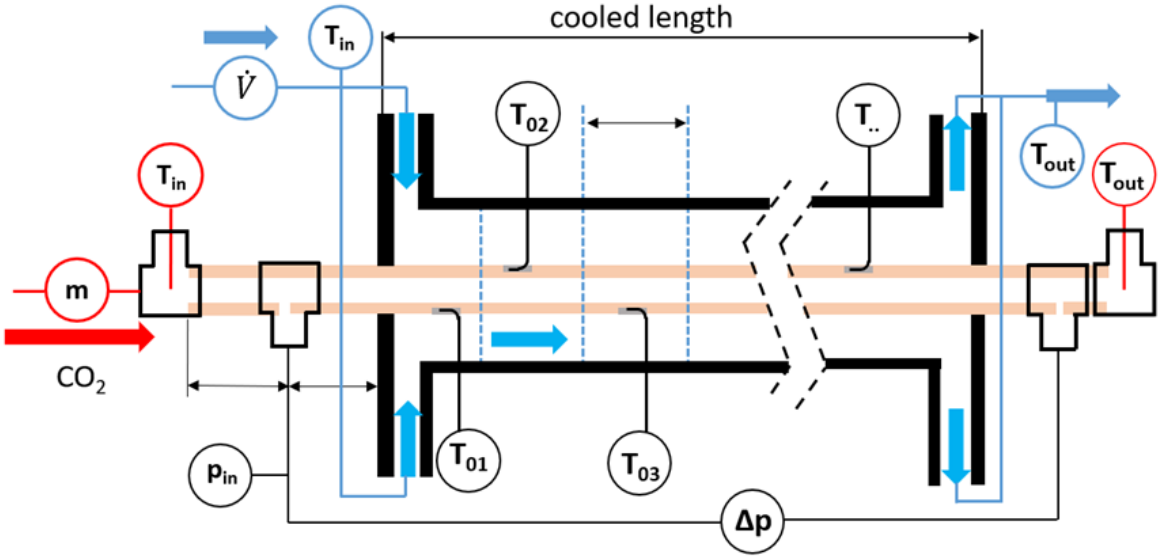

Figure 20: General construction of the test tubes

The cooling part of the tube is the actual test section. The outer structure of the test section leads the cooling water on two sides into the annulus to ensure a flow with uniform distribution. The thermocouples are led through the outer structure and soldered into the tube wall. The thermocouples are implemented into the tube with a constant distance in between. The volumetric flow $\dot{V}$, the inlet temperature T_{in} and the outlet temperature T_{out} are measured in the cooling flow.

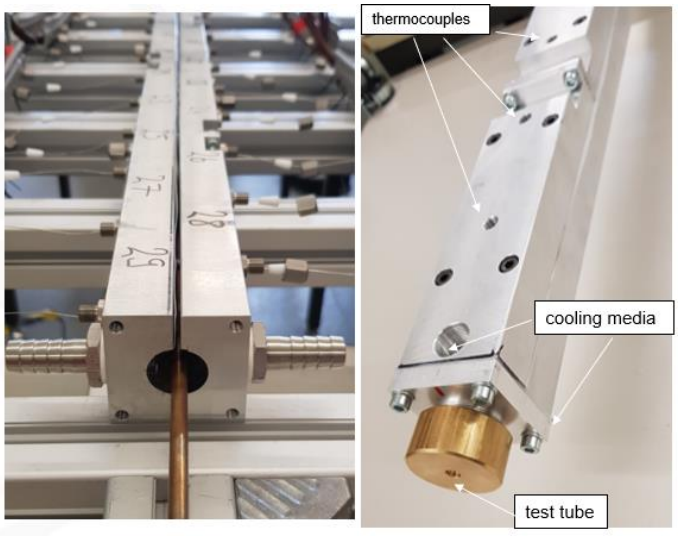

Figure 21: Outer structure of the test section

Figure 21 shows the test section during the build-up. On the left, the tube and outer structure are displayed without the flanges. Thermocouples are already soldered into the tube wall, the tube and the outer structure are in their end position. The following

steps in the construction are to screw both sides of the outer structure together to ensure a leak tide flow, bring the flanges into position and connect the water hose on both sides. On the right of Figure 21, the outer structure is displayed from a different angle with the flange. The connections for the cooling media flow and the thermocouples can be seen.

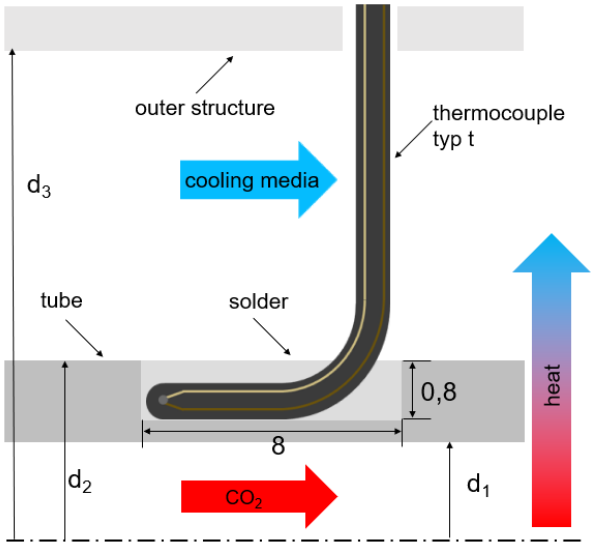

Figure 22: Implementation of thermocouples in the tube wall

The milled channels in the tube wall are displayed in Figure 22. The channels have the dimensions of 8mm length, 0,8mm depth and 0,8mm width. The thermocouples are bent and laid into the channel. The solder alloy used to connect the tube with the thermocouples was a 96 % tin and 4 % silver mixture with implemented colophony. This material has a low-temperature melting point (Solidus: 221 °C, Liquidus 238 °C), which does not exceed the temperature range of T-type thermocouples (-40 °C…+350 °C) and leads to a good thermal connection of the two components due to the high thermal conductivity.

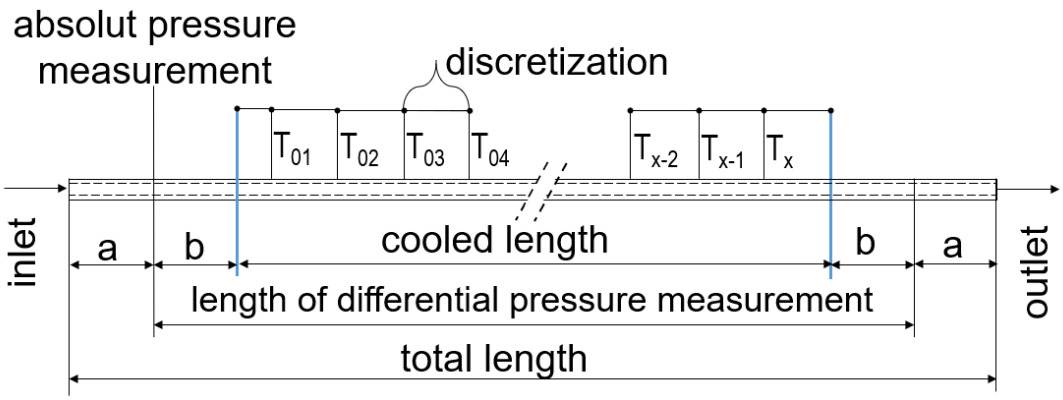

Figure 23: Dimensions of test tubes

The dimensions of the tubes are described in Figure 23 and Table 1 including the total length of the tube, the length of the differential pressure measurement and the cooling length. The cooled length contains the thermocouples with a constant discretization. The lengths a and b define the in- and outflow area.

Table 1: Dimensions of the test section

	2 mm	3 mm
cooled length [mm]	1200	500
Material	Copper	Stainless steal
number of tc's [-]	29	12
discretization [mm]	40	40
positioning of tc's	Alternating	One-sided
total length [mm]	1500	1000
diff. pressure [mm]	1386	700
a [mm]	57	150
b [mm]	93	100

In Figure 24, the 2 mm test section is displayed. The test section is mounted on a base frame and fully isolated. The coloured circles illustrate the measurement devices. The measurements of the CO_2 flow is shown in red and the cooling flow in blue. The test section is connected with the SCARLETT facility by the in- and outlet (red square). The bypass valves are used to adjust the mass flux during the experiments. A vacuum valve was implemented on both sides of the test section to evacuate the system. The in- and outlet of the cooling flow are built on the lower side of the frame. The temperature is measured before the flow is separated and the sensors enter the test section from both sides. The arrangement is identical on the outflow side.

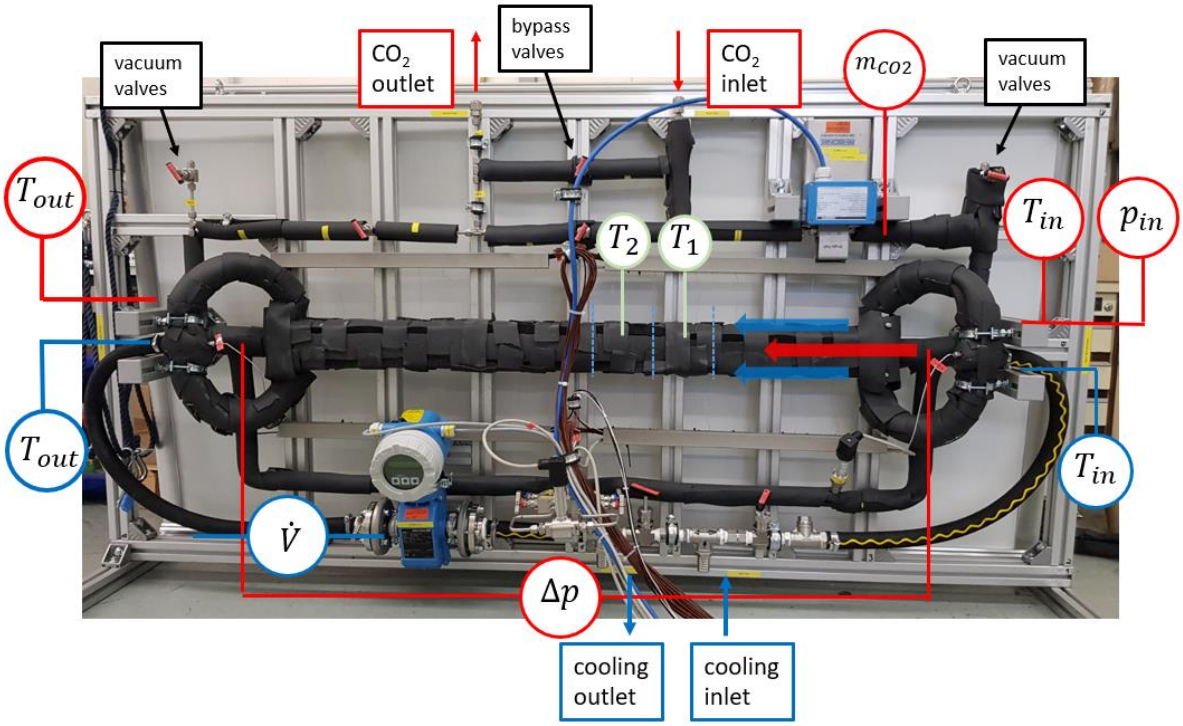

Figure 24: Test section 2mm tube

In Figure 25, the test section with the 3 mm tube is displayed during construction. The thermocouples are already soldered into the tube wall. In the next step, the outer tube structure is closed and the cooling media connections are mounted.

Figure 25: Test section 3mm tube during construction

4.3 Measurement devices and uncertainties

The measurement devices utilized for the experimental investigations are described in this chapter. The volumetric cooling flow was measured with electromagnetic flowmeters by manufacturer ENDRESS+HAUSER. The smaller size was used to ensure high accuracy at a lower flow of app 100 ml/s. The mass flow of CO_2 was measured with a Coriolis flow meter by manufacturer SCHWING. The Coriolis measuring principle can directly measure the mass flux which is very important due to rapidly changing density in the supercritical region. Simultaneously, the flow density is determined by the measurement device, however, the measured values were not utilized. The pressure was measured with piezoresistive sensors by manufacturer KELLER. The temperature measurements of the CO_2 flow were conducted with PT-100 resistance thermometers. The sensors were implemented into compression fittings by manufacturer ELECTRONIC SENSORS. The temperature measurements inside the tube wall were done with thermocouple sensors due to the small diameters of 0,5 and 1 mm. All temperature sensors were calibrated against a PT1000 Reference with an accuracy of ±0,02K. All measured quantities are summarized in Table 2.

Table 2: Experimental measurement devices

Meas. quantity	Symbol	Range	Unit	Accuracy
Volumetric flow	$\dot{V}$	0-2.5	dm³/s	±1%
Mass flow	$\dot{m}$	0-50	g/s	±0.3%
Pressure	p	0-100	bar	±0.15
Diff. pressure	Δp	0-1000	mbar	±1.5
Thermocouples	T	5-60	°C	±0.1
RTD	T_{in}/T_{out}	0-100	°C	±0.1

The temperature calibration was conducted with a copper cylinder immersed in a bath thermostat. The cylinder has drilled holes in the centre for the reference temperature measurement and 32 holes in the circumference for the thermocouples. The cylinder was immersed completely in the bath with a flow restriction reaching over the water surface. During the calibration process, the water bath was shielded from the surrounding air by insulation foam.

For the calibration process, the thermostat was set to a fixed temperature. The water bath and the copper block took some time the reach the equilibrium temperature. The measurement interval was 15 minutes. The thermocouples were calibrated within a range of 5 - 65°C with 5 K differences between the temperature points. The derivation between the reference temperature and the thermocouples was regressed with a linear function and implemented into the data processing.

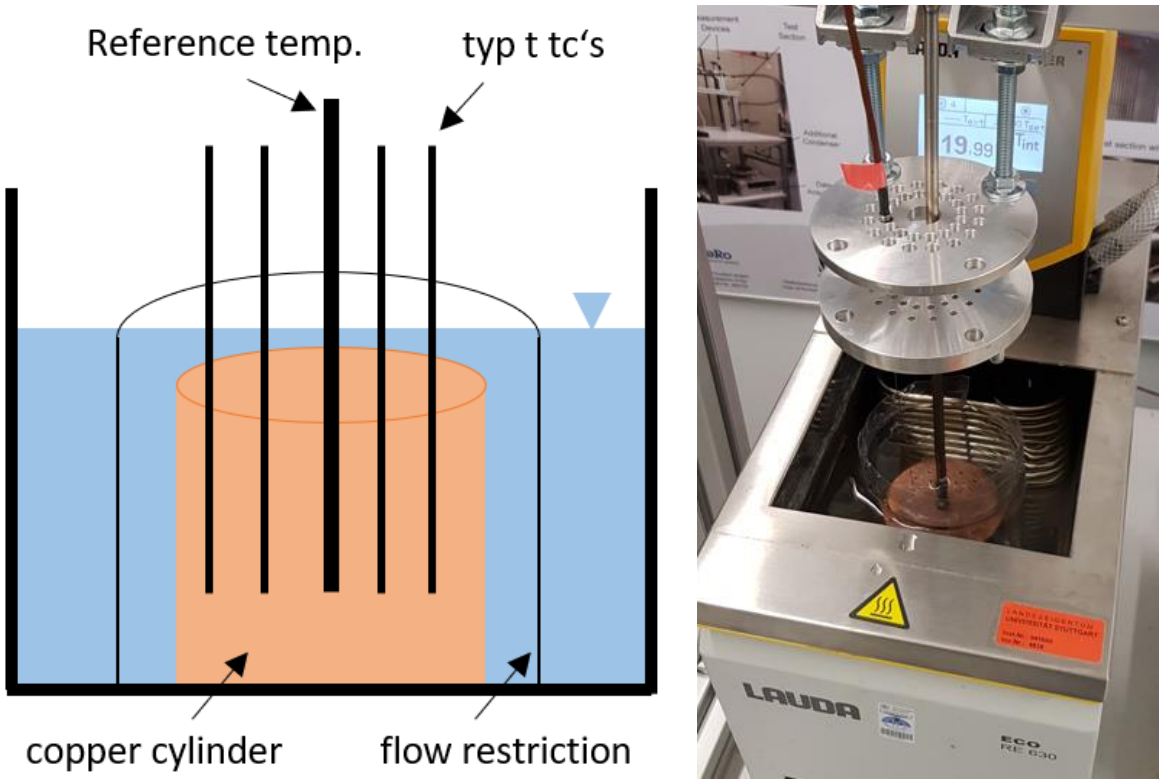

Figure 26: Temperature calibration schematic diagram and the Lauda bath thermostat

5 Data reduction

In this chapter, the calculation methods are presented for both test sections. The experimental tubes vary significantly in diameter and cooled length which leads to separate calculation approaches. The explanations in chapter 5.1 and 5.2 for the transferred heat in both flows and the frictional pressure drop are valid for both tubes. In chapter 5.3, the calculation method of the heat transfer for the 2 mm and 3 mm tubes are presented separately.

5.1 Energy balance

The transferred heat in the cooling side is calculated by the use of the measurement values of the volumetric flow $\dot{V}$ and the temperature difference between the inlet and outlet $T_{c,out} - T_{c,in}$. The density ρ was derived from the inlet temperature $T_{c,in}$ and the isobaric heat capacity c_p from the average water temperature $(T_{c,out} - T_{c,in})/2$:

$$Q_{cool} = \dot{V} \rho \, c_p (T_{c,out} - T_{c,in}) \tag{45}$$

The transferred heat measured in the CO_2 flow is based on the measured mass flow m_{CO2}. The temperature measurements T_{in}/T_{out} contribute directly to the enthalpy. The inlet pressure is directly measured, while the outlet pressure is determined with the differential pressure.

$$Q_{CO2} = m \, (h(p_{in}, T_{in}) - h(p_{out}, T_{out})) \tag{46}$$

5.2 Pressure drop and friction factor

The pressure drop evaluation is based on the Bernoulli equation. In Eq.47, the equations are described by the pressure energy, potential energy and kinetic energy.

$$p_{in} + \rho g h + \frac{\rho_{in}}{2} u_{in}^2 = p_{out} + \rho g h + \frac{\rho_{out}}{2} u_{out}^2 + p_{fric} \qquad (47)$$

In the horizontal flow orientation, the difference in the potential energy can be neglected. The measured pressure drop is the difference between the inlet and outlet (Eq.48):

$$\Delta p_{meas} = p_{in} - p_{out} \qquad (48)$$

Due to the reduction of the density within the cooling process, the change in kinetic energy must be considered. The frictional pressure drop is calculated as follows in Eq. 49:

$$p_{fric} = \Delta p_{meas} - \frac{1}{2} * \left(\frac{1}{\rho_{out}} - \frac{1}{\rho_{in}} \right) * G^2 \qquad (49)$$

by use of the mass flux density G and the respective densities at in- and outlet. In both test sections, the frictional pressure drop consists of three parts. In the perspective of the flow direction, an isothermal length is considered before and after the cooling section in Eq.50:

$$p_{fric} = \Delta p_{inflow} + \Delta p_{cool} + \Delta p_{outflow} \qquad (50)$$

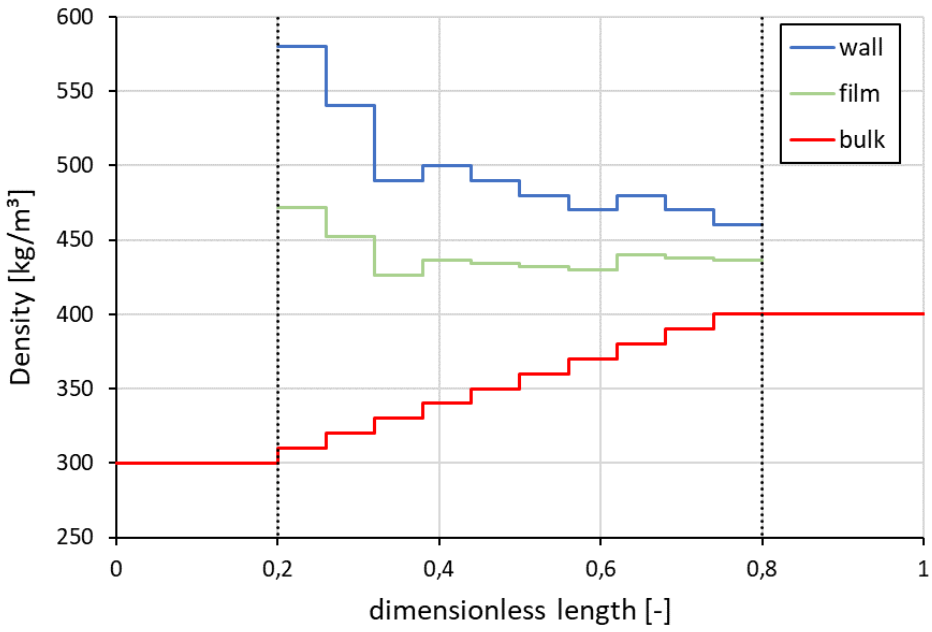

Figure 27: Schematic progress of the bulk, film and wall density along the test section

In Figure 27, the schematic progress of the density along the tube is shown. The inflow at 0 to 0.2 and the outflow at 0.8 to 1 is isothermal, thus, just the bulk density is displayed. The densities of the wall, film and bulk are displayed in the cooled length between 0.2 to 0.8. Therefore, it's possible to evaluate the pressure drop based on the different density values.

5.3 Heat transfer calculations

5.3.1 Integrational method in 2 mm tube

The heat output at each discretization step ($\dot{Q}_x$) is defined by the iterated heat transfer coefficient on the outer tube surface ($\mathrm{htc_{cool}}$), the outer tube area ($\mathrm{A_{t,o}}$) and the temperature difference between wall and cooling water temperature $\left(\mathrm{T_{t,o}} - \mathrm{T_{cool}}\right)$ (Eq.51):

$$\dot{\mathrm{Q}}_x = \mathrm{htc_{cool}} * \mathrm{A_{t,o}} * \left(\mathrm{T_{t,o}} - \mathrm{T_{cool}}\right) \tag{51}$$

The heat transfer resistance of the copper tube leads to a small difference between the inner ($\mathrm{T_{t,i}}$) and outer ($\mathrm{T_{t,o}}$) temperature of the tube wall by considering the thermal conductivity λ_{Cu} = 340W/mK, the inner and outer diameter of the test tube ($\mathrm{d_o}$, $\mathrm{d_i}$), the length of the pipe section L. The inner tube temperature ($\mathrm{T_{t,i}}$) is equal to the wall temperature of CO_2 ($\mathrm{T_{CO2,w}}$) (Eq.52):

$$\dot{\mathrm{Q}}_x = \frac{2\,\pi\,\mathrm{L}\,\lambda_{\mathrm{Cu}}}{\ln\left(\frac{\mathrm{d_o}}{\mathrm{d_i}}\right)}\left(\mathrm{T_{t,o,x}} - \mathrm{T_{t,i}}\right) \tag{52}$$

The heat transfer coefficient of CO_2 at every discretization step is calculated by the heat $\dot{Q}_x$, the inner tube area $\mathrm{A_i}$ and the temperature difference between bulk and wall temperature (Eq.53):

$$\mathrm{htc_{CO2,x}} = \frac{\dot{\mathrm{Q}}_x}{\mathrm{A_i} * \left(\mathrm{T_{CO2,b}} - \mathrm{T_{CO2,w}}\right)} \tag{53}$$

Both, CO_2 and cooling water temperatures are measured at the in- and outlet. Within the tube, the process temperatures are calculated by the heat flux of the previous discretization step and the respective mass flux to determine the enthalpy of the flow (Eq.54). The heat exchanger is operated in the co-current flow of sCO_2 and the cooling water.

$$\mathrm{h_{CO2/cool}(x+1)} = \mathrm{h_{CO2/cool}(x)} \pm \frac{\dot{\mathrm{Q}}(\mathrm{x})}{\dot{\mathrm{m}}_{\mathrm{CO2/cool}}} \tag{54}$$

This procedure leads to 29 sets of the process parameters along the test section. Each thermocouple measurement is paired with cooling water and a CO_2 temperature. The calculation leads to a progress of the CO_2 bulk fluid temperature, which is the result of the earlier described assumptions, all parameters measured and most significantly, the properties of CO_2. For each experiment, htc_{cool} was assumed to be constant along the test section and is the result of solving Eq.55. The iteration fits the measured heat loss $\dot{Q}_{CO2}$ with the heat of the cooling side $\dot{Q}_{cool,calc}$by the integration of the Eq.51-53 along the test section:

$$\dot{Q}_{cool,cal} = htc_{cool} * \pi * d * \int_0^l \left(T_{t,o} - T_{cool}\right) dx = \dot{Q}_{CO2} \tag{55}$$

In Figure 28, an example of the calculated temperature within the tube is displayed. The x-axis is the length of the tube from 0 to 1.2m. The y-axis shows the temperature of the fluids. In red and blue squares, the measured in- and outlet temperatures are displayed for CO_2 and water. Along the tube, the measured values of the tube wall are displayed in grey squares. The temperature difference of the cooling media is relatively small, which leads to an almost linear increase in the cooling media temperature. From the inflow, the CO_2 bulk decreases fast due to the high heat flux based on the high-temperature difference.

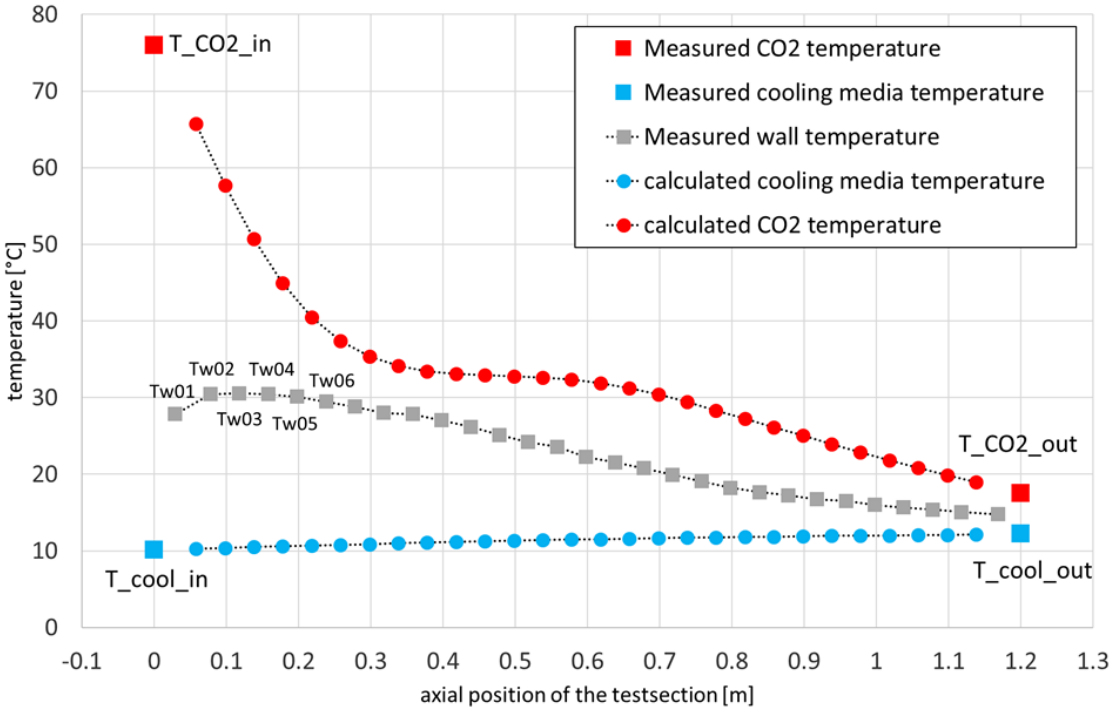

Figure 28: Calculation example

At reaching the pseudocritical temperature, the pseudo phase change occurs which leads to an almost constant temperature. After the pseudocritical point, the temperature decreases with a lower gradient based on the smaller temperature difference of the fluids.

Error propagation

Additional to the measurement errors, the error of the manual soldering process must be considered. For example, the manufacturing inaccuracies of the milled channels, the placing in the channel and the properties of the solder contribute to the assumed accuracy of the outer wall temperature of the cooper tube ($T_{t,o}$) of ±0.2 K. htc_{cool} was assumed to be constant along the test section with an accuracy of ±20 %. This value is a coarse estimation up to now.

Due to the explained assumptions, the accuracy of the CO_2 temperature along the test section was assumed as ±0.5 K. From the manufacturer certificate, the error of the inner and outer tube diameter was 0.05 mm. The heat conductivity of the cooper tube λ_{Cu} was assumed as 340 W/mK ±40 W/mK.

5.3.2 Averaging method in 3 mm tube

The temperature difference in the cooling media flow between the in- and outlet is too small to apply a caloric determination. Therefore, the heat flux is calculated based on the CO_2 heat flux considering the tube dimensions (Eq.56):

$$\dot{q}_{CO2} = \frac{\dot{Q}_{CO2}}{\pi d L} \tag{56}$$

The CO_2 bulk temperature $T_{CO2,b}$for each experiment is the average of in- and outlet temperature (Eq.57):

$$T_{CO2,b} = \frac{T_{CO2,in} + T_{CO2,out}}{2} \tag{57}$$

The twelve tube temperature measurements are averaged in Eq.58:

$$T_t = \frac{\sum_{i=1}^{12} T_{t,i}}{12} \tag{58}$$

The heat conduction of the tube wall leads to a difference between the measured tube wall temperature $T_{R,i}$ and the CO_2 wall temperature $T_{CO2,w}$. For this reason, the tube wall temperature measurement is assumed to be centred between the inner and outer surface (Eq.59):

$$T_{CO2,w} = T_t + \dot{q}_{CO2} \cdot \frac{\ln\left(\frac{4\ mm}{3\ mm}\right)}{2\pi L \lambda} \tag{59}$$

The heat transfer coefficient is defined as the ratio of heat flux and the temperature difference between CO_2 bulk and wall (Eq.60):

$$htc_{CO2} = \frac{\dot{q}_{CO2}}{\Delta T} \tag{60}$$

Because that in the supercritical region c_p und htc can change strongly, it is important to evaluate different definitions of the temperature difference ΔT. One option, as considered by Yoon et al. [52], Son et al. [114] and Liu et al. [119], is to calculate the difference of both averaged values $T_{CO2,b}$ and $T_{CO2,w}$ (Eq.61):

$$\Delta T_{average} = T_{CO2,b} - T_{CO2,w} \tag{61}$$

A second approach is to calculate the logarithmic mean temperature difference (LMTD) (Eq.62):

$$\Delta T_{LMTD} = \frac{\left(T_{in} - T_{CO2,w,1}\right) - \left(T_{out} - T_{CO2,w,12}\right)}{\ln\left(\frac{T_{in} - T_{CO2,w,1}}{T_{out} - T_{CO2,w,12}}\right)} \tag{62}$$

with the CO_2-wall temperature at the first and the last measurement $T_{CO2,w,1}$ / $T_{CO2,w,12}$ as applied by Liao [59] and Dang [58].

Error propagation

The error bars for the 3 mm tube are calculated based on the statistical error propagation according to the Gaussian error propagation (Eq.63). The standard deviation σ_k is based on partial differentials of each independent variable (x, y, …). The independence of the variables and the linear characteristic of the gradient is an assumption that delivers a good estimation of the standard deviation:

$$\sigma_k = \sqrt{\left(\frac{\partial k}{\partial x}\Delta x\right)^2 + \left(\frac{\partial k}{\partial y}\Delta y\right)^2 + \cdots} \tag{63}$$

For the heat flux of CO_2, the partial differentials of the measured quantities are shown in Eq.64-68. In Refprop, the differentials of the Enthalpy are available.

$$\frac{\partial\, q_{CO2}}{\partial\, m} = \frac{h_{in} - h_{out}}{\pi d L} \tag{64}$$

$$\frac{\partial\, q_{CO2}}{\partial\, p_{in}} = \frac{m\left(\frac{\partial h_{in}}{\partial p} - \frac{\partial h_{out}}{\partial p}\right)}{\pi d L} \tag{65}$$

$$\frac{\partial\, q_{CO2}}{\partial\, \Delta p} = \frac{m\left(\frac{\partial h}{\partial p}(p_{out}, T_{out})\right)}{\pi d L} \tag{66}$$

$$\frac{\partial\, q_{CO2}}{\partial\, T_{in}} = \frac{m\left(\frac{\partial h}{\partial T}(p_{in}, T_{in})\right)}{\pi d L} \tag{67}$$

$$\frac{\partial\, q_{CO2}}{\partial\, T_{out}} = \frac{m\left(\frac{\partial h}{\partial T}(p_{out}, T_{out})\right)}{\pi d L} \tag{68}$$

The standard deviation of the experimental result is calculated based on Eq.69:

$$\Delta\, q_{CO2} = \sqrt{\left(\frac{\partial\, q_{CO2}}{\partial\, m}\right)^2 \Delta m^2 + \cdots} \tag{69}$$

The standard deviation of the heat transfer coefficient is based on the partial differentials of the heat flux, the bulk and wall temperature (Eq.70-72):

$$\frac{\partial\, htc_{CO2}}{\partial\, \dot{q}_{CO2}} = \frac{1}{T_b - T_w} \tag{70}$$

$$\frac{\partial\, htc_{CO2}}{\partial\, T_b} = \frac{\dot{q}_{CO2}}{(T_b - T_w)^2} \tag{71}$$

$$\frac{\partial\, htc_{CO2}}{\partial\, T_w} = \frac{\dot{q}_{CO2}}{(T_b - T_w)^2} \tag{72}$$

The standard deviation of the heat flux $\Delta\, q_{CO2}$ (Eq.73) is based on the calculation of Eq.69 and ΔT is based on the measurement accuracy:

$$\Delta\, htc_{CO2} = \sqrt{\left(\frac{\partial\, htc_{CO2}}{\partial\, \dot{q}_{CO2}}\right)^2 \Delta {q_{CO2}}^2 + \left(\frac{\partial\, htc_{CO2}}{\partial\, T_b}\right)^2 \Delta T^2 + \left(\frac{\partial\, htc_{CO2}}{\partial\, T_w}\right)^2 \Delta T^2} \tag{73}$$

6 Results

This chapter is built up according to the shown research gaps in chapters 2.4.2 to 2.4.5. In chapter 6.1, the influence on the heat transfer coefficient will be evaluated at a wide range of different CO_2 pressures, CO_2 mass fluxes, CO_2 inlet temperatures and cooling water temperatures. The significant effects of all parameters will be discussed in detail and a new heat transfer correlation for the heat transfer coefficient in a 2 mm tube is presented. In chapter 6.2, the heat transfer in vertical flow orientation is evaluated with the 2 mm and 3 mm tubes. In the vertical flow, the heat transfer performance of the upwards and downwards orientation are compared and evaluated based on the Jackson criterion. In Chapter 6.3, the horizontal flow orientation was investigated in the 3 mm tube with variation in CO_2 mass fluxes and CO_2 inlet temperatures with the wall temperature measurements at the top and bottom of the tube to determine the development of temperature stratifications within the cooling process. In chapter 6.4, the pressure drop is evaluated with the 2 mm and 3 mm tubes and compared to literature correlations.

6.1 Forced convection cooling heat transfer in 2 mm tube

In this experimental study, the heat transfer was derived for different boundary conditions in the 2 mm tube. The experiments were conducted with a constant cooling mass flux of $\dot{V}_{cool} = 100\ \mathrm{ml/s}$ with a wide range of CO_2 temperatures between 80 and 10 °C. Three CO_2 pressure and four CO_2 mass fluxes were tested (Table 3). The combinations of all these parameters leads to a total number of cooling experiments in horizontal flow orientation of 160.

Table 3: Experimental inlet conditions of horizontal cooling in 2 mm tube

p_{CO2} (bar)	G_{CO2} (kg/m²s)	T_{cool} (°C)	
77	400 (G1)	10	15
81	600 (G2)	20	22.5
85	850 (G3)	25	27.5
	1300 (G4)	30	32.5
		35	40

With the chosen volumetric flow of cooling water $\dot{V}_{cool} = 100\ ml/s$, the difference between $T_{cool,in}$ and $T_{cool,out}$ resulted in an average of 1.13 °C. This marginal difference reduces the potential differences between the measured and the calculated outlet temperature of the cooling media. Additional, this approach leads to the fact that the integrational term of Eq.56, $\int_0^l (T_{t,o} - T_{cool})$, has a small dependency from htc_{cool}. Thus, the adjustment of htc_{cool} leads to an approximately proportional adjustment of $\dot{Q}_{cool,calc}$.

The Reynolds numbers range based on the bulk fluid properties of the experiments are displayed in Figure 29. For the highest mass flux ($1300\ kg/m^2s$) and high temperatures the Reynolds numbers are at approximately $120 \cdot 10^3$. With the reduction of temperature, the Reynolds number drops by a factor of 3 at constant mass flux. At the lowest mass flux ($400\ kg/m^2s$), the Reynolds number is within a range of 10 to $39 \cdot 10^3$ in the complete temperature range which is still far in the turbulent flow region. In between 30 and 40 °C, the pressure plays a major role based on the shifted fluid properties. The Reynolds number can be higher with lower mass flux and lower pressure which can be seen at the overlapping of 81bar/1300kg/m²s with 77bar/850kg/m²s.

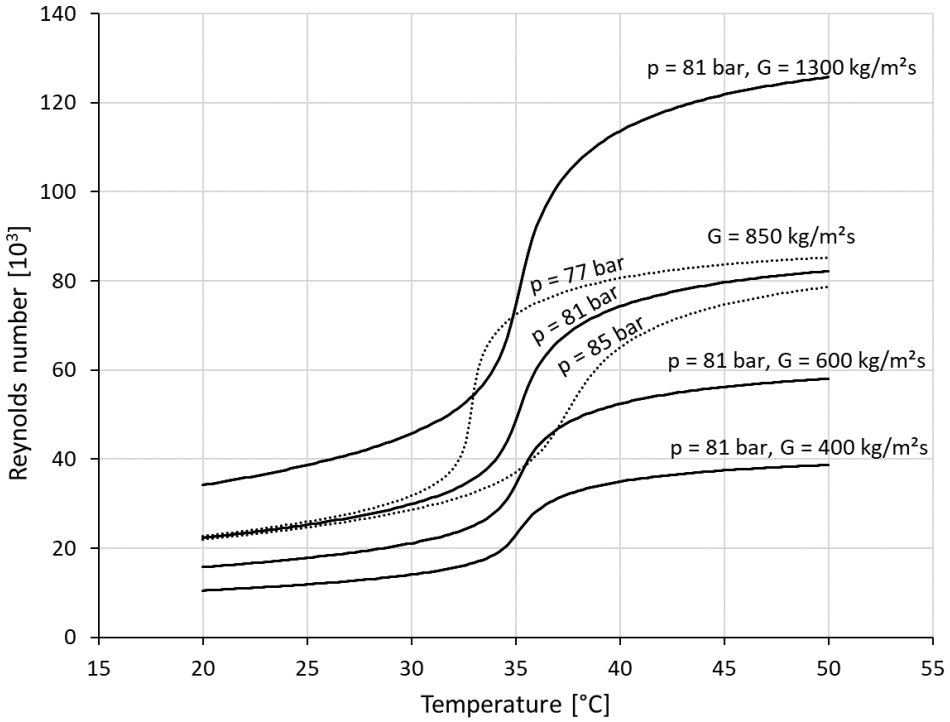

Figure 29: Reynolds number as a function of the bulk fluid temperature for the four experimental mass flux and the three different pressures at 850kg/m²s

The measured heat values in both, CO_2 and cooling media are compared in Figure 30. It can be seen, that most of the experiments are within a deviation of ±25%. At low cooling temperatures (10-15°C), the measured heat input of cooling flows is higher caused by the heat input by the ambient air. At higher cooling temperatures (>25°C), this trend is inverted. An exemplary error bar is displayed. The high error in Q_{cool} is caused by the small temperature differences between the in- and outlet of the cooling flow.

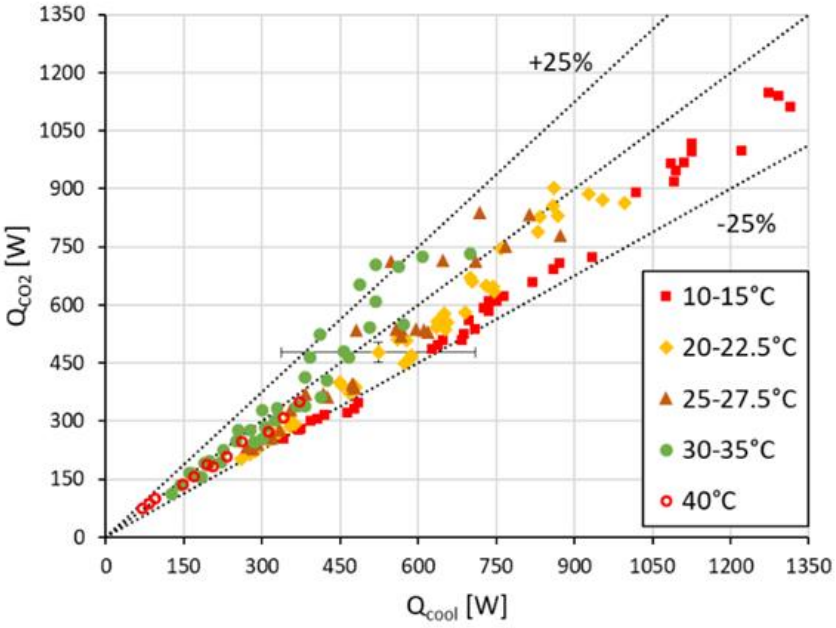

Figure 30: Energy balance of CO2 and cooling flow including an exemplary error bar

The repeatability of the experimental results is displayed exemplary in Figure 31. The set value of the experiments is 1300 kg/m²s, 81bar, 69 °C for the CO_2 inlet conditions and 100 ml/s, 25 °C as cooling flow inlet conditions. The experimental values of the CO_2 parameters are displayed in the diagram. The deviation between the two values is 52.6 kg/m²s/4.0 % for the mass fluxes, 0,15 bar/-0.2 % at pressure and -0.1 %/ 0.3 °C at the inlet temperature. Both results are in very good agreement. The red line is slightly higher due to the 4 % higher mass flux. Thus, overall good repeatability is given in the experiments. As the experiment is under cooling conditions, the entrance of the test section is on the right of the diagram. The 29 thermocouples in the tube deliver the displayed data point with a steady reduction of the bulk temperature.

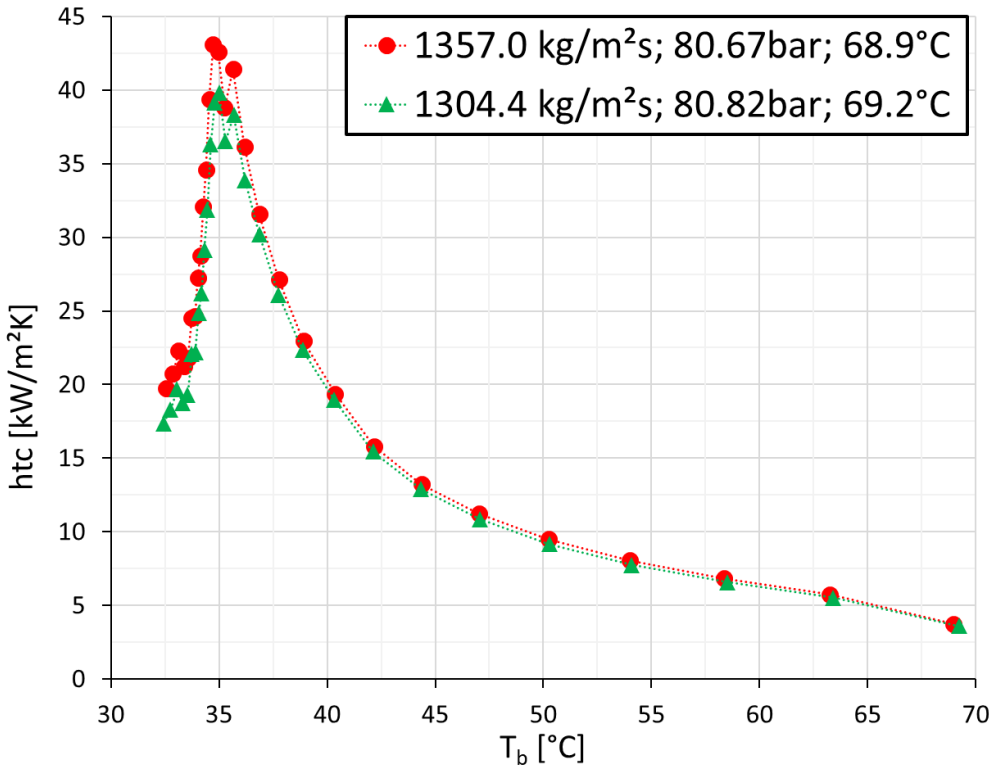

Figure 31: Exemplary repeatability of experiments at CO_2 conditions of 1300 kg/m²s, 80 bar and 69 °C

The error bars of the experimental results are displayed exemplary in Figure 32. At the entrance of the test section, the CO_2 temperature is high which leads to a general high-temperature difference between CO_2 bulk and CO_2 wall. In this region, the measurement deviation of the temperatures is relatively small compared to the measured difference. With further cooling, the CO_2 bulk temperature is lowered fast, lowering the temperature difference and thus increasing the error bar. The high heat transfer at the vicinity of the pseudocritical temperature further decreases the difference between CO_2 bulk and wall which leads to the highest error bars. With further reduction of the CO_2 bulk temperature, the heat transfer coefficient decreases which leads in total to smaller error bars.

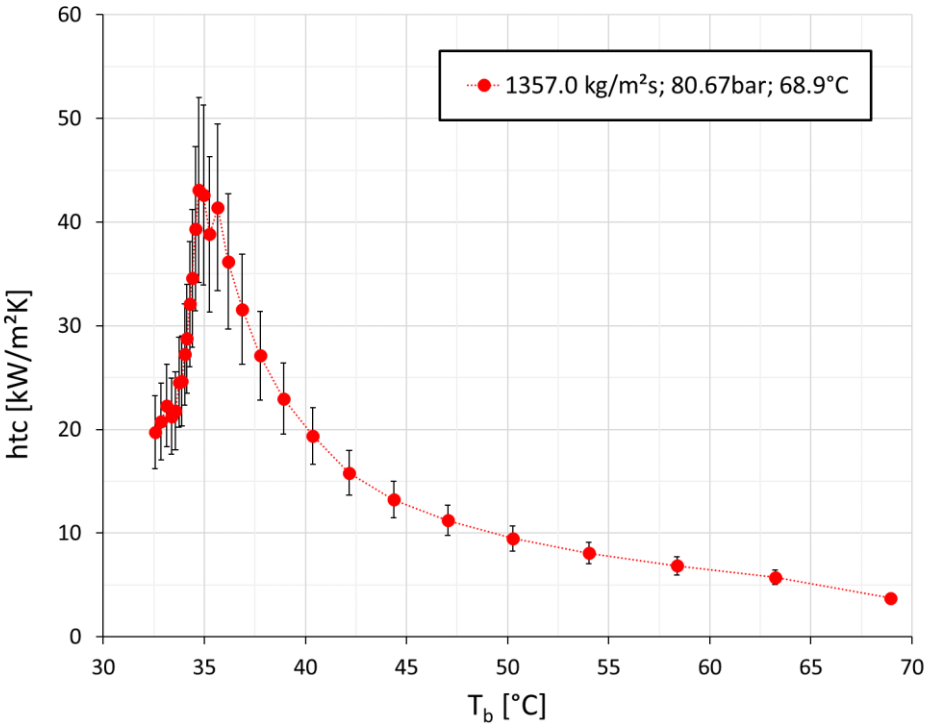

Figure 32: Error bars of experiment at CO_2 conditions of 1300 kg/m²s, 80 bar and 69 °C

6.1.1 Parametric study

In this parametric study, the influence of each experimental parameter on the heat transfer coefficient is analysed by showing variations of the respective parameter with all other parameters at constant values. Figure 33 (top) presents the effect of the mass fluxes at 415, 830 and 1370 kg/m²s for p_{CO2} = 85 bar and T_{cool} = 10 °C. The heat transfer coefficient is shown as a function of the bulk fluid temperature. The heat transfer coefficient increases as the mass flow increases due to an increase in turbulent diffusion. As shown by Dang and Hihara [58], the maximum heat transfer coefficient occurred at bulk temperatures slightly higher than the pseudocritical temperature.

In Figure 33 (bottom) the heat flux q_{CO2} is shown as a function of the bulk temperature. The heat flux is in total higher for increased mass fluxes. This is caused by the increased heat transfer coefficient, whereas T_{cool} and htc_{cool} were constant. The heat flux underwent a sharp decrease by crossing the pseudocritical temperature. At the first position of temperature measurement q_{CO2} is lower than the second position due to the lower temperature caused by heat conduction towards the flanges.

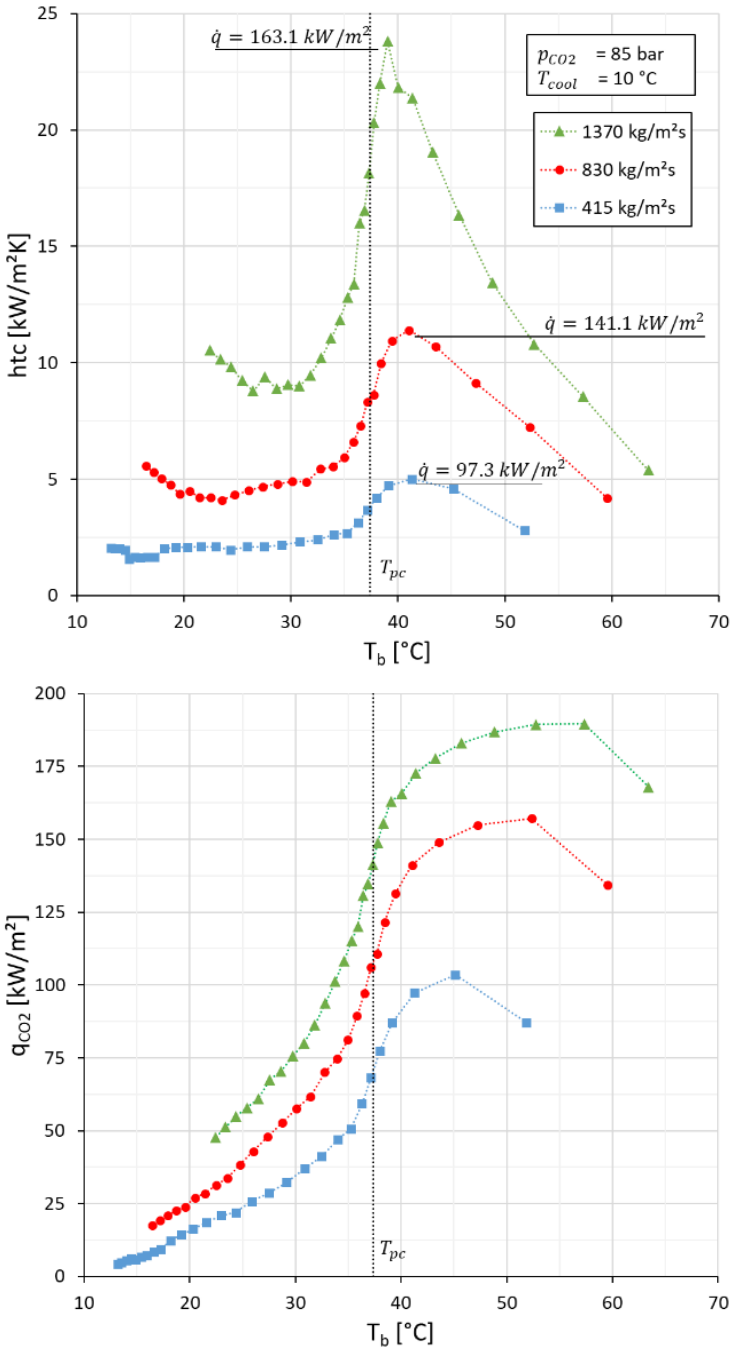

Figure 33: Effect of mass flux; heat transfer coefficient and heat flux as a function of the bulk fluid temperature

Figure 34 presents the htc of CO_2 for three different pressures ranging from 77 bar to 85 bar at G = 860 kg/m²s and T_{cool} = 10°C. For each pressure, the htc shows the same tendency in the gas like region. The htc increases continuously by approaching the pseudocritical temperature. In this stage, higher pressure has a higher heat transfer coefficient due to the higher thermal conductivity. For different pressures, the gradient of the htc continues to different peak values. The values are reduced with increased pressure and htc values of 21, 15 and 12 kW/m²s are reached. This behaviour is

related to the evolution of specific heat with temperature and pressure. In the liquid-like region of the cooling process, the htc decreases for all pressures to the same level. In this stage, higher pressure has a lower heat transfer coefficient due to the lower specific heat. In this temperature range, however, the measurement uncertainty increases as the CO_2 temperature approaches the cooling media temperature.

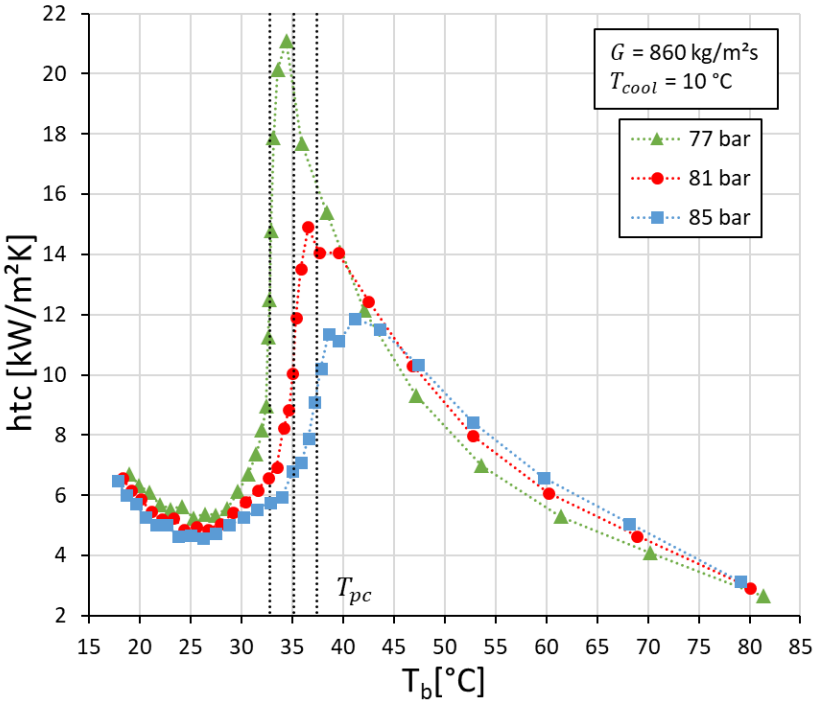

Figure 34: Effect of pressure; heat transfer coefficient as a function of the bulk fluid temperature

Figure 35 (top) shows the htc at two different cooling media temperatures at p_{CO2} = 77 bar, G = 860 kg/m²s. T_{cool} = 20 °C leads to slightly lower htc in the early stage of the cooling process whereas the peak value is significantly higher. In the late stage of the cooling process, the tendency is reversed: higher cooling media temperature leads to a higher htc. In Figure 35 (bottom) the wall temperature is displayed as a function of the bulk temperature. T_{cool} = 10 °C leads to a lower wall temperature, thus, the wall temperature is subcritical from the early stage of the cooling process. As the bulk temperature approaches the pseudocritical temperature, the wall temperature is already far below the pseudocritical temperature, thus, the wall properties left the beneficial temperature range, which is close to the pseudocritical critical temperature. At T_{cool} = 20 °C, the wall temperature reaches the pseudocritical temperature at T_b = 48 °C. As the bulk temperature reaches the pseudocritical temperature, the wall

temperature is close to the pseudocritical temperature. Thus, both bulk and wall temperatures are in the temperature range of beneficial properties.

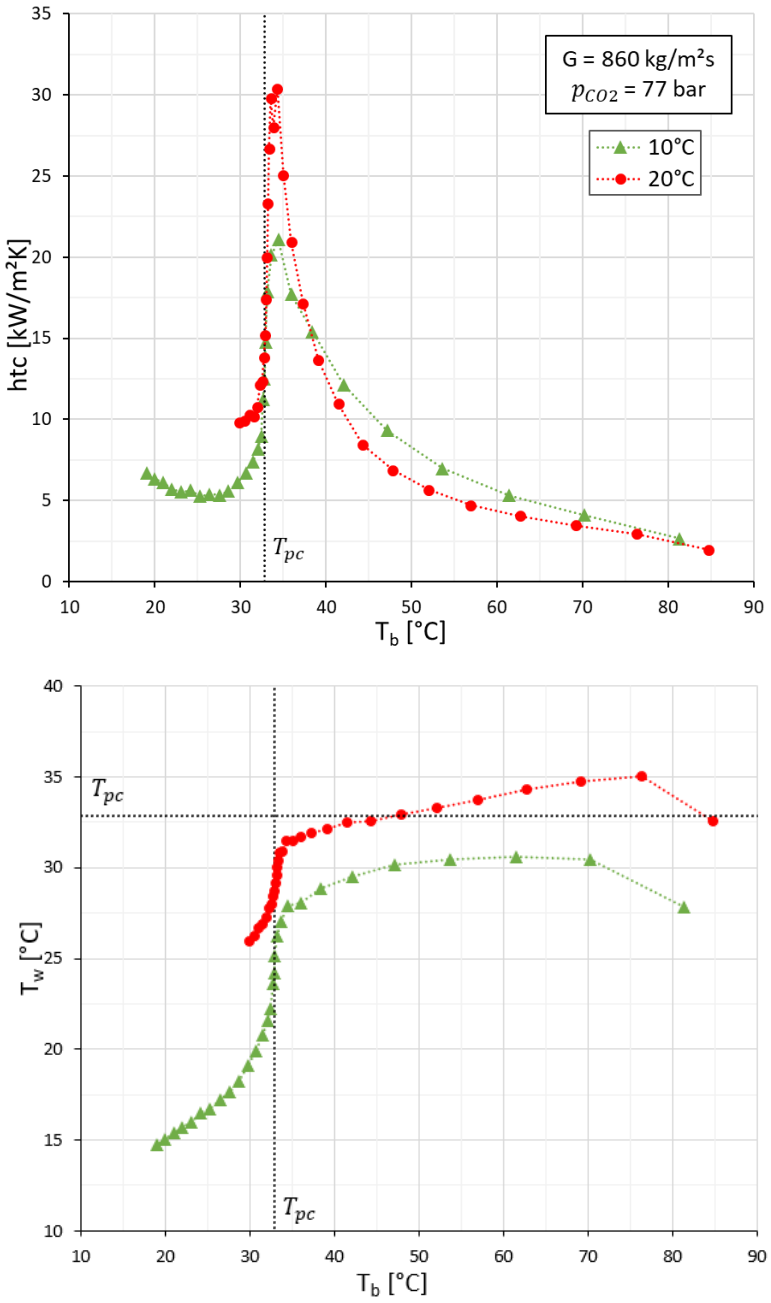

Figure 35: Effect of cooling temperature; heat transfer coefficient and wall temperature as a function of the bulk fluid temperature

To verify the experimental setup, it is important to prove the reproducibility of the heat transfer calculation. In Figure 36, three different experiments are displayed in which only $\mathrm{T_{CO2,in}}$ is varied, while $\mathrm{T_{cool}}$, $\mathrm{p_{CO2}}$ and G are kept constant. The heat transfer coefficient (top) and the wall temperature (bottom) are displayed as a function of the bulk temperature. The CO_2 is cooled in the tube, which means, that $T_{CO2,in}$ is on the right side and the progress of cooling inside the tube should be read from right to left in both diagrams. The bulk temperature ranges of the experiment are overlapping. The comparison shows, that htc and T_w are in good agreement confirming the very good repeatability of the experiments. Additionally, clear evidence of inlet and outlet effects can be seen. The first three discretization steps can be denoted as inflow effects and the last four as outflow effects. Both effects are not evaluated further. It cannot be stated if these effects are caused by the thermal behaviour of the CO_2 flow, heat conduction in the tube wall or the local heat transfer on the cooling side. For the discretization points, 4 to 25, heat transfer coefficient and wall temperature are in good agreement. The inlet and outlet effects are marked and excluded from the connecting dotted line. Regarding the development of a forced convection heat transfer correlation, this effect must be filtered out.

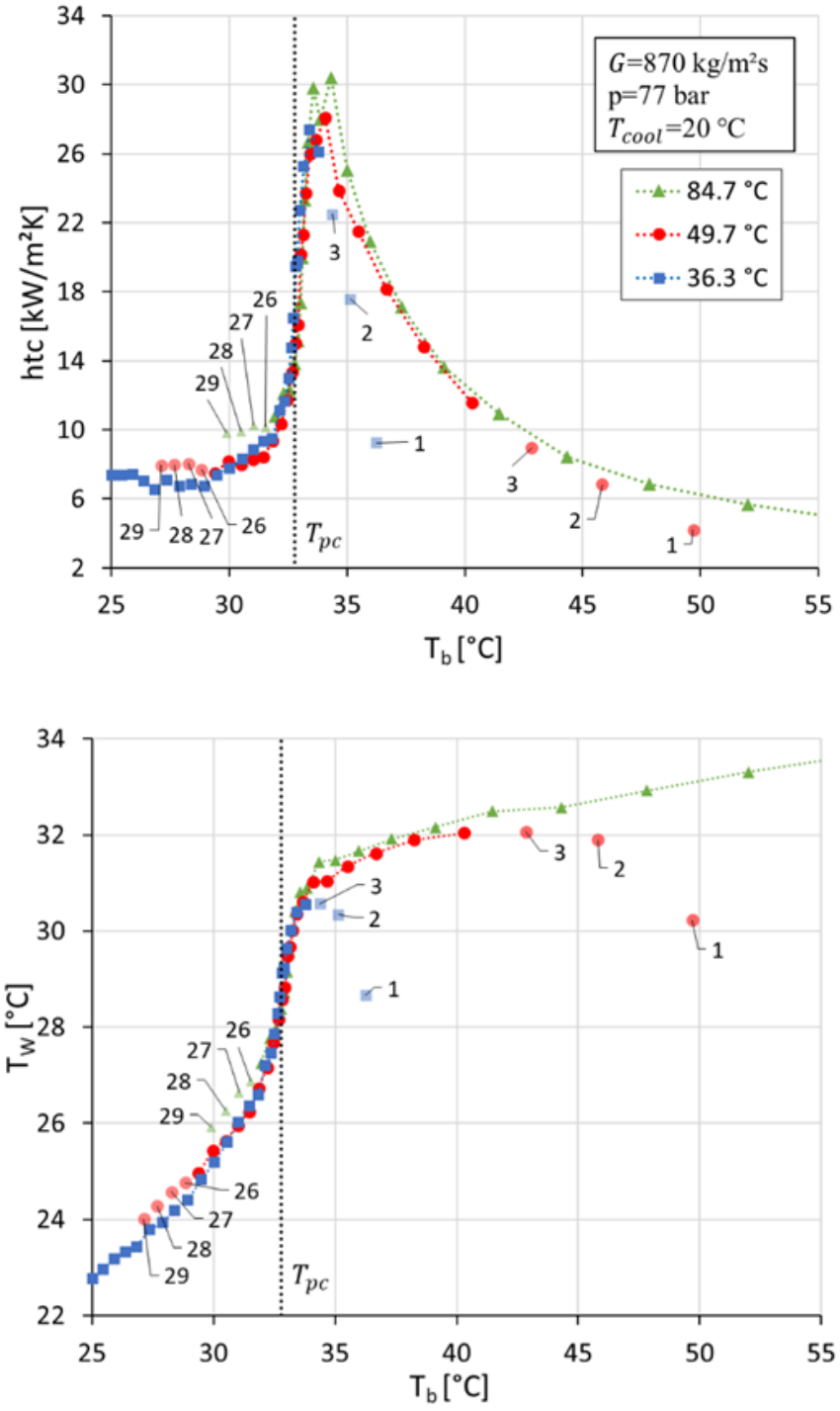

Figure 36: Effect of Inflow temperature; heat transfer coefficient and wall temperature as a function of the bulk fluid temperature

6.1.2 Development of a Nusselt heat transfer equation

To compare the experiments with different CO_2 temperatures, CO_2 mass fluxes and cooling temperatures, the ratio of the cooling flux to mass flux (q/G) is displayed as a function of the dimensionless bulk temperature ($T^* = (T_b + 273.15)/(T_{pc} + 273.15)$) (Figure 37). The experiments cover the temperature range of T* between 0.93 and 1.12. The highest g/G ratio reached is app. 280 J/kg. The purpose of the black line is to state the range of validity of the heat transfer correlation. The lowest boundary at 0.93 < T^*<1.03 was set at 15 J/kg, the boundary increases towards 100 J/kg at 1.03 < T^*<1.11. The upper boundary increases at 0.93 < T^*<1 from 15 to 140 J/kg. At T^*=1.0 a sudden increase towards 27J/kg exists, followed by a decrease towards 100 J/kg at 1 < T^*<1.11.

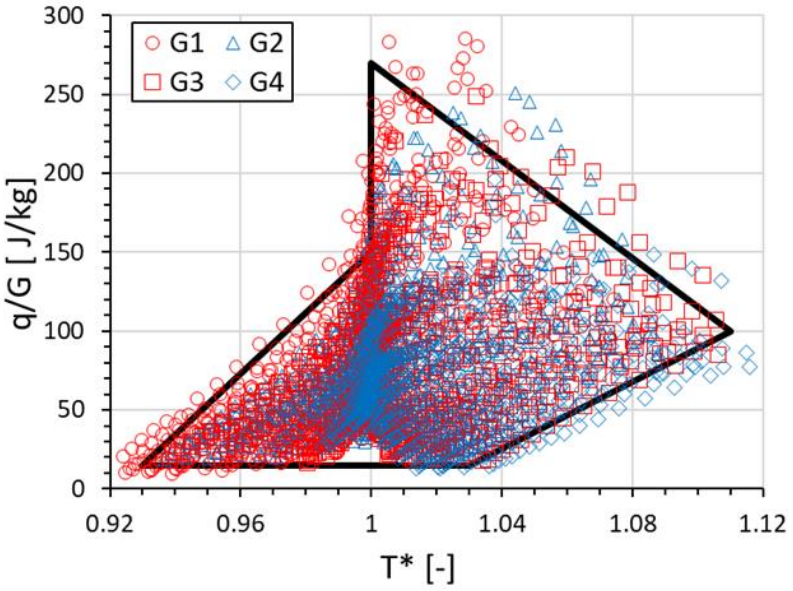

Figure 37: Ratio q/G as a function of T *for different mass fluxes

The heat transfer data obtained experimentally are compared with the predicted heat transfer with correlations of Dang and Hihara [58] and Liao and Zhao [59]. Figure 38 compares the heat transfer calculated with the Dang and Hihara model in orange circles, whereas the blue squares indicate the use of the Liao and Zhao model.

In detail, the Liao and Zhao model underestimates the experimental data with a significant amount of data points below the -40% line. The average deviation is -29.8% and the average absolute deviation is 38.2%. The Dang and Hihara equation leads to an average deviation of -2.3% and an absolute average deviation of 18.8%

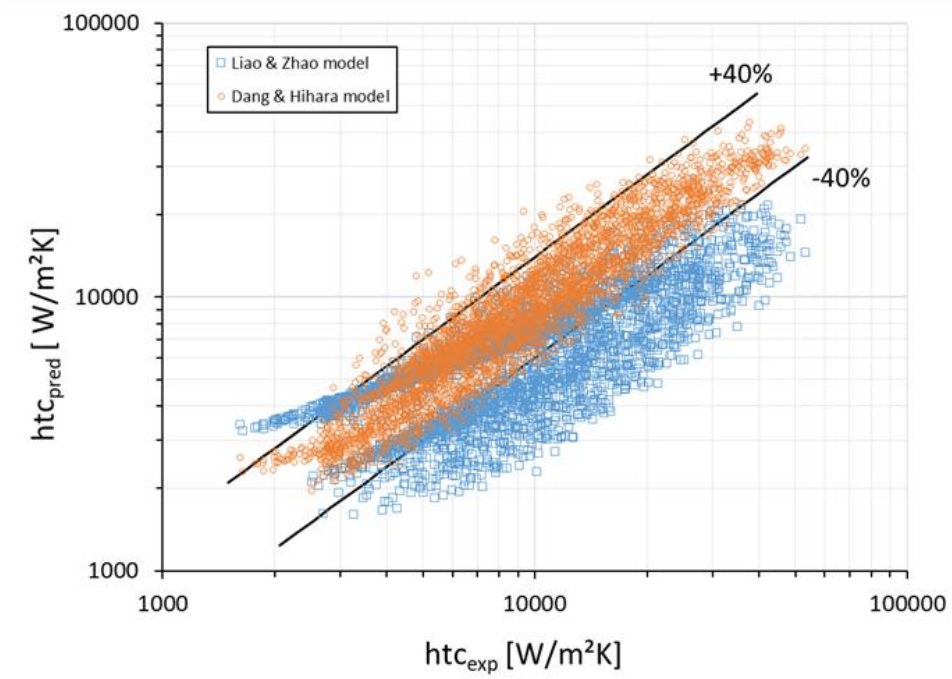

Figure 38: Experimental results compared with the predicted data

The heat transfer coefficients obtained with the two models do not match the experimental results satisfying. The absolute average deviations of 38.2% and 18.8% respectively, are too high. However, the Dang and Hihara equation is on average a reasonable accurate equation.

In Figure 39, the experimental parameter ranges of the present work are compared with the values by Dang and Hihara. The parameter ranges of the mass fluxes G, the heat flux q and the heat flux to mass flux ratio q/G is displayed as a function of the diameter D. The heat fluxes q are significantly higher in the present investigation, whereas the mass fluxes also reach lower values. The g/G-ratio is much higher due to the higher heat flux.

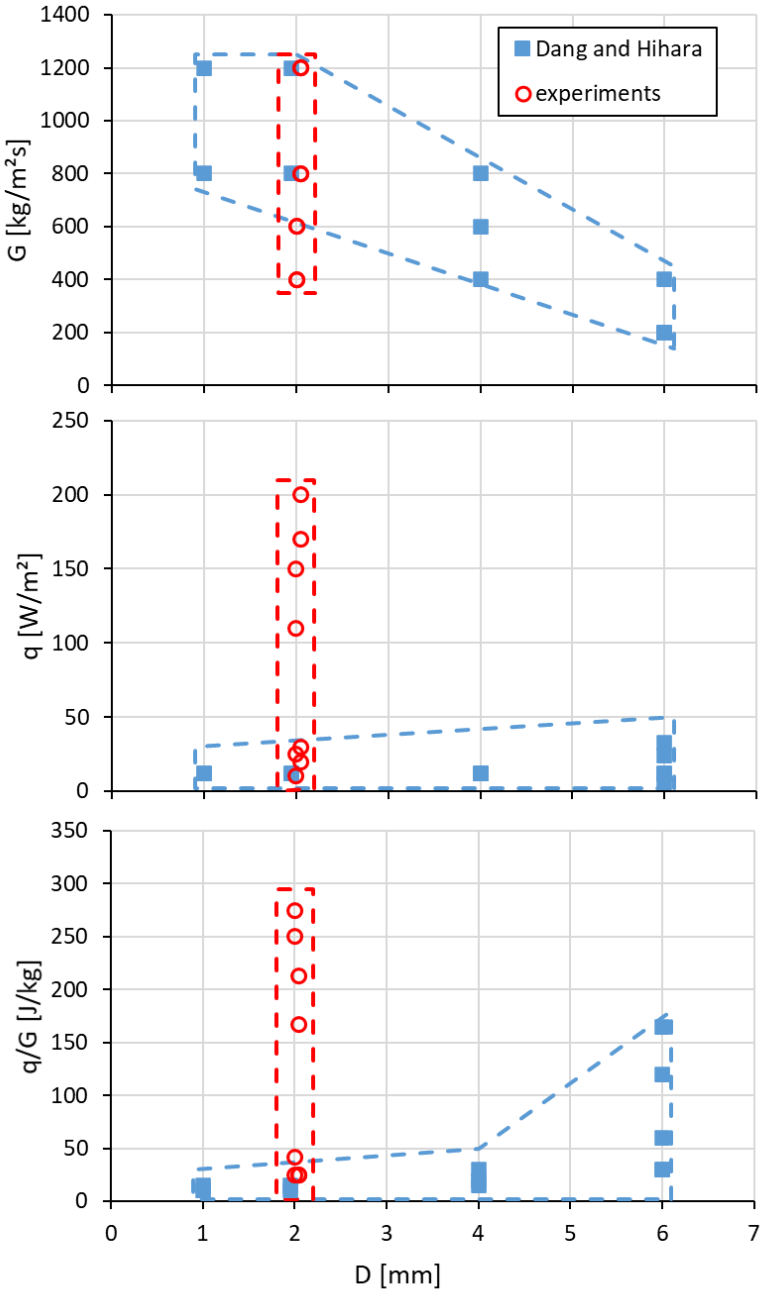

Figure 39: Heat flux q, mass flux G and heat flux to mass flux ratio g/G as a function of the diameter D

The comparison of the experimental data and the available correlations shows that it is necessary to propose a new correlation for the cooling heat transfer of CO_2 near the critical point. For this reason, an equation based on the Dittus-Boelter [91] correlation was considered. The equation was expanded with ratio terms of the fluid properties.

$$\mathrm{Nu}_{\substack{b\\w\\f}} = \mathrm{a}_0 * \mathrm{Re}_{\substack{\mathrm{b}\\w\\f}}^{\mathrm{a}_1} * \mathrm{Pr}_{\substack{\mathrm{b}\\w\\f}}^{\mathrm{a}_2} * \left(\frac{\rho_\mathrm{b}}{\rho_\mathrm{w}}\right)^{\mathrm{a}_3} * (C)^{\mathrm{a}_4} * \left(\frac{\lambda_\mathrm{b}}{\lambda_\mathrm{w}}\right)^{\mathrm{a}_5} * \left(\frac{\eta_\mathrm{b}}{\eta_\mathrm{w}}\right)^{\mathrm{a}_6} \quad (74)$$

$$C = \frac{\mathrm{c}_{\mathrm{p,b}}}{\mathrm{c}_{\mathrm{p,w}}}; \frac{\overline{c_p}}{c_{\mathrm{p,b}}}; \frac{\overline{c_p}}{\mathrm{c}_{\mathrm{p,w}}} \quad (75)$$

The different options of the correlation are displayed in Eq.74 and 75. The Nusselt number can be defined using fluid properties either of the wall, of the film or the bulk fluid properties. These options were tested and the highest accuracy was reached using the wall fluid properties. The second option is to implement $\overline{cp}$, which leads to three cases for the factor C. The ratio $\overline{c_p}/c_{p,b}$has been found out to deliver the best fit. The last option is to split the equation into two areas, representing the range above and below the pseudocritical temperature. Eq.76 shows the resulting correlation with its coefficients a_0-a_6. The coefficients of the equation were calculated by linearizing Eq.75 and solving a multiple linear regression. In Table 4 the coefficients of the proposed equation are displayed. The correlation was published in Wahl et al. [121].

$$\mathrm{Nu}_w = \mathrm{a}_0 * \mathrm{Re}_w^{\mathrm{a}_1} * \mathrm{Pr}_w^{\mathrm{a}_2} * \left(\frac{\rho_\mathrm{b}}{\rho_\mathrm{w}}\right)^{\mathrm{a}_3} * \left(\frac{\overline{c_p}}{c_{p,b}}\right)^{\mathrm{a}_4} * \left(\frac{\lambda_\mathrm{b}}{\lambda_\mathrm{w}}\right)^{\mathrm{a}_5} * \left(\frac{\eta_\mathrm{b}}{\eta_\mathrm{w}}\right)^{\mathrm{a}_6} \quad (76)$$

Table 4: Coefficient of the proposed heat transfer correlation

a0	a1	a2	a3	a4	a5	a6	
0.0495	0.771	0.455	1.450	-0.026	1.604	-2.623	for $T_w \geq T_{pc}$
0.0052	0.971	0.388	1.279	0.450	2.158	-2.923	for $T_w < T_{pc}$

The comparison between the experimental Nusselt number Nu_{exp} and the calculated values by the new equation Nu_{equ} is presented in Figure 40. The equation predicts the experimental results with an absolute average deviation of 7.7%. The proposed equation predicts the experimental results much better than the reviewed correlations.

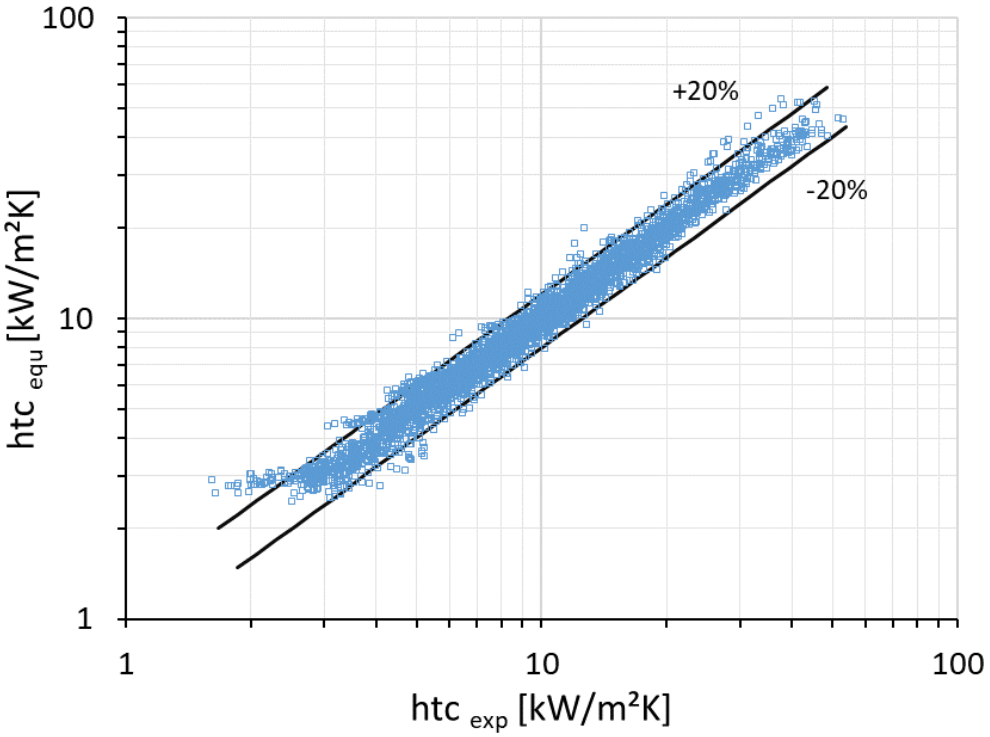

Figure 40: Comparison of predicted and experimental results

6.1.3 Summary of forced convection results

The cooling heat transfer of supercritical CO_2 was investigated experimentally. A test section was built up with local measurements of the tube wall along the cooled length to calculate the heat transfer coefficient by use of an integral method. Effects of mass flux, inlet pressure and cooling water temperature on the heat transfer were analyzed. It has been shown that the test section delivers reliable heat transfer performance data. In- and outflow effects have been separated clearly. The heat transfer coefficient increases with increasing mass flux. However, the influence of the mass flux on the htc is significantly stronger near the pseudocritical temperature. The peak value of the heat transfer coefficient appears at a temperature slightly higher than the pseudocritical value. Due to the fluid properties, the peak value of the heat transfer coefficient is shifted and flattened towards higher temperature for increasing pressure. Lower cooling media temperatures causes stronger subcooling of the wall, which leads to a trade-off between heat transfer performance in the early stage of the cooling process and the near pseudo critical region. A heat transfer correlation was developed with an absolute average deviation of 7.7%.

6.2 Vertical flow orientation

The vertical flow orientation was investigated in both the 2 mm (chapter 6.2.1) and 3 mm (chapter 6.2.2) diameter tube and presented in separate chapters respectively. A Summary of the experiments is presented in chapter 6.2.3.

6.2.1 2 mm tube

In this chapter, the heat transfer was derived for different boundary conditions in the upwards and downwards flow direction. The experiments were conducted with a constant cooling flux of $\dot{V}_{cool} = 100\ \mathrm{ml/s}$ with a CO_2 inlet temperature between 60 and 80 °C. Three different mass fluxes (400, 600, 1300 $\mathrm{kg/m^2s}$) and two cooling temperatures (20,25°C) were tested at a constant pressure of 80 bar (Table 5). The total number of cooling experiments in vertical flow orientation was 50.

Table 5: Experimental inlet conditions of vertical cooling in 2 mm tube

p_{CO2} (bar)	G_{CO2} (kg/m²s)	T_{cool} (°C)
80	400	20
	600	25
	1300	

In Figure 41 (top), the heat transfer coefficients for two experiments at mass flux G = 400 kg/m²s are compared. The green triangles are the upwards flow, and the red circles are the downwards flow. The comparison, which is at the lowest mass flux of the investigation, shows good agreement between the two flow orientations. Thus, no deterioration was detected in this experiment. In Figure 41 (bottom), the Jackson criterion $Gr/Re^{2.7}$ is displayed as a function of the bulk fluid temperature. The horizontal orange line shows the threshold value from the literature (Eq.19). The experiments only reach this value and do not exceed significantly.

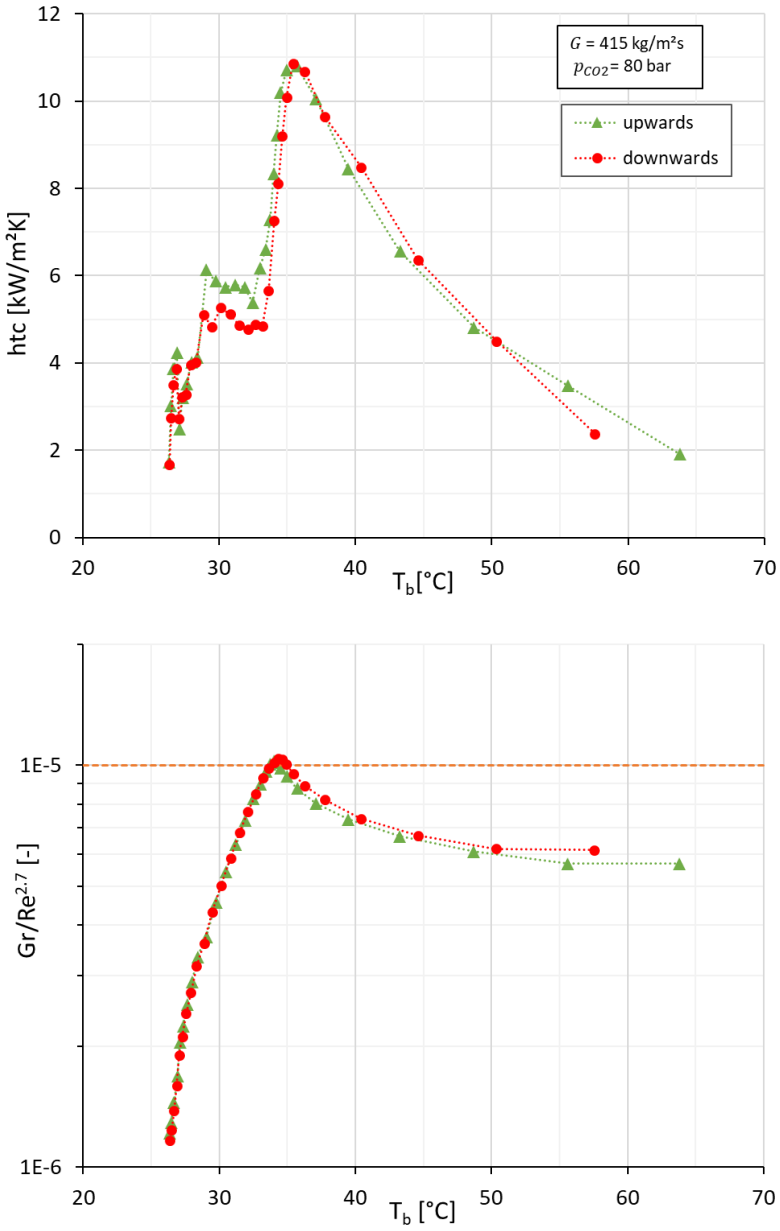

Figure 41: Effect of flow direction; heat transfer coefficient and $Gr/Re^{2.7}$ as a function of the bulk fluid temperature

At the higher mass flux of 600kg/m²s (Figure 42) and 1300kg/m²s (Figure 43) no significant difference between the two flow directions can be seen.

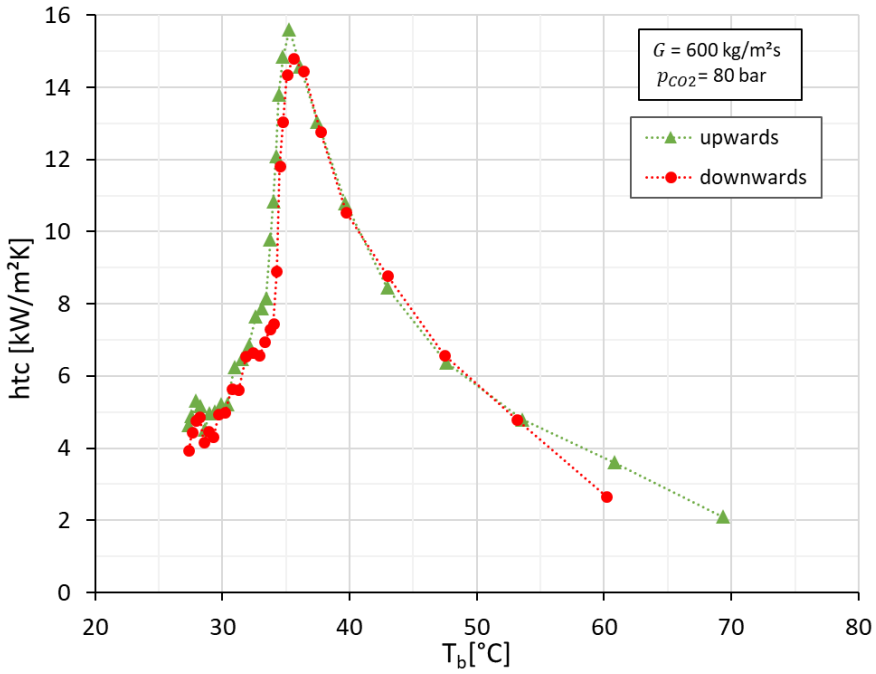

Figure 42: Effect of flow direction; heat transfer coefficient and as a function of the bulk fluid temperature at G=600kg/m²s

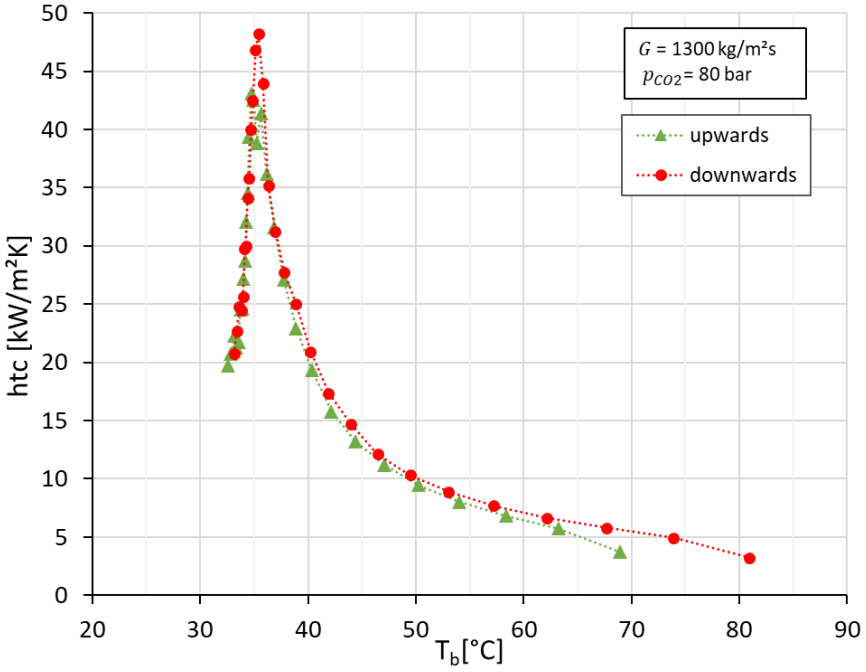

Figure 43: Effect of flow direction; heat transfer coefficient and as a function of the bulk fluid temperature at G=1300kg/m²s

In consideration, that no deterioration occurs at all three mass fluxes and the threshold value is reached, only a simple conclusion can be made from this experimental campaign. The overall comparison of the experiments is shown in Figure 44. Both flow orientations are close to unity. Thus, within the experiment in the 2 mm tube, the threshold value can be confirmed in terms of that no deterioration was detected below this value. As in the 2 mm tube no deterioration was detected, in the next chapter the experimental investigation of vertical flow orientation in the 3 mm tube is presented.

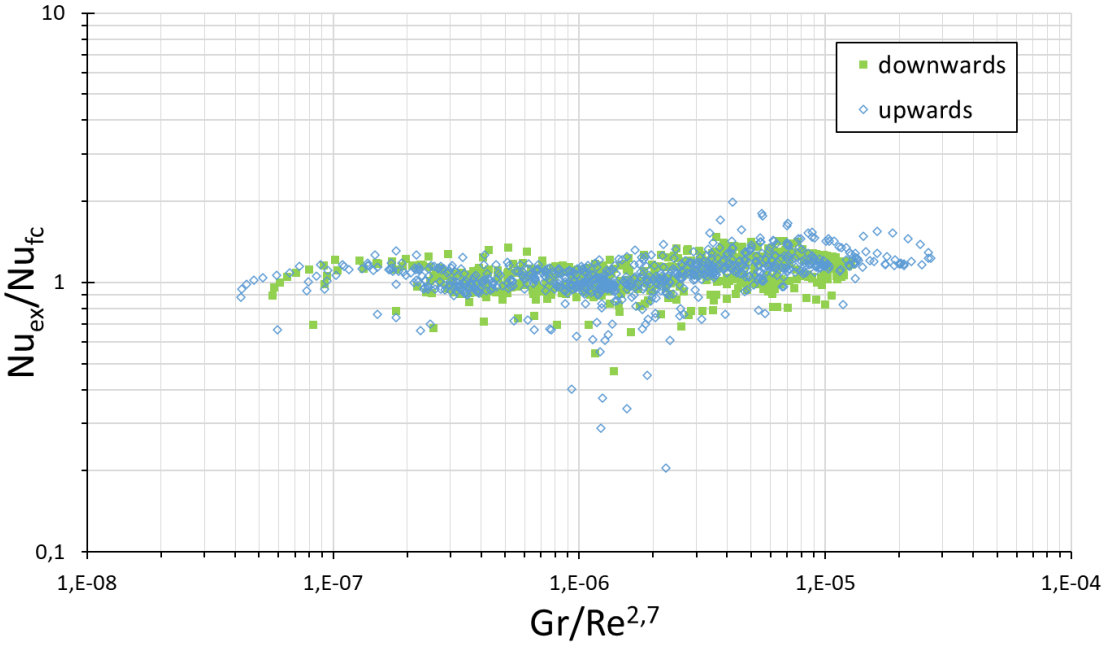

Figure 44: Evaluation of the heat transfer in vertical flow orientation in 2 mm tube

6.2.2 3 mm tube

In the vertical flow orientation, five mass fluxes (141, 177, 212, 283 and 354kg/m²s) were investigated at a constant pressure of 80 bar and CO_2 temperatures between 20 and 50°C. In total 204 experiments were conducted, with 45 in the upwards and 159 in the downwards flow direction

Table 6: Experimental inlet conditions of vertical cooling in 3 mm tube

p_{CO2} (bar)	G_{CO2} (kg/m²s)	T_{cool} (°C)
80	141/177/212/283/354	5-30

To limit the changes of the properties between the in- and outlet of CO_2, the temperature difference of the experiments is kept low if the bulk temperature is close to the pseudocritical temperature. Higher temperature differences were only measured far away from the pseudocritical temperature. It results in a difference of both approaches of between +10% and -20%. Near the pseudocritical temperature T_{pc}, htc_{ave} is up to 10% higher. Towards lower and higher temperatures, this tendency is reversed. In the liquid-like region, the htc_{LMTD} is up to 10% higher and in the gas like region up to 20% higher. However, to ensure the accuracy of $\dot{q}_{CO2}$ determination, it is important to measure above a certain temperature difference between in-and outlet. This is due to the high c_p close to T_{pc}. To meet both requirements the temperature difference between T_{in} and T_{out} close to T_{pc} was kept around $2\ K$. The inaccuracies based on the measurements was kept below 20%. This assessment shows the good agreement of both approaches. However, has little influence on the final evaluation of heat transfer deterioration which is based on a direct comparison of both flow direction. As of now, htc_{LMTD} is presented about htc.

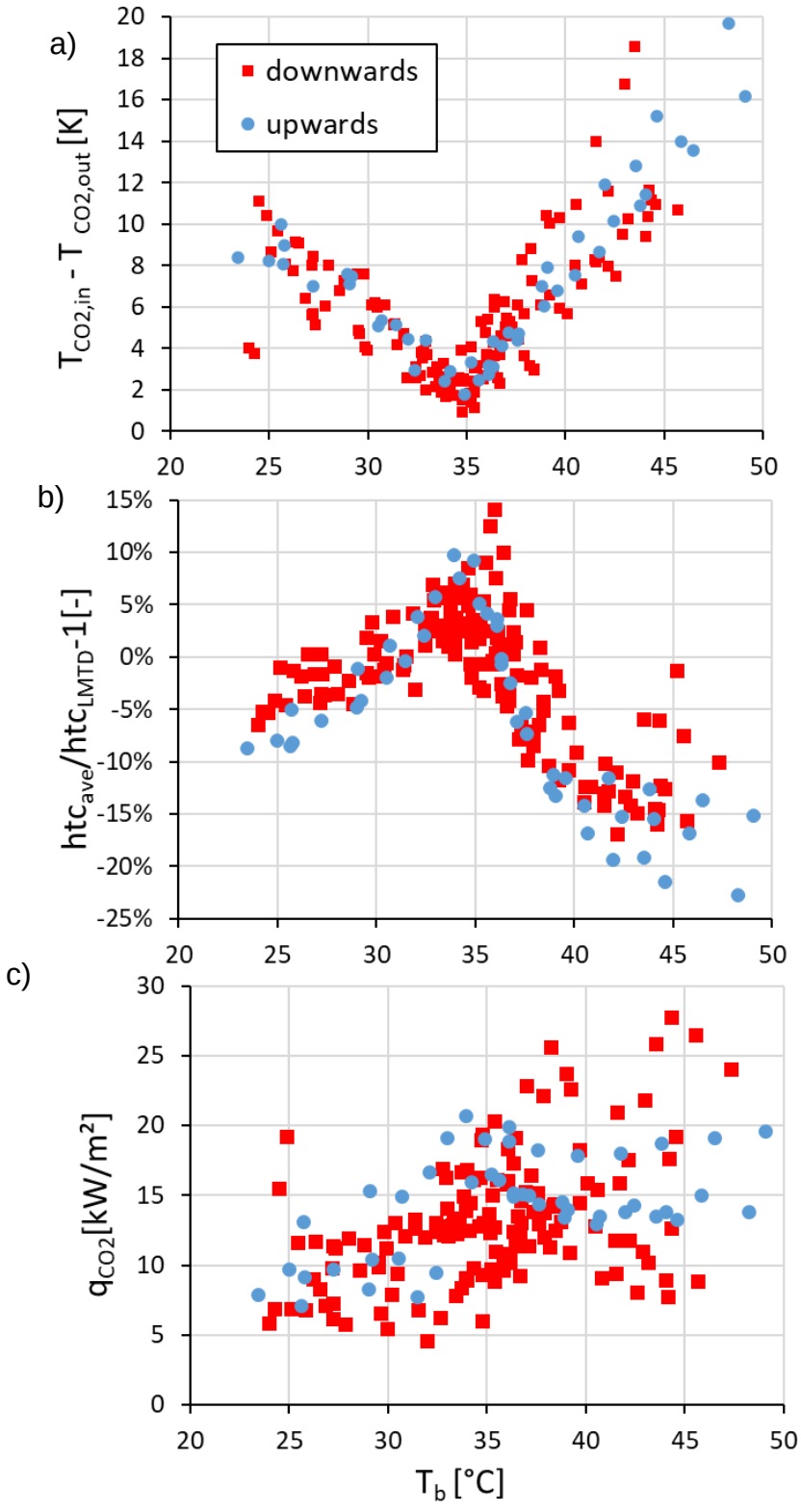

Figure 45: a) Temperature difference between CO_2 in- and outlet, b) the percentaged difference between htc_{ave} and htc_{LMTD} and c) heat flux q_{CO2} as function of the bulk temperature

In the vertical upwards flow, free convection induces additional turbulence. The effective direction of forced convection is upwards while free convection is in the downwards direction. The interaction of both effects leads to a parabolic velocity profile, which increases the velocity difference between the wall and the centreline and thus, increases the heat transfer.

In Figure 46, the heat transfer coefficients for mass fluxes from $141\ \mathrm{kg/m^2s}$ to $283\ \mathrm{kg/m^2s}$ are shown. As expected, all three mass fluxes show a similar trend with a peak close to the pseudocritical temperature. The enhancement of the mass flow leads to a higher heat transfer coefficient due to increases turbulent diffusion. Horizontal error bars represent temperature change from the inlet to the outlet of the test section, and vertical error bars represent the uncertainty in the measurement. Only two error bars are displayed to keep the diagram readable. Error bars are calculated based on the error propagation as displayed in chapter 5.3.2.

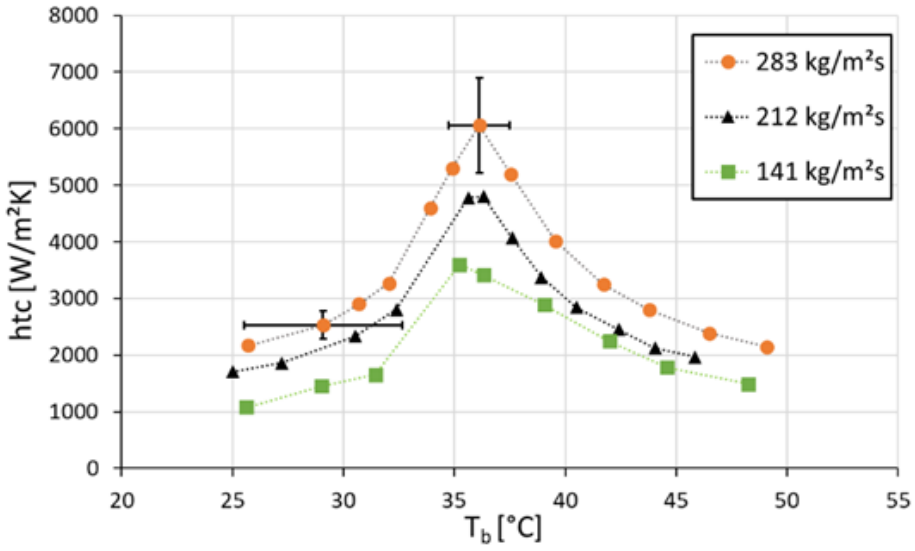

Figure 46: Heat transfer coefficient over bulk temperature for different mass flux in vertical upwards flow

In the vertical downwards flow, the effective direction of both, forced and free convection are in a downwards direction. In this case, an m-shaped velocity profile develops. Due to this interaction, the velocity difference between the wall and centerline is reduced, which can handicap the radial energy transfer. In the downwards flow, it is expected to see a significant deterioration of the heat transfer, which is different to the forced convection regime. In Figure 47, the heat transfer coefficients for mass fluxes from $141\ \mathrm{kg/m^2s}$ to $354\ \mathrm{kg/m^2s}$ in the vertical downwards flow are shown. With the reduction of the mass flux from $354\ \mathrm{kg/m^2s}$ to $283\ \mathrm{kg/m^2s}$, a constant decrease in the heat transfer coefficient can be seen. With the further reduction of the mass flux, clear evidence of mixed convection is present. In the liquid-like region ($T_b < 34.6°C$), the heat transfer coefficient drops between $212\ \mathrm{kg/m^2s}$ and $177\ \mathrm{kg/m^2s}$ relatively strong. However, the heat transfer coefficient remains constant with further reduction. At the pseudocritical temperature, a strong reduction of the heat transfer coefficient can be seen for $\mathrm{G} = 177\ \mathrm{kg/m^2s}$. At this mass flux, the abrupt change in the thermophysical properties seems to induce deterioration. The heat transfer coefficients at $G = 141\ kg/m^2s$ show a flat trend and thus, disagrees clearly from forced convection. In the temperature region $T_b < 33\ °C$ and $T_b > 42\ °C$, the heat transfer coefficients are constant with the further reduction from $\mathrm{G} = 177\ \mathrm{kg/m^2s}$ to $141\ \mathrm{kg/m^2s}$.

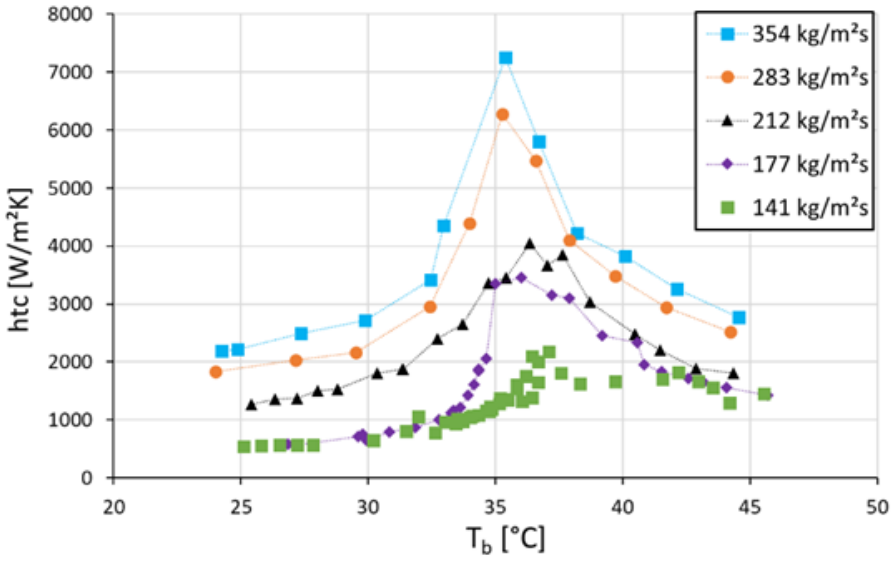

Figure 47: Heat transfer coefficient over bulk temperature for different mass flux in vertical downwards flow

In Figure 48, the wall temperatures are presented as a function of the bulk temperatures. In the upwards flow, the enhancement of the heat transfer with increasing mass flux leads to no difference in the wall temperature. The dotted lines visualize the tendencies. The differences between the gas and liquid-like region are significant. In the downwards flow, the heat transfer deterioration causes a strong decrease in the wall temperatures.

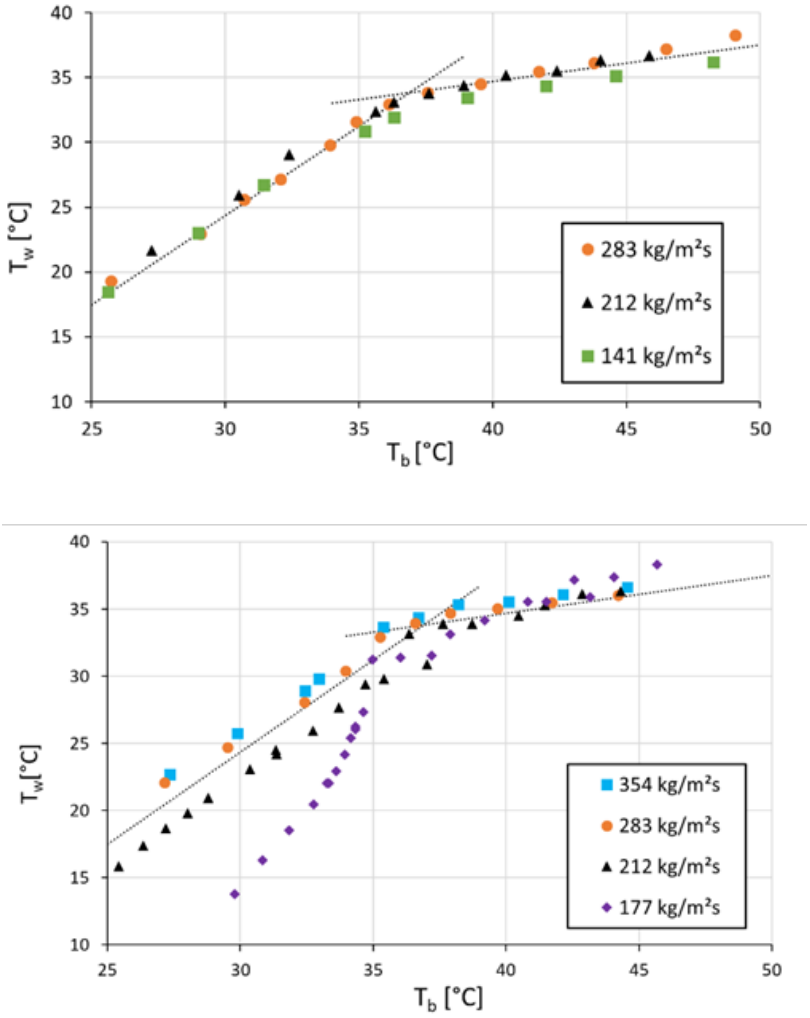

Figure 48: Wall temperature over bulk temperature for different mass flux in vertical upwards flow (top) and vertical downwards flow (bottom)

The comparison with existing heat transfer correlations is shown in Figure 49. Three different equations were chosen for comparison:

- Wahl et al. [121] (Eq.77), which was presented in chapter 6.1.2
- Dang and Hihara [58] (Eq.10) and
- Jackson and Hall [106] (Eq.29).

In the downwards flow at 141 kg/m²s, all correlations overestimate the heat transfer. The Jackson and Hall predictions the highest values at the pseudocritical temperature. In the liquid-like region, all correlation delivers similar over estimation. In the gas like region $T_b > 40°C$, the predictions are relatively good except for the Dang and Hihara equation. At the same mass flux in the upwards flow direction, the predictions are good, except for the underestimation by Jackson and Hall in the gas like region. In the downwards flow with mass flux of 212 kg/m²s, the experimental results are slightly overestimated in the liquid- and gas-like region. The deviations are much stronger close to the pseudocritical temperature. In the upwards flow, the predictions are overall quite good, with little stronger deviation at the pseudocritical temperature. At the mass flux of 283 kg/m²s, both flow direction shows same tendencies. Fairly good agreement in the liquid-like region and overestimation by Wahl et al. and Dang and Hihara and underestimation by Jackson and Hall.

In Figure 50, the ratio Nu_{exp}/Nu_{fc} is displayed as a function of the Jackson criterion $Gr/Re^{2,7}$. The three different Nusselt correlations as introduced above were chosen as forced convection equations. Additionally, the experimental measurements are divided into liquid-like ($T<T_{pc}$) and gas-like regions ($T>T_{pc}$).

In Figure 51, the overall evaluation is presented with the regression lines for both the downwards and the upwards flow. For the downwards regression, a ±15% error line is shown at $Gr/Re^{2,7}<10^{-5}$ and ±40% at $Gr/Re^{2,7}>10^{-5}$. The negative gradient of the regression in the downwards flow direction can be assigned to the deteriorated heat transfer.

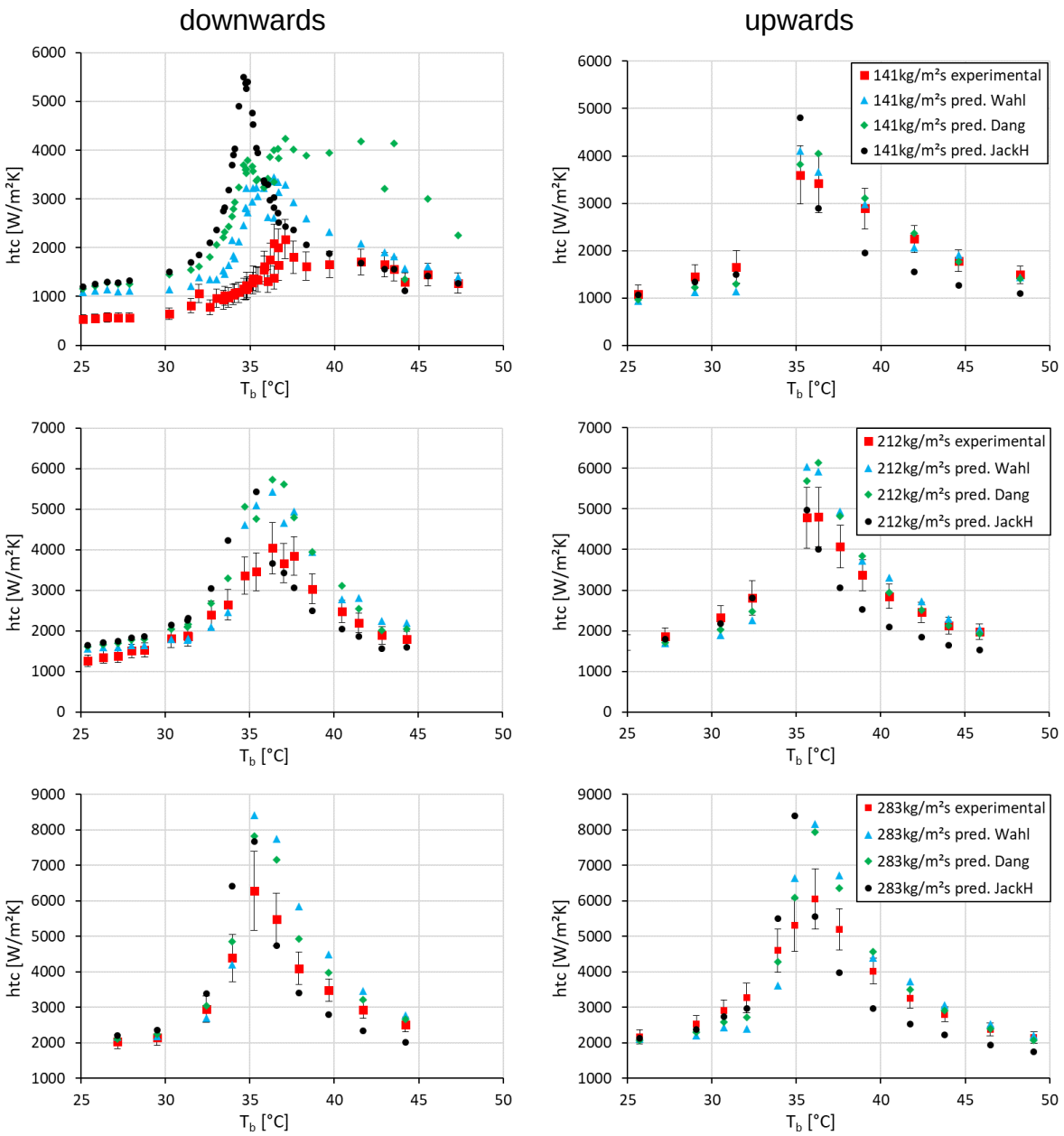

Figure 49: Measured heat transfer coefficient compared with predicted values by Wahl et al., Dang and Hihara, Jackson and Hall for 141, 212 and 283 kg/m²s

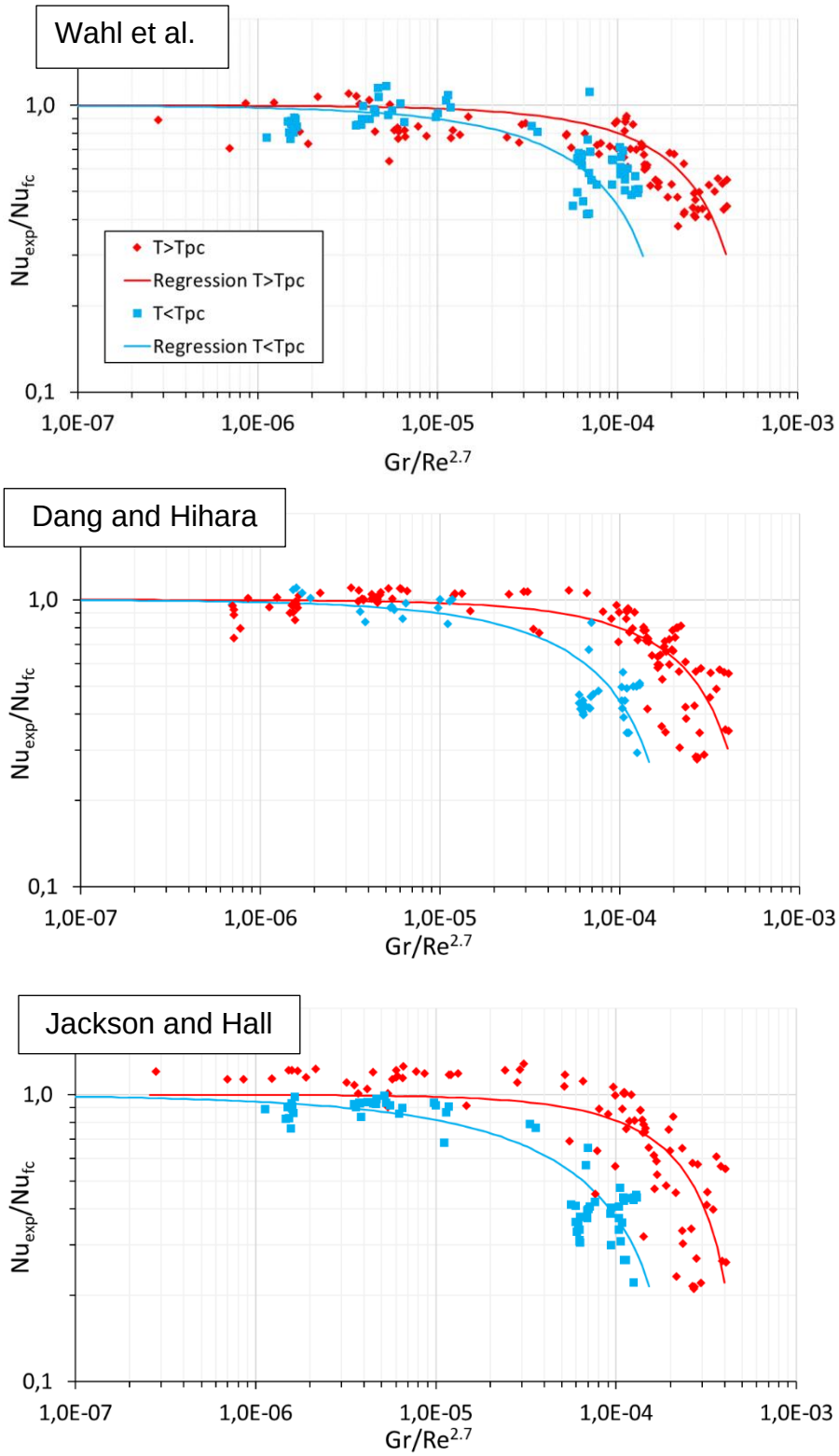

Figure 50: Nu_{exp}/Nu_{fc} as a function of the Jackson criterion $Gr/Re^{2,7}$

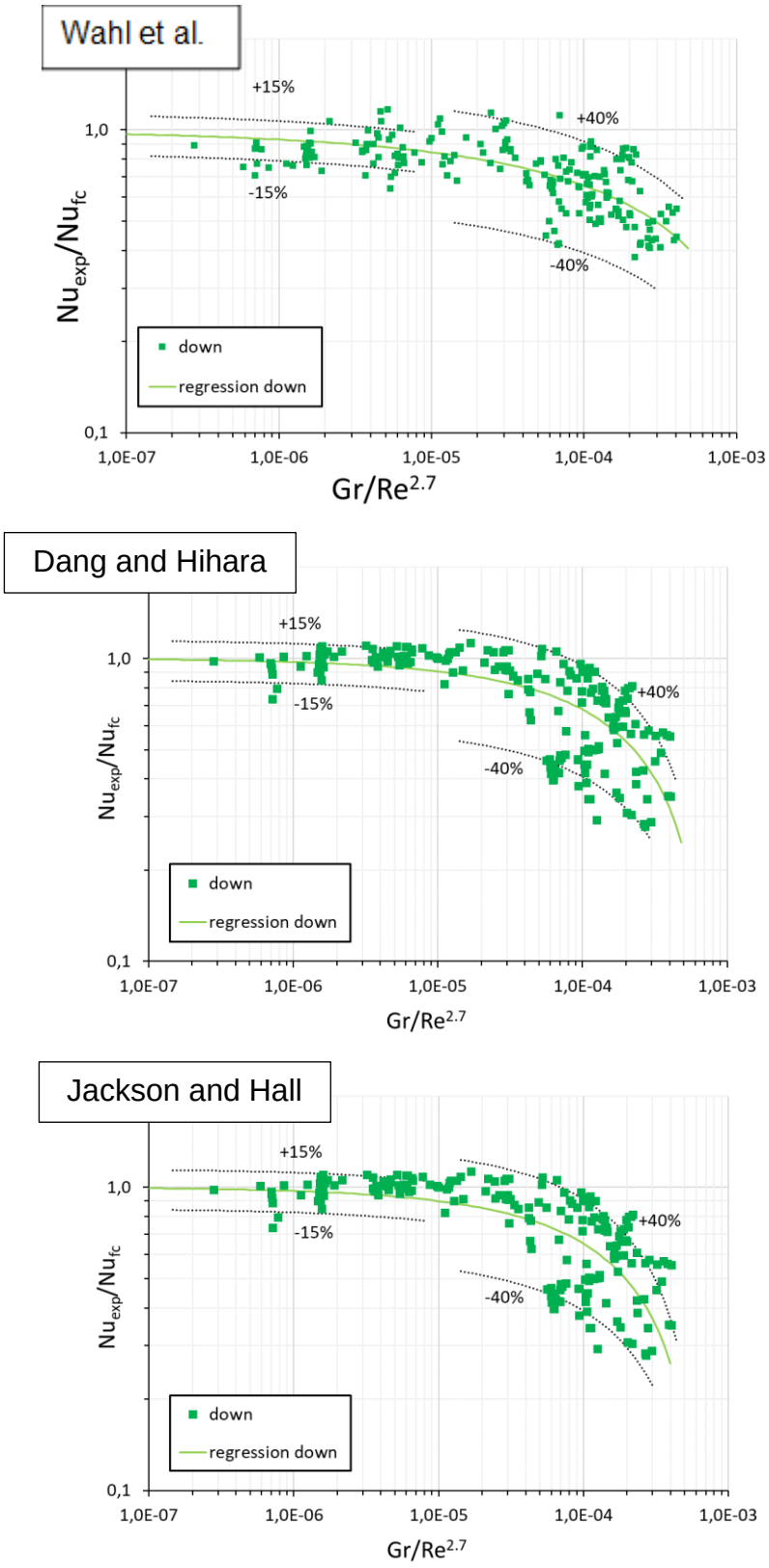

Figure 51: Overall data evaluation with the regression lines for both flow directions

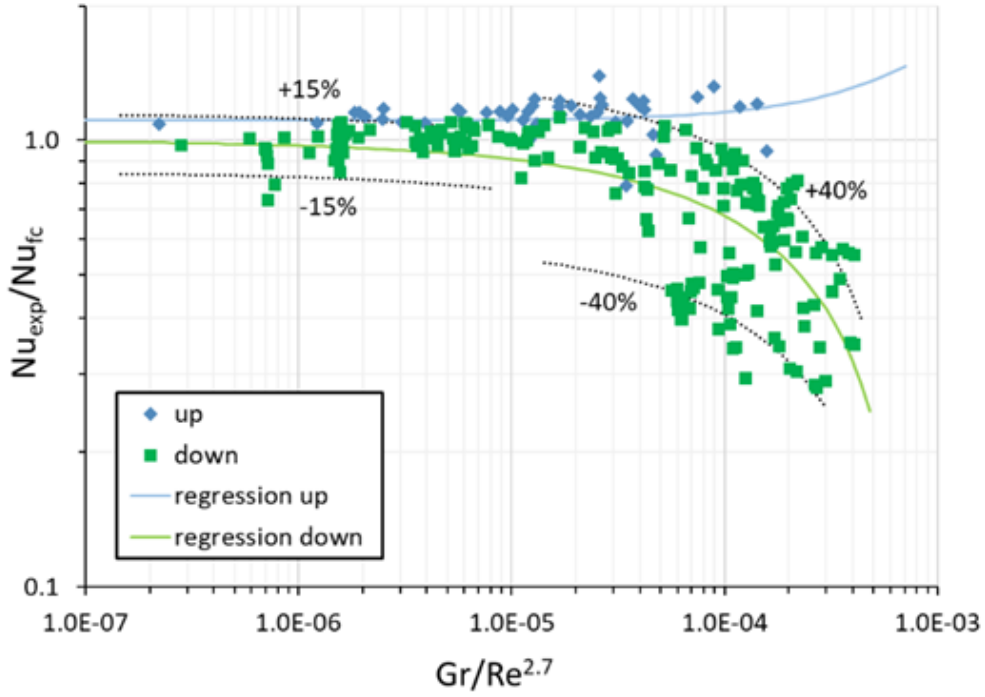

Figure 52: Evolution of ratio Nu_{exp}/Nu_{fc} with the mixed convection parameter $Gr/Re^{2.7}$ of the downwards and upwards flow based on the Dang and Hihara equation

In Figure 52, the results are presented in dimensionless form. For low values of the mixed convection parameter $\mathrm{Gr}/\mathrm{Re}^{2.7}$, forced convection is the dominant mechanism of heat transfer. The influence of free convection is negligible and the ratio $\mathrm{Nu}_{\mathrm{exp}}/\mathrm{Nu}_{\mathrm{fc}}$ is close to unity for both flow directions. This also indicates a good agreement with the chosen forced convection equation by Dang and Hihara [58]. As the parameter $\mathrm{Gr}/\mathrm{Re}^{2.7}$ increases, buoyancy forces are stronger, and differences appear between the flow direction. Heat transfer is enhanced in upwards flow and deteriorated in downwards flow. In the downwards flow a clear trend can be seen, however, the mean variation is relatively high. The transition to free convection, which is characterized by the recovery of the $\mathrm{Nu}_{\mathrm{exp}}/\mathrm{Nu}_{\mathrm{fc}}$ the ratio was not detected within the experimental boundary conditions. Eq. 77 and 78 are the functions of the plotted regression of Figure 52.

upwards:
$$\frac{\mathrm{Nu_b}}{\mathrm{Nu_{fc}}} = 1.107 + 510.2 * \frac{\mathrm{Gr}}{\mathrm{Re}^{2.7}} \qquad (77)$$

downwards:
$$\frac{\mathrm{Nu_b}}{\mathrm{Nu_{fc}}} = 1 - 46.4 * \left(\frac{\mathrm{Gr}}{\mathrm{Re}^{2.7}}\right)^{0.540} \qquad (78)$$

In Figure 53, the final results of the downwards flow are compared with the regression line of Bruch et al [105]. As an error estimation of the presented work, a regression line was processed with the data of the upper error limit as well as the lower error limit. The experimental data is displayed in the green line. The experiments show deterioration at higher $\mathrm{Gr}/\mathrm{Re}^{2.7}$ values. This might indicate that the tube diameter is a relevant factor of the heat transfer deterioration in cooling heat transfer. It seems like that the phenomena of deterioration and recovery is shifted towards higher $\mathrm{Gr}/\mathrm{Re}^{2.7}$ values. The heat transfer recovery is expected to appear near the end of the plotted regression at $\mathrm{Gr}/\mathrm{Re}^{2.7} \approx 10^{-3}$. However, the experimental facility with its fixed cooling length would reduce the accuracy to an unacceptable level with the further reduction of the mass flux.

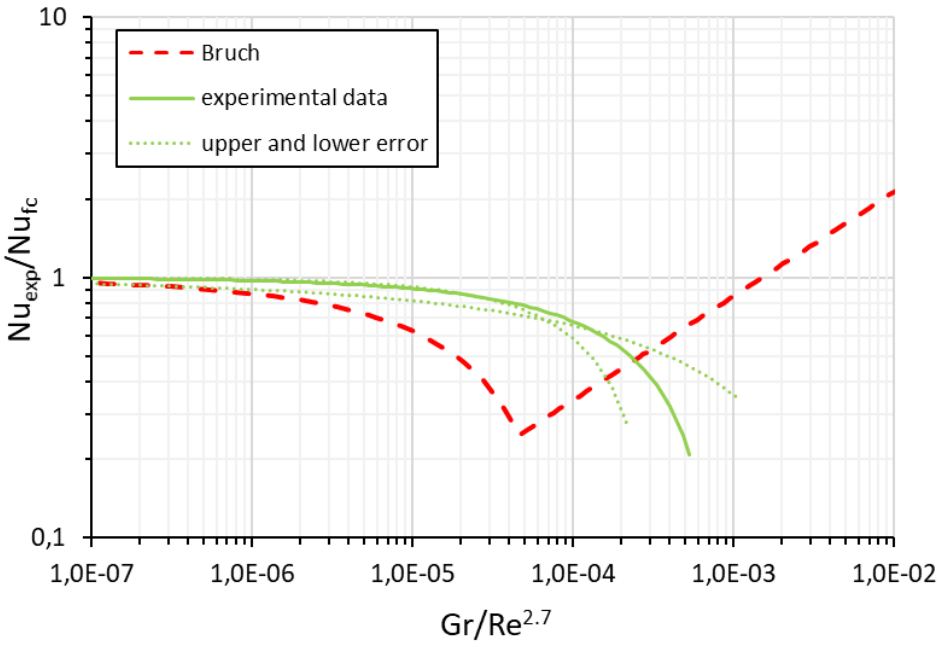

Figure 53: Comparison of proposed correlation of downwards flow with the correlation by Bruch et al. [105]

6.2.3 Summary of vertical flow results

In the 2 mm tube, no deterioration was observed within the measured experimental boundary conditions. The evaluation based on the Jackson Criterion and the threshold value was reached, however, not significantly exceeded. As for the 2 mm tube, the threshold value can be confirmed.

In the 3 mm tube, significant deterioration was detected in the lower mass flux region of the downwards flow. The deterioration was evaluated based on three different heat transfer equations with no significant difference. The regression of the data points was compared with the only available literature correlation for deterioration of the cooling case. The dimensionless evaluation showed differences compared to the literature data. The comparison might indicate that the tube diameter is a relevant factor of the heat transfer deterioration in cooling heat transfer. It seems like that the phenomena of deterioration and recovery is shifted towards higher $\mathrm{Gr}/\mathrm{Re}^{2.7}$ values for smaller tube diameters.

6.3 Buoyancy effects in horizontal flow in 3 mm tube

To investigate flow stratifications in the CO_2 flow, it is necessary to ensure a turbulent heat transfer with uniform temperature distribution in the annulus of the test section. The pretesting is necessary to ensure, that the temperature differences in the tube wall is exclusively induced by stratification in the sCO_2 flow and not by the annulus flow. Pretests were conducted to investigate the occurance of temperaturstratifications in the annulus cooling flow.The testing was done with hot water in the tube as the heat source and the cooling water in the annulus at 20°C. The test section was extended with thermocouples reaching into the middle of the annulus flow area. The experiments were conducted twice, with additional thermocouples on top (Option 1) and bottom (Option 2) of the flow (Figure 54).

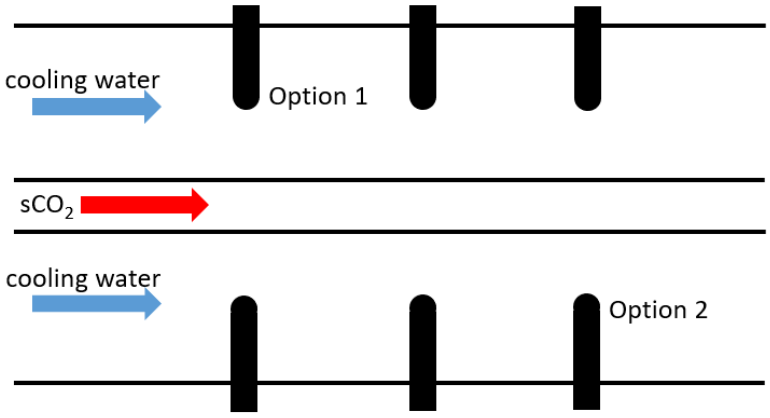

Figure 54: Experimental set-up for pre-testing of cooling water flow

The measurement settings of the heat flux and the volumetric cooling flow $\dot{V}_{cool}$ in the annulus are displayed in Table 7. In total 16 experiments with all combinations of the two parameters were conducted.

Table 7: Parameter settings for pretesting of cooling flow

q_{CO2} (kW/m²)	V_{cool} (ml/s)
12	10
18	20
24	30
30	50

The maximum temperature difference ΔT between the measurement in the top and the bottom of the annulus are displayed in Figure 55. The 10 ml/s flow shows relatively high differences even at the lowest heat flux and is increasing up to 7.5 K at the highest heat flux. The 20 ml/s flow is close to zero at the lowest cooling heat flux and increases to approximately 2 K at the highest heat flux. Almost no stratification is detected in the 30 ml/s flow, where only a ΔT could be measured in the highest heat flux. No significant temperature differences were measured in the 50 ml/s flow.

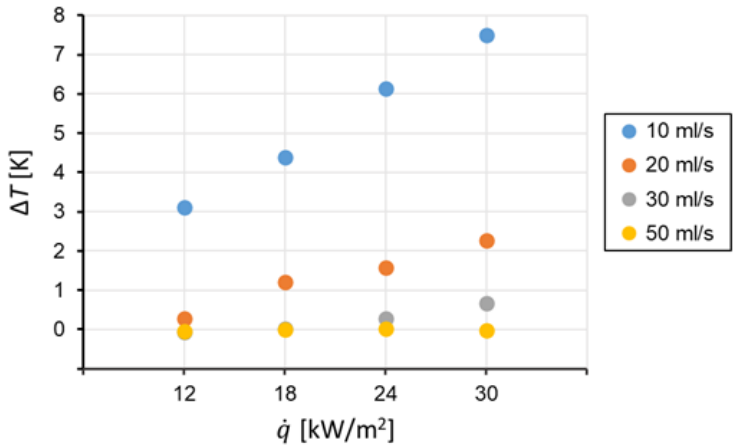

Figure 55: The maximal measured temperature difference between top and bottom in pretesting of annulus flow

In Figure 56, the temperature measurement is displayed for the heat flux of 30 kW/m² as a function of the axial measurement position. x = 0 and x = 500 mm are denoted as the measurement positions inlet and the outlet temperatures, respectively. The agreement of the inlet and outlet temperatures represent the repeatability of the experiments as the same heat flux and volume flow is applied. In the low volume flow experiments the heated water at the tube circumference rises to the top of the annulus due to buoyancy. This effect is reduced with increasing volumetric flow due to two reasons. The total temperature difference of the experiments decreases and the turbulent mixing increases. The pretests show that at 50 ml/s flow, the temperature differences in the annulus is neglectable.

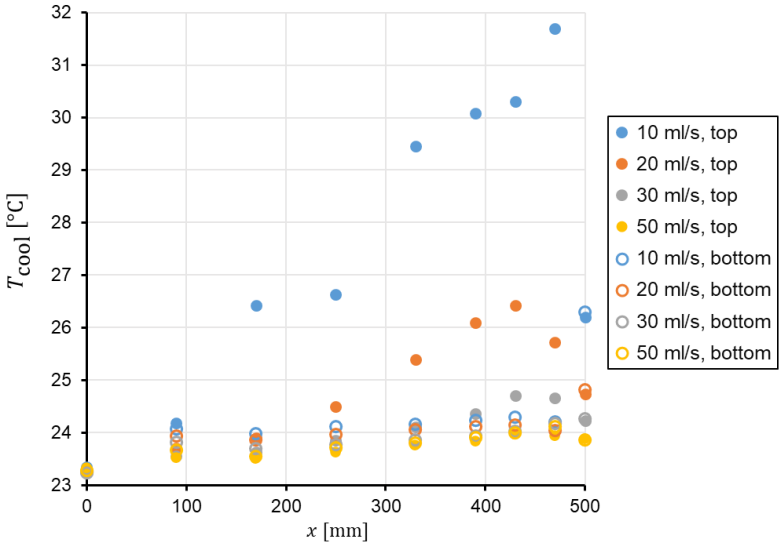

Figure 56: Temperature of cooling water over the length of the test section for different volumetric cooling fluxes at q = 30kW/m²

The measurement parameters for the CO_2 cooling are displayed in Table 8. Three different mass fluxes were tested at a volumetric cooling flow of 60 ml/s which is by far in the turbulent mixed flow regime. The CO_2 temperatures were between 50 and 20 °C. The cooling heat flux was constant at 12 W/m²K.

Table 8: Parameter settings for CO_2 testing

p_{CO2} (bar)	G_{CO2} (kg/m²s)	Q_{CO2} (W/m²K)
80	141	12
	212	
	283	

Figure 57 displays the wall temperatures (left) and the heat transfer coefficients (right) for all three mass fluxes. The hollow and filled triangles display the measurements on the bottom and top, respectively. For all three mass fluxes, the wall temperature shows in the liquid-like region a gradient of $(\mathrm{dT_{CO2,W}}/\mathrm{dT_{CO2,b}}) > 1$, a bend in the pseudocritical temperature and the gas like region a gradient of $(\mathrm{d}T_{\mathrm{CO2,W}}/\mathrm{d}T_{\mathrm{CO2,b}}) < 1$. Temperature stratification is present in the liquid-like region of the 141 and 212 kg/m²s experiments. The difference between the top and bottom wall temperatures is illustrated with a linear regression at $\mathrm{T_{CO2,b}} < 34°\mathrm{C}$. The difference is 2.5 K at 141 kg/m²s and 1.7 K at 212 kg/m²s. No stratification is present in the liquid-like region in the 283 kg/m²s experiments as well as in the gas like region of all mas fluxes. The absence of

stratification in the gas like region can be explained by the higher turbulence due to the lower viscosity. In the liquid-like region, the reduction of the stratification is due to the increased turbulence based on the increased Reynolds number. The effects in the pseudocritical region are not clear. Especially the very small temperature difference between wall and bulk at 212 kg/m²s requires further investigation.

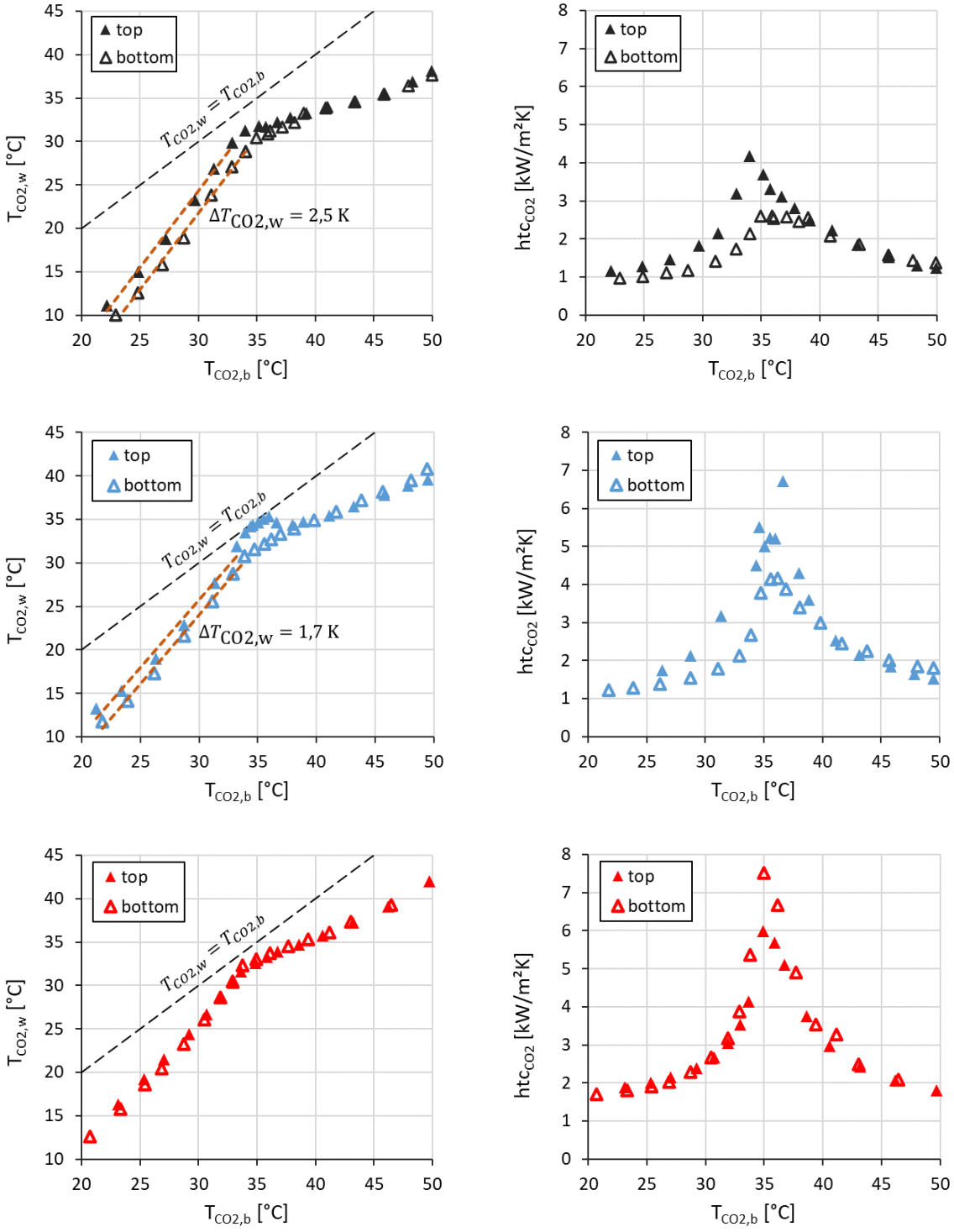

Figure 57: Wall temperature and heat transfer coefficient as a function of the bulk temperature (black: 141 kg/m²s ; blue: 212 kg/m²s ; red: 283 kg/m²s)

In Figure 58, the three introduced buoyancy parameters are displayed for all experiments as a function of the bulk temperature. The green line is the proposed value by the author's investigation (Eq. 32-34). The black horizontal line indicates the approximate value of the experimental investigation whereas the liquid-like region at 141 kg/m²s and 212 kg/m²s had significant stratification. No significant stratification was detected in the gas-like region.

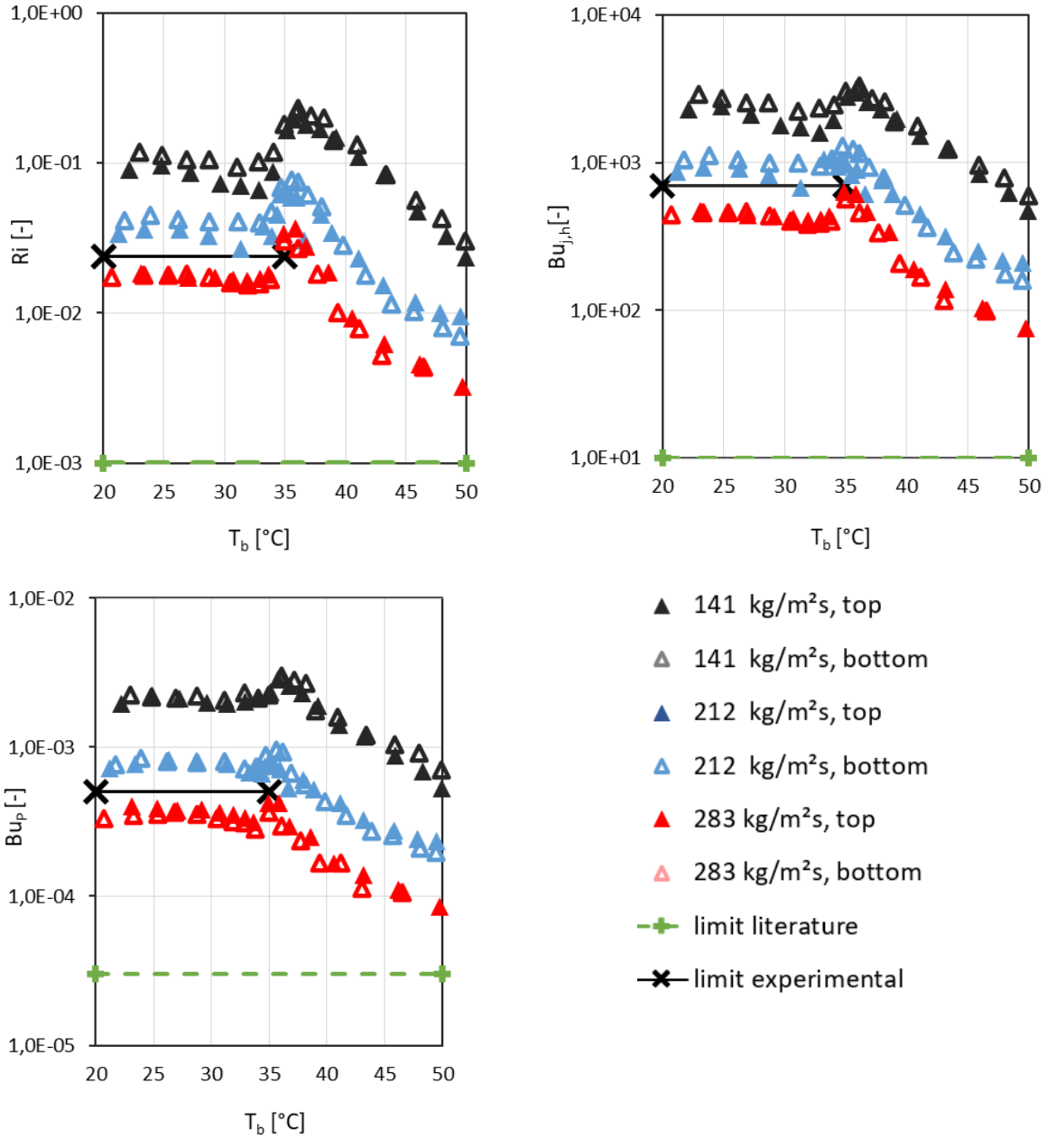

Figure 58: Buoyancy parameters for all experiments as a function of the bulk temperature compared to the proposed limit

The evaluation of the experimental results based on the buoyancy parameter was displayed as a function of the bulk temperature. In the liquid-like region, a threshold value of the experimental results was implemented with the black line. In this temperature range, the experimental results show higher values than the proposed literature data. In the gas-like region, no stratification was detected, thus, no comparison is possible. The results indicate that stratification in the cooling case might be influenced by the tube diameter or in general different to that of the heating case.

6.4 Pressure drop evaluation

The pressure drop evaluation of the two tubes is presented separately, the 2 mm tube in chapter 6.4.1 and the 3 mm tube in chapter 6.4.2. The material of the 2 mm tube is cooper and the 3 mm tube is stainless steel which leads to different surface roughness. For both tubes, an isothermal measurement campaign is presented first to validate a friction factor correlation which is then applied to the cooling experiment. The summary of the experiments is presented in chapter 6.4.3.

6.4.1 2 mm tube

The purpose of this chapter is to investigate the cooling pressure drop of sCO_2. In the cooling process, a sharp decrease of the fluid density might occur in both, axial and radial directions. This is in general the difficulty in predicting the pressure drop performance. As a starting point, 90 uncooled measurements were conducted with a wide range of parameters as displayed in Table 9. The annulus of the test section was left empty, that no heat transfer was possible. A small temperature difference was still present in the experiments. However, it was mainly within the range of 3 K and had theoretically only marginal influence on the fluid density.

Table 9: Isothermal measurements

p_{CO2} (bar)	G_{CO2} (kg/m²s)	T_{CO2} (°C)
77	400	20
81	850	25
85	1300	40
		45

A part of the experimental campaign is shown in Figure 59. The experiments at 25 °C and 45 °C were selected based on the only small difference in the density between the pressures, thus, all three pressures deliver similar results. The frictional pressure drop is displayed as a function of the mass flow. Additionally, a cubic regression line illustrates the expected dependency of the pressure drop from the mass flow. The absolute difference of the two temperature ranges is implemented by a density difference of approximately 40%.

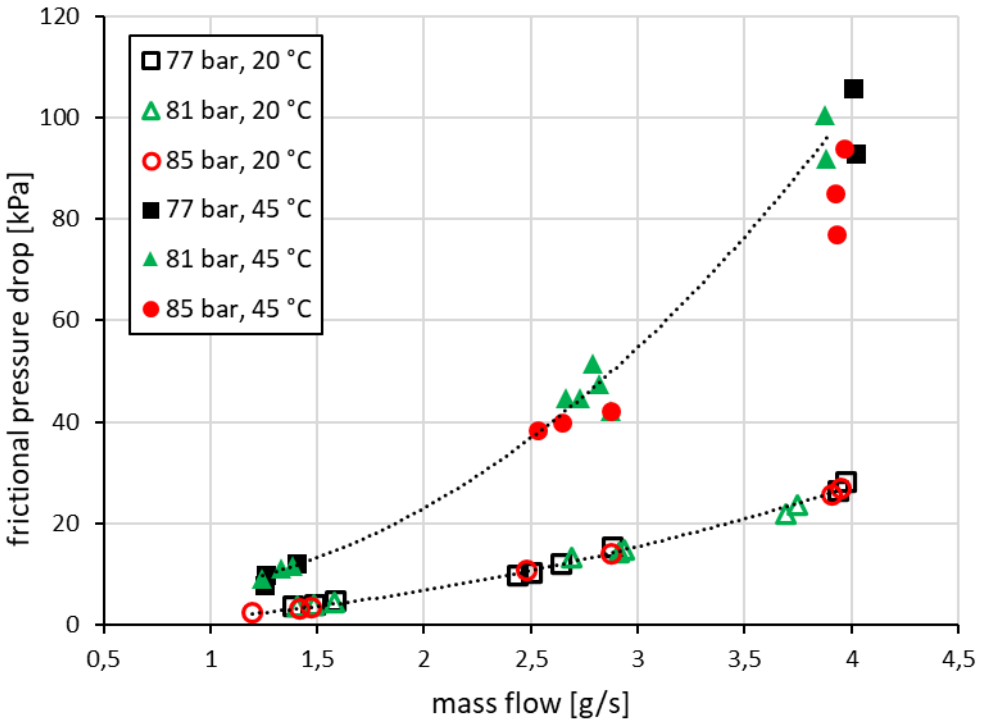

Figure 59: Measured frictional pressure drop as a function of mass flow in uncooled conditions for three pressures and two temperature regions

As the next step, the dimensionless friction factor based on the measured friction pressure drop, the flow density, the tube diameter and the tube length is evaluated. A dimensionless examination is meant to produce a universally valid correlation. Thus, the friction factor is plotted as a function of the Reynolds number in Figure 60. The measured tube roughness (18.2µm) applied to Eq.79 leads to a predicted function of $\xi_{pred}(Re)$:

$$\frac{1}{\sqrt{\xi}} = -2\lg\left[\frac{2{,}51}{Re_i\sqrt{\xi}} + \frac{K/d_i}{3{,}71}\right] \tag{79}$$

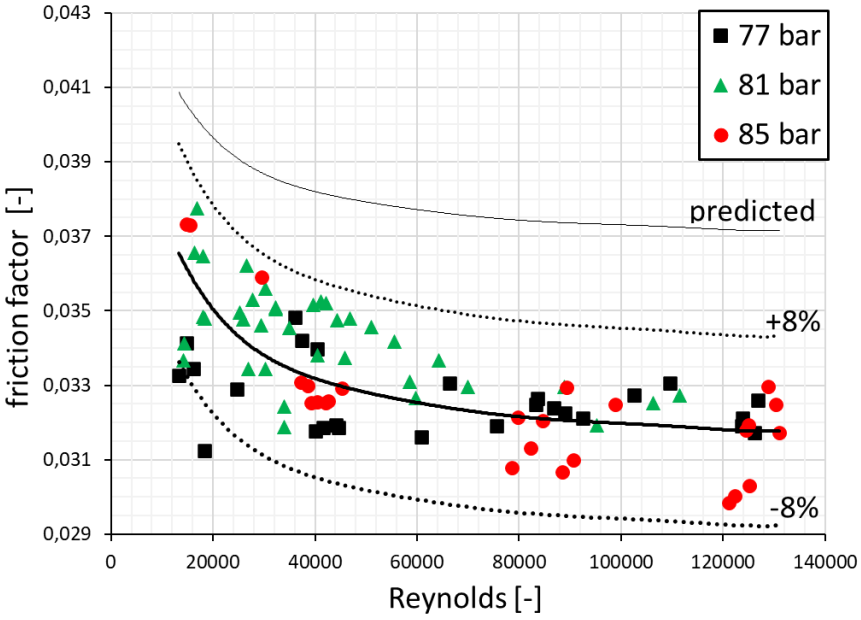

Figure 60: Dimensionless friction factor as a function of Reynolds in uncooled conditions for three pressures

The same correlation is used to correlate the experimental values. Additionally, the ±8% error line is applied. The correlated tube roughness is 10.2 µm with an average absolute deviation of 3.3%.

The final objective of the pressure drop evaluation is to predict the pressure drop of the cooling process. The fluid enters the test section with low density and leaves with higher density. Thus, the deceleration effect is considered. In the inflow and outflow, an isothermal section is present, this pressure drop is calculated always with the bulk properties. The frictional pressure drop for each subsection is calculated based on Eq.80. Three different options were chosen by considering the bulk, film and wall properties respectively. The fourth option is the prediction equation by Fang and Xu [115] which is presented in Eq.42-44.

$$p_{fric} = \frac{1}{2} * \xi(Re_{\substack{b\\f\\w}}) * \frac{l}{d} \frac{G^2}{\rho(T_{\substack{b\\f\\w}}, p)} \tag{80}$$

The results are displayed in Figure 61 and quantified in Table 10. The bulk properties by tendency overestimate whereas the wall properties underestimate the measured pressure drop with an average deviation of 12.8% and -16.4% respectively. The film properties and the Fang and Xu equation show a good agreement with an average deviation of -0.6% and 3.9%, respectively. The average absolute deviation is chosen

for a final evaluation where both, the film properties and the Fang equation, deliver quite similar values of 3.7% and 3.9%.

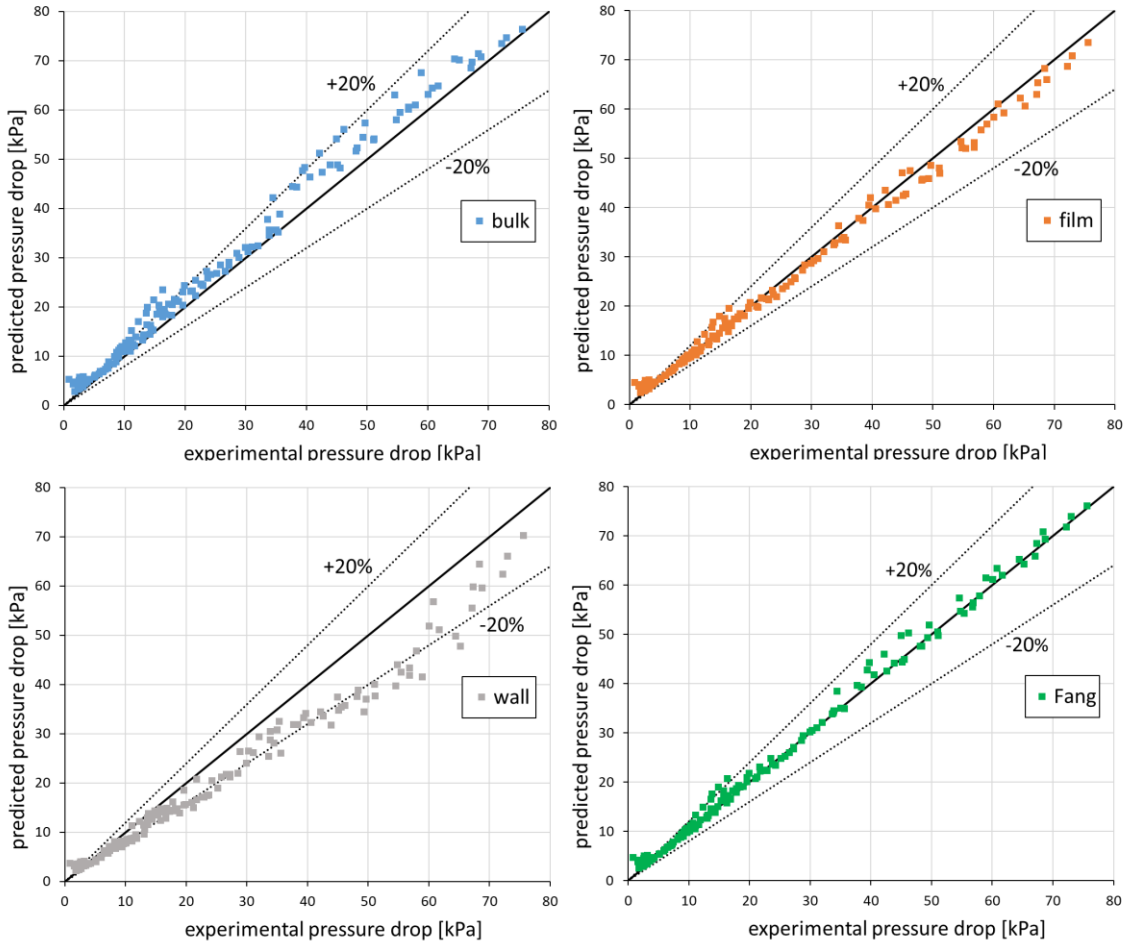

Figure 61: Predicted pressure drop as a function of the experimental pressure drop for the bulk, film and wall properties and the equation by Fang

Table 10: Average deviation and average absolute deviation for the different prediction methods

Prediction [%]	bulk	film	wall	Fang
Average deviation	12,8	-0,6	-16,4	3,9
Average absolute deviation	10,8	3,7	13,9	3,9

For a comparison of the wall properties and the Fang equation, the predicted pressure drop is plotted as a function of the experimental pressure drop in the double logarithmic scale in Figure 62. Additionally, the ± 15% error line is displayed.

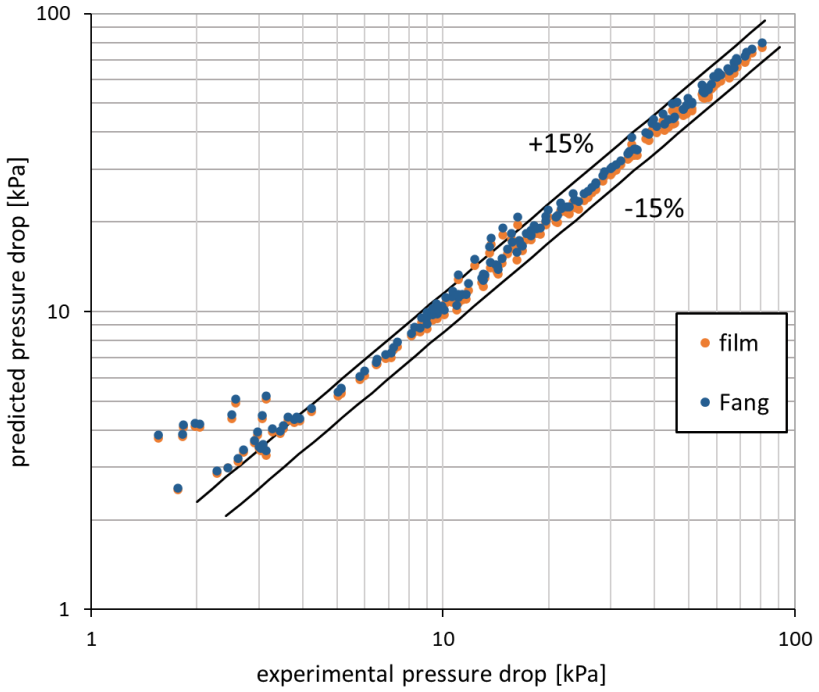

Figure 62: Predicted pressure drop as a function of the experimental pressure drop

6.4.2 3 mm tube

As a starting point, 30 uncooled measurements of the pressure drop were conducted at a constant pressure of 80 bar, three different mass fluxes (640, 850 and 1060 kg/m²s) and a temperature range between 25 and 45°C. In Figure 63, the dimensionless friction factor of the measured parameters is displayed as a function of the Reynolds number. The measured values show a good agreement with the correlation by Konakov [112] (Eq.81) for plain tubes. The average deviation is -2,2% and the average absolute deviation is 4,2%

$$\xi = \frac{1}{(1.8 \lg Re - 1.5)^2} \tag{81}$$

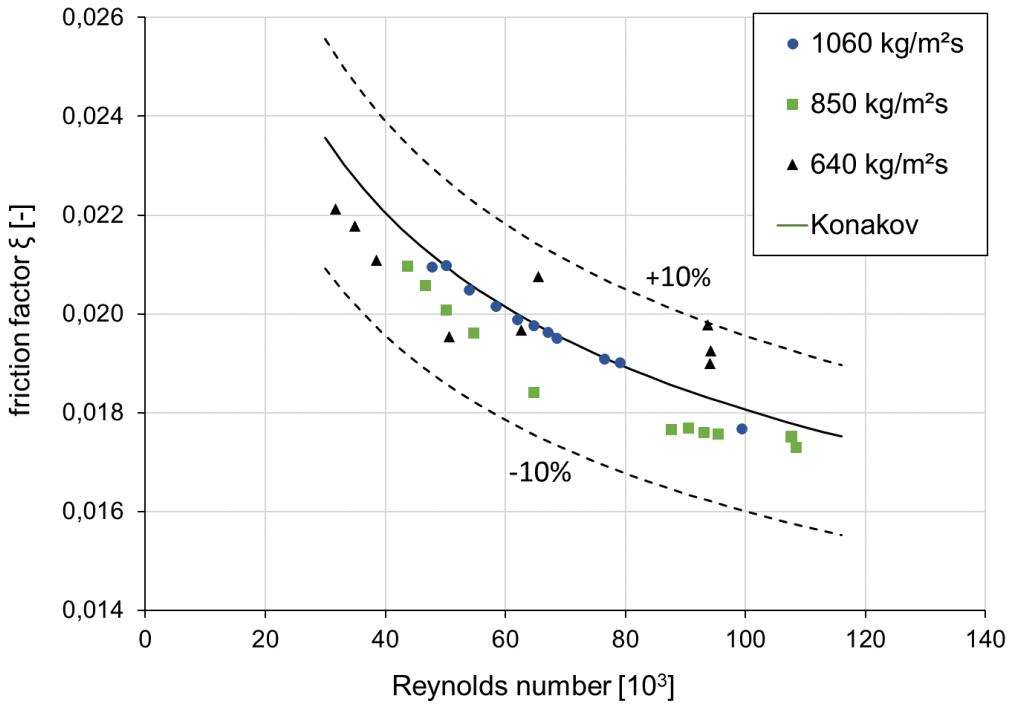

Figure 63: Dimensionless friction factor as a function of Reynolds number of the uncooled pressure drop measurements

The cooling experiments were conducted with a constant pressure of 80 bar and mass flux of 850 kg/m²s. The CO_2 inlet temperature is within the range of 25 to 50 °C. The volumetric cooling flow was constant at 60 ml/s and a cooling temperature between 8 and 34 °C. Each CO_2 inlet temperature was cooled with three different cooling temperatures. In total 45 experiments were conducted. In Figure 64, the frictional pressure drop of the experiments is displayed as a function of the bulk fluid temperature. The pressure drop increases sharply around the pseudocritical temperature of 35°C.

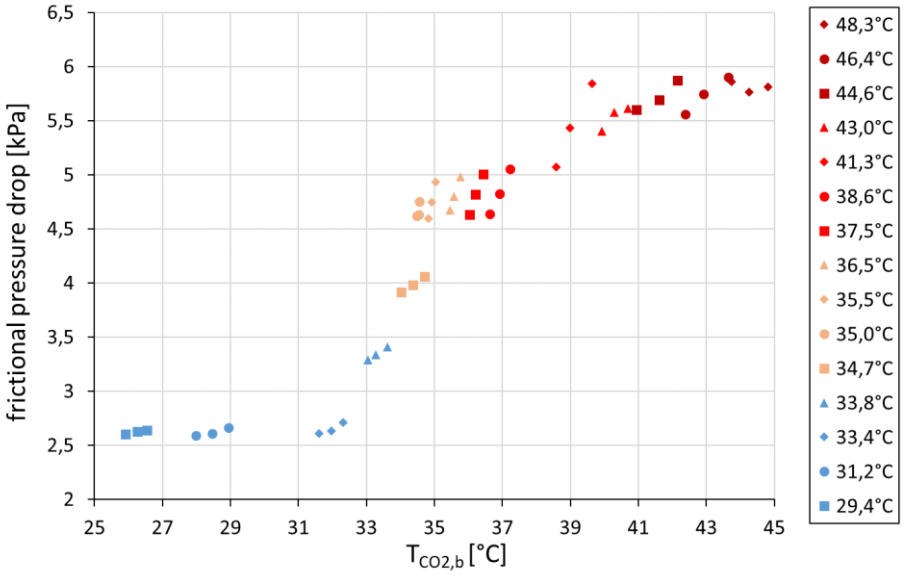

Figure 64: Frictional pressure drop as a function of the bulk fluid temperature at 80bar and 850kg/m²s for 15 sets of inlet temperatures

The prediction of the cooled experiments is based on the Konakov correlation (Eq.82) which was validated in Figure 63.

$$p_{fric} = \frac{1}{2} \frac{1}{(1.8 \lg Re_{\substack{b \\ f \\ w}} - 1.5)^2} * \frac{l}{d} \frac{G^2}{\rho(T_{\substack{b \\ f \\ w}}, p)} \qquad (82)$$

Three different approaches were selected to represent the cooling process. The fluid properties to calculate the Reynolds number and density were based on either the bulk, film or wall properties. The fourth option is the prediction equation by Fang and Xu [115]. The predicted pressure drop is displayed as a function of the experimental pressure drop in Figure 65. The average deviation and average absolute deviation is quantified in Table 11.

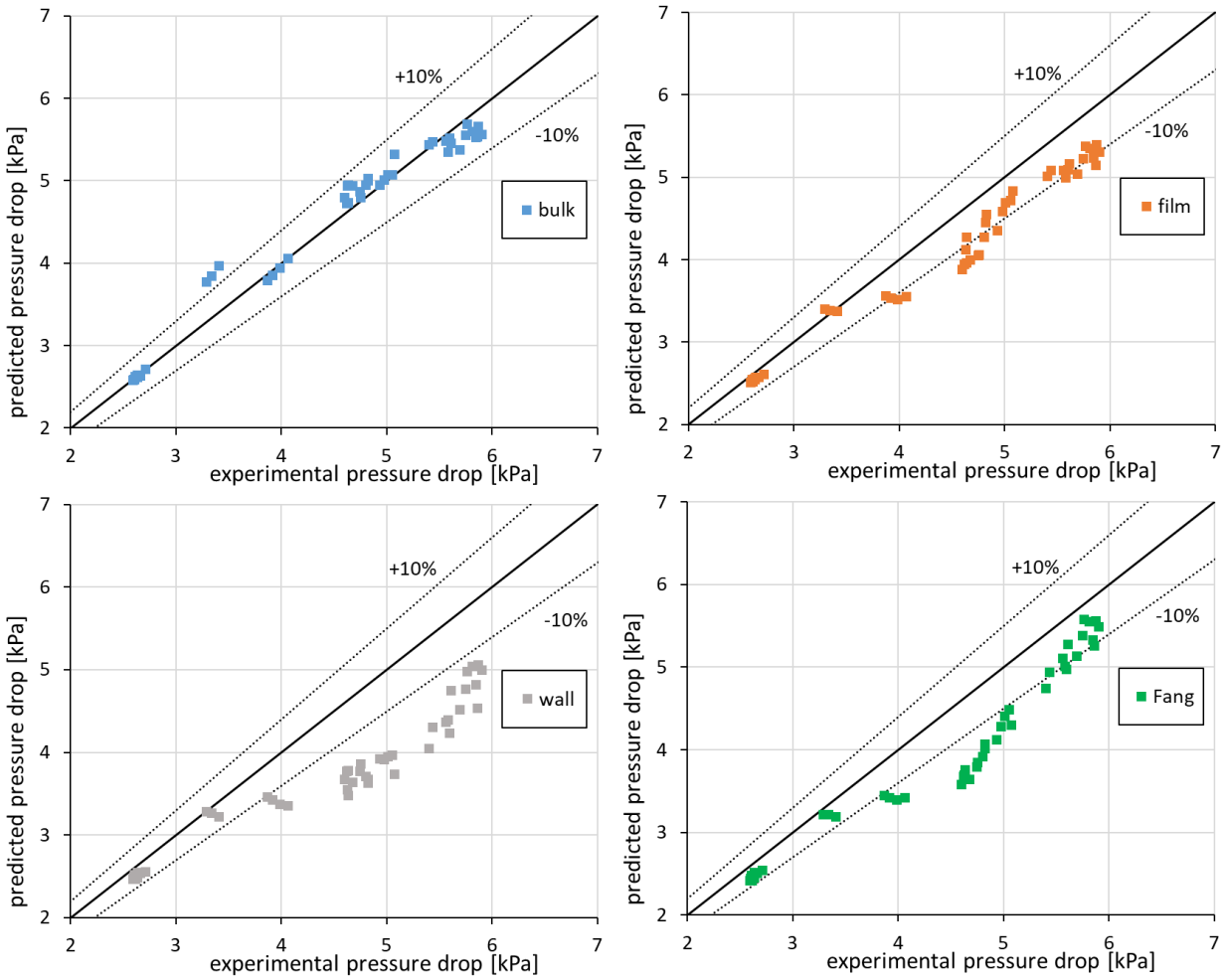

Figure 65: Predicted pressure drop as a function of the experimental pressure drop for bulk, film and wall properties and the equation by Fang

Table 11: Average deviation and average absolute deviation for different prediction methods

Prediction [%]	bulk	film	wall	Fang
Average deviation	1.0	-7.5	-15.0	-10.9
Average absolute deviation	3.2	7.7	15.0	10.9

The bulk properties show the best prediction with an average absolute deviation of 3.2%. The film and wall properties underestimate the pressure drop with an average deviation of -7.7% and -15.0% respectively.

6.4.3 Summary of pressure drop evaluation

The surface of the 2 mm tube can be considered rough which was initially based on measurements of the tube surface. The conducted isothermal measurement campaign showed a lower friction factor with a low average absolute deviation of 3.3% of the regression. Four different approaches were chosen to predict the pressure drop of the cooling case with the regressed roughness used respectively. The prediction by the properties of the film temperature showed the best agreement.

The stainless-steel tube of the 3 mm test section is plain which was shown with the isothermal measurement campaign. A good agreement was reached with the Konakov [112] equation. In the cooling experiments, the prediction based on the bulk fluid properties showed the best prediction.

The results of the two tubes are difficult to compare based on the tube roughness as an additional factor. However, the isothermal measurements were rather simple to evaluate with good agreement to state-of-the-art equations. The cooling experiments were predicted with different methods with a different outcome for the tubes, however, the differences were quite small.

7 Conclusion and Outlook

This work presented the heat transfer and pressure drop performance of supercritical carbon dioxide in small diameter tube flow to contribute to the design of new concepts of compact heat exchangers. Two test sections were built up as tube in tube heat exchangers. CO_2 flows in the inner tube is cooled by the media flowing in the annulus. Temperature measurements in the wall of the inner tube facilitate theevaluation of the heat transfer coefficient of CO_2. The present work is structured in four chapters with respective experimental campaigns. Suitable literature data is presented in each chapter to evaluate the experimental results.The forced convection cooling heat transfer was investigated experimentally in the 2 mm tube. Based on the energy balance of cooling- and CO_2 flow and the repeatability of the single experiments it has been shown that the test section delivers reliable heat transfer performance data. The effects of mass flux, inlet pressure and cooling water temperature on the heat transfer were analyzed with a parametric study. Which means that a single parameter was changed while the other bundarys where kept constant. The heat transfer coefficient increases with increasing mass flux. However, the influence of mass flux on the heat transfer coefficient is significantly stronger near the pseudocritical temperature. The peak value of the heat transfer coefficient appears at a temperature slightly higher than the pseudocritical value. Due to the fluid properties, the peak value of the heat transfer coefficient is shifted and flattened towards higher temperature for increasing pressure. Lower cooling media temperatures causes stronger subcooling of the wall, which leads to a trade-off between heat transfer performance in the early stage of the cooling process and the near pseudo critical region. The effects of the inflow temperature was analized and it showed a defined in- and outflow effect of the test section. It was concluded that a defined data range from the in- and outlet of the test section were excluded from the correlation. Further, the range of validity was defined by the use of dimensionless temperature and heat flux to mass flux ratio. A heat transfer correlation with different parameters of the equation for the liquid-like and the gas-like region was developed with an absolute average deviation of 7.7%. The deviation from literature data was also shown.

In the vertical flow orientation of the 3 mm tube, different mass fluxes where tested in both upwards and downwards flow orientation. The upwards flow showed, as expected, a steady reduction of the heat transfer coefficient as the mass flux decreases. In the downwards flow, at low massfluxes, the decrease of heat transfer coefficient significantly increases. The deterioration of the heat transfer was evaluated based on the wall temperature as function of the bulk temperature. The deterioration of the heat transfer showed significant lower wall temperature than the normal heat transfer. The deterioration was evaluated based on three different heat transfer equations as a function of the Jackson criterium ($\mathrm{Gr}/\mathrm{Re}^{2.7}$). The evaluation showed was splitted in the liquid-like and the gas-like region which showed quite different correlation. The regression of the complete data set showed a mainly good agreement with the most of data with in ± 15% in the normal heat transfer and ± 40% in the deteriorated heat transfer area. The regression was compared with the only available literature correlation. The experimental testing for this deterioration correlation in the cooling case was conducted with a 6 mm innner diameter tube. The dimensionless comparison showed significant differences which might indicate that the tube diameter is a relevant factor of the heat transfer deterioration in cooling heat transfer. It seems like that the phenomena of deterioration and recovery is shifted towards higher $\mathrm{Gr}/\mathrm{Re}^{2.7}$ values.

In the horizontal flow orientation of the 3 mm tube, three different mass fluxes where investigated at constant pressure of 80 bar and heat flux of 12 W/m²K. The results showed significant stratification and the findings where compared to buoyancy parameters from literature. The stratification was detected based on lower wall temperatures in the bottom of the tube compared to the temperatures in the top of the tube. The differences were detected in the liquid-like region with a maximum of 2.5 K at the lowest massflux.Therefore, in the liquid-like region, a threshold value of significant stratification was proposed. In this temperature range, the experimental results show higher values than the proposed literature data. In the gas-like region, no stratification was detected, thus, no comparison is possible. The results indicate that stratification in the cooling case might be influenced by the flow diameter or in general different to that of the heating case.

The pressure drop evaluation for both tubes showed similar results. The isothermal measurements were rather simple to evaluate with good agreement to state-of-the-art equations. However, the results of the two tubes are difficult to compare based on the tube roughness as an additional factor. The 2 mm tube has a rough surfance based on a material analysis. The measured pressure drop in the isothermal experiments were up to 1 bar. The dimensionless evaluation of the friction factor as a function of the Reynoldsnumber showed good agreement with an maximum difference of 8% and thus, delivered the roughness of the tube as it was part of the equation. The cooling experiments were compared with the prediction by the bulk-, film- and wall properties and a literature equation. The lliterature correlation and the prediction with the film properties where similar results the best option. The 3 mm tube was evaluated in the same way as the 2 mm tube. The outcome of the isothermal measuemnst showed good agreement with turbulent friction factor of plain surface tubes. In the cooled experiments, the bulk properties showed the best agreement.

The present work opens up avenues for future work and they can be categorized as follows:

- The forced convection heat transfer can be extended with experimental data of smaller and larger tubes.

- In the vertical flow orientation, the experimental results indicate an influence of the tube diameter. Heat transfer measurements with bigger diameter tubes would close this gap.

- Experimental data on temperature stratification in horizontal flow orientation in the cooling process is very limited in the literature. Experimental and numerical work would both increase the state of the art in this subject.

8 References

1. European Commission, *Communication from the commission to the european parliament, the european council, the council, the european economic and social commitee and the commitee of the regions* (2019).
2. European Commission, "The EU's track record on climate action - The European Green Deal" (2019).
3. M. T. White; G. Bianchi; L. Chai; S. A. Tassou; A. I. Sayma, "Review of supercritical CO 2 technologies and systems for power generation", *Applied Thermal Engineering*, pp. 116447 (2021).
4. Y. Ahn; S. J. Bae; M. Kim; S. K. Cho; S. Baik; J. I. Lee; J. E. Cha, "Review of supercritical CO2 power cycle technology and current status of research and development", *Nuclear Engineering and Technology*, pp. 647–661 (2015).
5. S. B. Riffat; C. F. Afonso; A. C. Oliveira; D. A. Reay, "Natural refrigerants for refrigeration and air-conditioning systems", *Applied Thermal Engineering* 1, pp. 33–42 (1997).
6. C. M. Mendez and G. Rochau, *sCO2 Brayton Cycle: Roadmap to sCO2 Power Cycles NE Commercial Applications -SAND2018-6187*, Albuquerque, New Mexico (2018).
7. T. Kuppan, *Heat exchanger design handbook*, Marcel Dekker, New York (2000).
8. Fundamentals of Heat Exchanger Design, *John Wiley & Sons, Inc*, Hoboken, NJ, USA (2003).
9. S. K. Mylavarapu; X. Sun; R. E. Glosup; R. N. Christensen; M. W. Patterson, "Thermal hydraulic performance testing of printed circuit heat exchangers in a high-temperature helium test facility", *Applied Thermal Engineering* (65 (1–2)), pp. 605–614 (2014).
10. J. P. Abraham; E. M. Sparrow; J. Tong, "Heat transfer in all pipe flow regimes: laminar, transitional/intermittent, and turbulent", *Journal of Heat Transfer* (3-4), pp. 557–563 (2009).
11. M. Chen; X. Sun; R. N. Christensen; S. Shi; I. Skavdahl; V. Utgikar; P. Sabharwall, "Experimental and numerical study of a printed circuit heat exchanger", *Annals of Nuclear Energy* (97), pp. 221–231 (2016).
12. J.-W. Seo; Y.-H. Kim; D. Kim; Y.-D. Choi; K.-J. Lee, "Heat Transfer and Pressure Drop Characteristics in Straight Microchannel of Printed Circuit Heat Exchangers", *Entropy* (5), pp. 3438–3457 (2015).
13. K. Nikitin; Y. Kato; L. Ngo, "Printed circuit heat exchanger thermal–hydraulic performance in supercritical CO2 experimental loop", *International Journal of Refrigeration* (5), pp. 807–814 (2006).
14. T. L. Ngo; Y. Kato; K. Nikitin; N. Tsuzuki, "New printed circuit heat exchanger with S-shaped fins for hot water supplier", *Experimental Thermal and Fluid Science* (8), pp. 811–819 (2006).
15. I. H. Kim and H. C. NO, "Physical model development and optimal design of PCHE for intermediate heat exchangers in HTGRs", *Nuclear Engineering and Design*, pp. 243–250 (2012).

16. S. G. Kim; Y. Lee; Y. Ahn; J. I. Lee, "CFD aided approach to design printed circuit heat exchangers for supercritical CO2 Brayton cycle application", *Annals of Nuclear Energy*, pp. 175–185 (2016).
17. M. Chen; X. Sun; R. N. Christensen; I. Skavdahl; V. Utgikar; P. Sabharwall, "Pressure drop and heat transfer characteristics of a high-temperature printed circuit heat exchanger", *Applied Thermal Engineering*, pp. 1409–1417 (2016).
18. S.-J. Yoon; J. O'Brien; M. Chen; P. Sabharwall; X. Sun, "Development and validation of Nusselt number and friction factor correlations for laminar flow in semi-circular zigzag channel of printed circuit heat exchanger", *Applied Thermal Engineering*, pp. 1327–1344 (2017).
19. N. Tsuzuki; M. Utamura; T. L. Ngo, "Nusselt number correlations for a microchannel heat exchanger hot water supplier with S-shaped fins", *Applied Thermal Engineering* (16), pp. 3299–3308 (2009).
20. W. Chu; X. Li; T. Ma; Y. Chen; Q. Wang, "Study on hydraulic and thermal performance of printed circuit heat transfer surface with distributed airfoil fins", *Applied Thermal Engineering*, pp. 1309–1318 (2017).
21. J. G. Kwon; T. H. Kim; H. S. Park; J. E. Cha; M. H. Kim, "Optimization of airfoil-type PCHE for the recuperator of small scale brayton cycle by cost-based objective function", *Nuclear Engineering and Design*, pp. 192–200 (2016).
22. J. Y. Ho; K. K. Wong; K. C. Leong; T. N. Wong, "Convective heat transfer performance of airfoil heat sinks fabricated by selective laser melting", *International Journal of Thermal Sciences*, pp. 213–228 (2017).
23. Z. Zhao; K. Zhao; D. Jia; P. Jiang; R. Shen, "Numerical Investigation on the Flow and Heat Transfer Characteristics of Supercritical Liquefied Natural Gas in an Airfoil Fin Printed Circuit Heat Exchanger", *Energies* (11), pp. 1828 (2017).
24. W. Chu; K. Bennett; J. Cheng; Y. Chen; Q. Wang, "Thermo-Hydraulic Performance of Printed Circuit Heat Exchanger With Different Cambered Airfoil Fins", *Heat Transfer Engineering*, pp. 1–15 (2019).
25. Y. T. Ge; S. A. Tassou; I. D. Santosa; K. Tsamos, "Design optimisation of CO2 gas cooler/condenser in a refrigeration system", *Applied Energy*, pp. 973–981 (2015).
26. J. Li; J. Jia; L. Huang; S. Wang, "Experimental and numerical study of an integrated fin and micro-channel gas cooler for a CO 2 automotive air-conditioning", *Applied Thermal Engineering*, pp. 636–647 (2017).
27. "An experimental comparison between a microchannel cooler and conventional coolers of a CO2 air conditioning cycle".
28. J. M. Yin; C. W. Bullard; P. S. Hrnjak, "R-744 gas cooler model development and validation", *International Journal of Refrigeration* (7), pp. 692–701 (2001).
29. A. Vojacek; V. Dostal; F. Goettelt; M. Rohde; T. Melichar, "Performance Test of the Air-Cooled Finned-Tube Supercritical CO2 Sink Heat Exchanger", *Journal of Thermal Science and Engineering Applications* (3), pp. 1-11 (2019).

30. R. M. Manglik and A. E. Bergles, "Heat transfer and pressure drop correlations for the rectangular offset strip fin compact heat exchanger", *Experimental Thermal and Fluid Science* (2), pp. 171–180 (1995).
31. M. M. Ganzarolli and C. A. C. Altemani, "Optimum Fins Spacing and Thickness of a Finned Heat Exchanger Plate", *Heat Transfer Engineering* 1, pp. 25–32 (2010).
32. W. Li and X. Wang, "Heat transfer and pressure drop correlations for compact heat exchangers with multi-region louver fins", *International Journal of Heat and Mass Transfer* (15-16), pp. 2955–2962 (2010).
33. H. Najafi; B. Najafi; P. Hoseinpoori, "Energy and cost optimization of a plate and fin heat exchanger using genetic algorithm", *Applied Thermal Engineering* (10), pp. 1839–1847 (2011).
34. J. Fernández-Seara; R. Diz; F. J. Uhía, "Pressure drop and heat transfer characteristics of a titanium brazed plate-fin heat exchanger with offset strip fins", *Applied Thermal Engineering* (1-2), pp. 502–511 (2013).
35. D. Taler, "Experimental determination of correlations for average heat transfer coefficients in heat exchangers on both fluid sides", *Heat and Mass Transfer* (8), pp. 1125–1139 (2013).
36. M. Khoshvaght-Aliabadi; M. Khoshvaght; P. Rahnama, "Thermal-hydraulic characteristics of plate-fin heat exchangers with corrugated/vortex-generator plate-fin (CVGPF)", *Applied Thermal Engineering*, pp. 690–701 (2016).
37. H. Peng; X. Ling; J. Li, "Performance investigation of an innovative offset strip fin arrays in compact heat exchangers", *Energy Conversion and Management*, pp. 287–297 (2014).
38. T. Chen; J. Wang; W. Peng, "Flow and heat transfer analyses of a plate-fin heat exchanger in an HTGR", *Annals of Nuclear Energy*, pp. 316–328 (2017).
39. B. B. Kuchadiya and P. P. Rathod, "Investigation of Hydraulic Behavior of PFHE Used for Cooling Application", *Energy Procedia*, pp. 40–47 (2017).
40. V. Dostal, *A Supercritical Carbon Dioxide Cycle for Next Generation Nuclear Reactors* (2004).
41. F. Nasuti and M. Pizzarelli, "Pseudo-boiling and heat transfer deterioration while heating supercritical liquid rocket engine propellants", *The Journal of Supercritical Fluids*, pp. 105066 (2021).
42. EXPERIMENTAL INVESTIGATIONS ON THE HEAT TRANSFER CHARACTERISTICS OF SUPERCRITICAL CO2 IN HEATED HORIZONTAL PIPES (2021).
43. D. M. McEligot and J. D. Jackson, ""Deterioration" criteria for convective heat transfer in gas flow through non-circular ducts", *Nuclear Engineering and Design* (3), pp. 327–333 (2004).
44. J. H. Song; H. Y. Kim; H. Kim; Y. Y. Bae, "Heat transfer characteristics of a supercritical fluid flow in a vertical pipe", *The Journal of Supercritical Fluids* (2), pp. 164–171 (2008).
45. D. E. Kim and M.-H. Kim, "Experimental investigation of heat transfer in vertical upward and downward supercritical CO2 flow in a circular tube", *International Journal of Heat and Fluid Flow* 1, pp. 176–191 (2011).
46. Y.-Y. Bae and H.-Y. Kim, "Convective heat transfer to CO2 at a supercritical pressure flowing vertically upward in tubes and an annular channel", *Experimental Thermal and Fluid Science* (2), pp. 329–339 (2009).

47. X. R. Zhang and H. Yamaguchi, "Forced convection heat transfer of supercritical CO2 in a horizontal circular tube", *The Journal of Supercritical Fluids* (3), pp. 412–420 (2007).
48. X. L. Cao; Z. H. Rao; S. M. Liao, "Laminar convective heat transfer of supercritical CO_2 in horizontal miniature circular and triangular tubes", *Applied Thermal Engineering* (14-15), pp. 2374–2384 (2011).
49. Z. Du; W. Lin; A. Gu, "Numerical investigation of cooling heat transfer to supercritical CO2 in a horizontal circular tube", *The Journal of Supercritical Fluids* 1, pp. 116–121 (2010).
50. S. Pandey and E. Laurien, "Heat transfer analysis at supercritical pressure using two layer theory", *The Journal of Supercritical Fluids*, pp. 80–86 (2016).
51. S. S. Pitla; E. A. Groll; S. Ramadhyani, "New correlation to predict the heat transfer coefficient during in-tube cooling of turbulent supercritical CO2", *International Journal of Refrigeration* (7), pp. 887–895 (2002).
52. S. H. Yoon; J. H. Kim; Y. W. Hwang; M. S. Kim; K. Min; Y. Kim, "Heat transfer and pressure drop characteristics during the in-tube cooling process of carbon dioxide in the supercritical region", *International Journal of Refrigeration* (8), pp. 857–864 (2003).
53. H.-K. Oh and C.-H. Son, "New correlation to predict the heat transfer coefficient in-tube cooling of supercritical CO2 in horizontal macro-tubes", *Experimental Thermal and Fluid Science* (8), pp. 1230–1241 (2010).
54. Z.-B. Liu; Y.-L. He; Z.-G. Qu; W.-Q. Tao, "Experimental study of heat transfer and pressure drop of supercritical CO2 cooled in metal foam tubes", *International Journal of Heat and Mass Transfer*, pp. 679–693 (2015).
55. C. Kondou and P. Hrnjak, "Heat rejection from R744 flow under uniform temperature cooling in a horizontal smooth tube around the critical point", *International Journal of Refrigeration* (3), pp. 719–731 (2011).
56. S. Pandey; X. Chu; E. Laurien, "Investigation of in-tube cooling of carbon dioxide at supercritical pressure by means of direct numerical simulation", *International Journal of Heat and Mass Transfer*, pp. 944–957 (2017).
57. M. Xiang; J. Guo; X. Huai; X. Cui, "Thermal analysis of supercritical pressure CO_2 in horizontal tubes under cooling condition", *The Journal of Supercritical Fluids* (130), pp. 389–398 (2017).
58. C. Dang and E. Hihara, "In-tube cooling heat transfer of supercritical carbon dioxide. Part 1. Experimental measurement", *International Journal of Refrigeration* (7), pp. 736–747 (2004).
59. S. M. Liao and T. S. Zhao, "An experimental investigation of convection heat transfer to supercritical carbon dioxide in miniature tubes", *International Journal of Heat and Mass Transfer* (25), pp. 5025–5034 (2002).
60. K. Brun; P. Friedman; R. Dennis, *Fundamentals and applications of supercritical carbon dioxide (sCO2) based power cycles*, Elsevier, Woodhead Publishing (2017).
61. V. Badescu; G. C. Lazaroiu; L. Barelli, *Power Engineering*, Chapman and Hall/CRC, Milton (2018).
62. P. J. Maziasz and R. W. Swindeman, "Selecting and Developing Advanced Alloys for Creep-Resistance for Microturbine Recuperator Applications1", *Journal of Engineering for Gas Turbines and Power* 1, pp. 310–315 (2003).

63. H. Osman; A. Borhana; M. N. Tamin, "Material Parameters for Creep Rupture of Austenitic Stainless Steel Foils", *Journal of Materials Engineering and Performance* (8), pp. 2858–2863 (2014).
64. N. D. Evans; P. J. Maziasz; J. P. Shingledecker; Y. Yamamoto, "Microstructure evolution of alloy 625 foil and sheet during creep at 750°C", *Materials Science and Engineering: A* (1-2), pp. 412–420 (2008).
65. J. Klöwer; R. U. Husemann; M. Bader, "Development of Nickel Alloys Based on Alloy 617 for Components in 700°C Power Plants", *Procedia Engineering*, pp. 226–231 (2013).
66. M. Anderson; G. Nellis; M. Corradini, *Materials, Turbomachinery and Heat Exchangers for Supercritical CO2 Systems*.
67. L. Chai and S. A. Tassou, "A review of printed circuit heat exchangers for helium and supercritical CO2 Brayton cycles", *Thermal Science and Engineering Progress* (18), pp. 100543 (2020).
68. OE Balje, *Turbomachines: A guide to design, selection, and theory(Book)* (1981).
69. *Advanced regulatory control of a 10 mwe supercritical CO2 recompression brayton cycle towards improving power ramp rates* (2018).
70. E. Hakkarainen; T. Sihvonen; J. Lappalainen, "Dynamic modelling and simulation of CSP plant based on supercritical carbon dioxide closed Brayton cycle", pp. 70004.
71. M. T. Luu; D. Milani; R. McNaughton; A. Abbas, "Analysis for flexible operation of supercritical CO2 Brayton cycle integrated with solar thermal systems", *Energy*, pp. 752–771 (2017).
72. M. T. Luu; D. Milani; R. McNaughton; A. Abbas, "Dynamic modelling and start-up operation of a solar-assisted recompression supercritical CO 2 Brayton power cycle", *Applied Energy*, pp. 247–263 (2017).
73. A. Moisseytsev and J. J. Sienicki, "Modeling of the SNL S-CO2 Loop With ANL Plant Dynamics Code", pp. 641–650.
74. A. Moisseytsev and J. J. Sienicki, *Simulation of IST Turbomachinery Power-Neutral Tests with the ANL Plant Dynamics Code* (2016).
75. R. Singh; S. A. Miller; A. S. Rowlands; P. A. Jacobs, "Dynamic characteristics of a direct-heated supercritical carbon-dioxide Brayton cycle in a solar thermal power plant", *Energy*, pp. 194–204 (2013).
76. E. M. Clementoni; T. L. Cox; M. A. King, "Off-Nominal Component Performance in a Supercritical Carbon Dioxide Brayton Cycle", *Journal of Engineering for Gas Turbines and Power* 1 (2016).
77. M. Marchionni; L. Chai; G. Bianchi; S. A. Tassou, "Numerical modelling and transient analysis of a printed circuit heat exchanger used as recuperator for supercritical CO2 heat to power conversion systems", *Applied Thermal Engineering*, pp. 114190 (2019).
78. T. Q. Trinh, *Dynamic response of the supercritical $C0_2$ Brayton recompression cycle to various system transients*.
79. J. S. Kwon; S. Son; J. Y. Heo; J. I. Lee, "Compact heat exchangers for supercritical CO2 power cycle application", *Energy Conversion and Management*, pp. 112666 (2020).
80. Heat and Mass Transfer Intensification and Shape Optimization, *Springer*, London (2013).

81. [Der Titel "Fan, Luo et al. 2013 – Design of Compact Heat Exchangers" kann nicht dargestellt werden. Die Vorlage "Literaturverzeichnis - Beitrag im Sammelwerk - (Standardvorlage)" enthält keine Informationen.]
82. Q. Li; G. Flamant; X. Yuan; P. Neveu; L. Luo, "Compact heat exchangers: A review and future applications for a new generation of high temperature solar receivers", *Renewable and Sustainable Energy Reviews* (9), pp. 4855–4875 (2011).
83. H.-J. Bart and S. Scholl, *Innovative Heat Exchangers*, Springer International Publishing, Cham (2018).
84. A. A. Bhuiyan and A. S. Islam, "Thermal and hydraulic performance of finned-tube heat exchangers under different flow ranges: A review on modeling and experiment", *Journal of Heat Transfer*, pp. 38–59 (2016).
85. Compact heat exchangers, *Pergamon*, Amsterdam, New York (2001).
86. E. W. Lemmon; M. L. Huber; M. O. McLinden, *REFPROP*, NIST Standard Reference Database 23, United States of America (2010).
87. R. Span and W. Wagner, "A New Equation of State for Carbon Dioxide Covering the Fluid Region from the Triple-Point Temperature to 1100 K at Pressures up to 800 MPa", *Journal of Physical and Chemical Reference Data* (6), pp. 1509–1596 (1996).
88. V. Vesovic; W. A. Wakeham; G. A. Olchowy; J. V. Sengers; J. T. R. Watson; J. Millat, "The Transport Properties of Carbon Dioxide", *Journal of Physical and Chemical Reference Data* (3), pp. 763–808 (1990).
89. Fenghour, A., Wakeham, W.A., Vesovic, V., "The Viscosity of Carbon Dioxide", *Journal of Physical and Chemical Reference Data* 1 (1998).
90. V. Gnielinski, "New equation for heat and mass transfer in turbulent pipe and channel flow", *International Chemical Engineering* (2), pp. 359–368 (1976).
91. F. W. Dittus and L. Boelter, "Heat transfer in automobile radiators of the tubular type", *International Communications in Heat and Mass Transfer* 1, pp. 3–22 (1985).
92. An Assessment of the criteria for the onset of heat transfer deterioration with supercritical CO_2 in vertical heated single circular tubes, *DuEPublico: Duisburg-Essen Publications online, University of Duisburg-Essen, Germany* (September 19-20, 2019).
93. M. F. Löwenberg, *Wärmeübergang von Wasser in vertikalen Rohrströmungen bei überkritischem Druck*, Stuttgart (2007).
94. V. A. Kurganov and A. G. Kaptilnyi, "Flow structure and turbulent transport of a supercritical pressure fluid in a vertical heated tube under the conditions of mixed convection. Experimental data", *International Journal of Heat and Mass Transfer*, *Elsevier*, pp. 3383–3392 (September, 1993).
95. Petukhov B.S., Kurganov B.A., Ankudinov B.B., "Heat transfer and flow resistance in the turbulent pipe flow of a fluid with near-critical state parameters", *Teplofizika Vysokikh Temperatur* (21), pp. 92–100 (1983).
96. J. D. Jackson, "Fluid flow and convective heat transfer to fluids at supercritical pressure", *Nuclear Engineering and Design*, pp. 24–40 (2013).

97. J. H. Bae; J. Y. Yoo; H. Choi, "Direct numerical simulation of turbulent supercritical flows with heat transfer", *Journal of Heat Transfer* (10), pp. 105104 (2005).
98. Experimental Investigation on the Heat Transfer Characteristics in a Vertical Upward Flow of Supercritical CO2 (June 4-8, 2006).
99. K. Yamagata; K. Nishikawa; S. Hasegawa; T. Fujii; S. Yoshida, "Forced convective heat transfer to supercritical water flowing in tubes", *International Journal of Heat and Mass Transfer* (12), pp. 2575–2593 (1972).
100. I. L. Pioro; H. F. Khartabil; R. B. Duffey, "Heat transfer to supercritical fluids flowing in channels—empirical correlations (survey)", *Nuclear Engineering and Design* (1-3), pp. 69–91 (2004).
101. Heat Transfer at Supercritical Pressures and the Onset of Deterioration, *ASME* (2006).
102. S. M. Liao and T. S. Zhao, "Measurements of Heat Transfer Coefficients From Supercritical Carbon Dioxide Flowing in Horizontal Mini/Micro Channels", *Journal of Heat Transfer* (3), pp. 413 (2002).
103. X. Lei; Q. Zhang; J. Zhang; H. Li, "Experimental and Numerical Investigation of Convective Heat Transfer of Supercritical Carbon Dioxide at Low Mass Fluxes", *Applied Sciences* (12), pp. 1260 (2017).
104. P.-X. Jiang; C.-R. Zhao; R.-F. Shi; Y. Chen; W. Ambrosini, "Experimental and numerical study of convection heat transfer of CO2 at super-critical pressures during cooling in small vertical tube", *International Journal of Heat and Mass Transfer* (21-22), pp. 4748–4756 (2009).
105. A. Bruch; A. Bontemps; S. Colasson, "Experimental investigation of heat transfer of supercritical carbon dioxide flowing in a cooled vertical tube", *International Journal of Heat and Mass Transfer* (11-12), pp. 2589–2598 (2009).
106. J. D. Jackson and W. B. Hall, "Forced Convection Heat Transfer to Fluids at Supercritical Pressure", *Institution of Mechanical Engineers, Conference Publications* (1979).
107. G. A. Adebiyi and W. B. Hall, "Experimental investigation of heat transfer to supercritical pressure carbon dioxide in a horizontal pipe", *Journal of Heat Transfer* (7), pp. 715–720 (1976).
108. W. Lin; Z. Du; A. Gu, "Analysis on heat transfer correlations of supercritical CO2 cooled in horizontal circular tubes", *Heat and Mass Transfer* (4), pp. 705–711 (2012).
109. L. Diao; Y. Chen; Y. Li, "Nonuniform heat transfer of supercritical pressure carbon dioxide under turbulent cooling condition in circular tubes at various inclination angles", *Nuclear Engineering and Design*, pp. 110153 (2019).
110. K. Tanimizu and R. Sadr, "Experimental investigation of buoyancy effects on convection heat transfer of supercritical CO2 flow in a horizontal tube", *Heat and Mass Transfer*, *Springer; Springer Berlin Heidelberg* (4), pp. 713–726 (2016).
111. T. H. Kim; J. G. Kwon; M. H. Kim; H. S. Park, "Experimental investigation on validity of buoyancy parameters to heat transfer of CO2 at supercritical pressures in a horizontal tube", *Experimental Thermal and Fluid Science* (92), pp. 222–230 (2018).
112. VDI-Wärmeatlas. Verein Deutscher Ingenieure, VDI-Gesellschaft Verfahrenstechnik und Chemieingenieurwesen (GVC), *Springer Berlin Heidelberg*, Berlin, Heidelberg, s.l. (2002).

113. P. V. Petrov N, "Heat-transfer and resistance of carbon-dioxide being cooled in the supercritical region", *Therm Eng 1985*.
114. C.-H. Son and S.-J. Park, "An experimental study on heat transfer and pressure drop characteristics of carbon dioxide during gas cooling process in a horizontal tube", *International Journal of Refrigeration* (4), pp. 539–546 (2006).
115. X. Fang and Y. Xu, "Modified heat transfer equation for in-tube supercritical CO2 cooling", *Applied Thermal Engineering* (14-15), pp. 3036–3042 (2011).
116. J. Pettersen; R. Rieberer; S. Tollak Munkejord, "Heat Transfer and pressure drop characteristics of evaporating carbon dioxide in mikrochannel tubes", *Purdue University*, pp. 1–10 (2000).
117. X. L. Huai; S. Koyama; T. S. Zhao, "An experimental study of flow and heat transfer of supercritical carbon dioxide in multi-port mini channels under cooling conditions", *Chemical Engineering Science* (12), pp. 3337–3345 (2005).
118. J. Lv; M. Fu; N. Qin; B. Dong, "Experimental study on heat transfer characteristics of supercritical carbon dioxide in horizontal tube", *Frontiers of Energy and Power Engineering in China* (3), pp. 339–343 (2008).
119. Z.-B. Liu; Y.-L. He; Y.-F. Yang; J.-Y. Fei, "Experimental study on heat transfer and pressure drop of supercritical CO2 cooled in a large tube", *Applied Thermal Engineering* 1, pp. 307–315 (2014).
120. W. Flaig, *Thermohydraulische Untersuchung eines diffusionsgeschweißten Kompaktwärmeübertragers zur Ertüchtigung eines Wärmeabfuhrsystems mit Kohlenstoffdioxid als Arbeitsmittel*, Universität Stuttgart, Stuttgart, Germany (2019).
121. A. Wahl; R. Mertz; E. Laurien; J. Starflinger, "Heat transfer correlation for sCO2 cooling in a 2 mm tube", *The Journal of Supercritical Fluids* (173), pp. 105221 (2021).